

**UNIVERSIDADE TECNOLÓGICA FEDERAL DO PARANÁ**

**JESSÉ DE PELEGRIN**

**DESENVOLVIMENTO E APLICAÇÕES DE SENSORES A FIBRA ÓTICA PARA  
INSTRUMENTAÇÃO DE MÁQUINAS ELÉTRICAS**

**CURITIBA**

**2022**

**JESSÉ DE PELEGRIN**

**DESENVOLVIMENTO E APLICAÇÕES DE SENSORES A FIBRA ÓTICA PARA  
INSTRUMENTAÇÃO DE MÁQUINAS ELÉTRICAS**

**Development And Applications Of Optical Fiber Sensors For Electric  
Machines Instrumentation**

Tese apresentada como requisito para obtenção do título de Doutor em Ciências, do Programa de Pós-Graduação em Engenharia Elétrica e Informática Industrial da Universidade Tecnológica Federal do Paraná (UTFPR).

Orientador: Prof. Dr. Jean Carlos Cardozo da Silva

Coorientador: Dr. João Paulo Bazzo

**CURITIBA**

**2022**



[4.0 Internacional](https://creativecommons.org/licenses/by/4.0/)

Esta licença permite compartilhamento, remixe, adaptação e criação a partir do trabalho, mesmo para fins comerciais, desde que sejam atribuídos créditos ao(s) autor(es). Conteúdos elaborados por terceiros, citados e referenciados nesta obra não são cobertos pela licença.



**Ministério da Educação  
Universidade Tecnológica Federal do Paraná  
Campus Curitiba**



JESSE DE PELEGRIN

**DESENVOLVIMENTO E APLICAÇÕES DE SENSORES A FIBRA ÓTICA PARA INSTRUMENTAÇÃO DE MÁQUINAS ELÉTRICAS**

Trabalho de pesquisa de doutorado apresentado como requisito para obtenção do título de Doutor Em Ciências da Universidade Tecnológica Federal do Paraná (UTFPR). Área de concentração: Fotônica Em Engenharia.

Data de aprovação: 13 de Maio de 2022

Dr. Jean Carlos Cardozo Da Silva, Doutorado - Universidade Tecnológica Federal do Paraná

Dr. Carlos Ruiz Zamarreno, Doutorado - Univeridad Pública de Navarra

Dr. Joao Paulo Bazzo, Doutorado - Universidade Tecnológica Federal do Paraná

Dr. Marco Jose Da Silva, Doutorado - Universidade Tecnológica Federal do Paraná

Dr. Uilian Jose Dreyer, Doutorado - Universidade Tecnológica Federal do Paraná

Dr. Yales Romulo De Novaes, Doutorado - Fundação Universidade do Estado de Santa Catarina (Udesc)

Documento gerado pelo Sistema Acadêmico da UTFPR a partir dos dados da Ata de Defesa em 16/05/2022.

To my parents, Vilmar and Evanilde, my brother,  
Juliano, my wife Christiane and daughter Alice.

## **AGRADECIMENTOS**

I thank my wife and daughter, Christiane Barbieri from Pelegrin, and Alice Barbieri from Pelegrin, for their motivation and understanding during my absence. My parents and brother Vilmar de Pelegrin, Evanilde Leonir de Pelegrin, and Juliano de Pelegrin are my references and inspirations always to move forward.

I would like to thank, in particular, my supervisor Jean Carlos Cardozo da Silva, for accepting to guide me. For the shared teachings that were fundamental to achieving the results presented. To the co-supervisor, João Paulo Bazzo, for his help, interest, and ideas contributing to this work's conclusion.

To professors Uilian Jose Dreyer and Kleiton Morais de Sousa, colleagues since graduation, and master's and doctoral professors who helped me conclude the course. And in their names all the CPGEI program teachers who transmitted their teachings. To the colleagues and friends of the department who helped me directly and indirectly in carrying out this work.

To professors Carlos Ruiz Zamarreño, Ignacio Matías, and colleague and doctoral friend Ignacio Vitoria for their reception and education during the internship at UPNA.

The author acknowledge CAPES (Coordination of Superior Level Staff Improvement), CNPQ (National Council for Scientific and Technological Development), FINEP (Funding Authority for Studies and Projects), Araucária Foundation, and SETI (State Secretary of Science, Technology, and Higher Education of Paraná), and Multi-User Photonics Facility - UTFPR-CT, IFC (Federal Institute of Catarinense), Universidad Pública de Navarra. This study was financed in part by the Coordenação de Aperfeiçoamento de Pessoal de Nível Superior - Brasil (CAPES) - Finance Code 001.

## RESUMO

Esta tese apresenta novos métodos para monitorar temperatura e deformação dinâmica em máquinas elétricas rotativas usando dois sensores de fibra óptica: 1) com redes de Bragg (FBG) encapsulado em polímero reforçado com fibra de carbono (CFRP) e 2) com sensores de temperatura distribuídos (DTS). Em máquinas elétricas, altas temperaturas e vibrações, se não detectadas precocemente, podem desgastar o isolamento elétrico, aumentando o risco de falhas de curto-circuito nas bobinas do estator. Esta tese é uma coleção de quatro artigos publicados: os dois primeiros são com sensores baseados em FBG, e os dois últimos com sensores baseados em DTS. Devido os sensores serem mecanicamente frágeis a tensões de cisalhamento, os encapsulamentos de CFRP conferem-lhes robustez sem alterar significativamente sua sensibilidade. O primeiro sensor FBG foi construído em forma do núcleo do estator de um motor de indução trifásico (MIT), e este projeto foi patenteado. A dinâmica do motor operando com rolamentos novos e danificados, em vazio e com carga, foram avaliados em ambiente industrial. O segundo sensor FBG foi projetado para operar em contato com o rolamento. Além de permitir rápida instalação, a detecção dos defeitos concentram-se no mensurando. Na análise de defeitos de rolamento, os resultados dos testes foram consistentes com os resultados teóricos para ambos os sensores FBG. No terceiro artigo o objetivo foi monitorar a temperatura usando um sensor DTS na região final da barra do estator de um gerador de 355 MW que superaquece e tem dimensões inferiores a 50 cm. No entanto, o equipamento de aquisição do sensor DTS não detecta com precisão os sinais com resolução espacial abaixo de 1 m. Para superar este problema, um algoritmo de reconstrução de sinal baseado em deconvolução de sinal por *total variation* foi usado, permitindo medições em comprimentos de até 15 cm. O quarto artigo focou na mapeamento de um MIT de 20 cv operando na indústria papeleira. A instrumentação DTS é realizada em todas as ranhuras do núcleos do estator com fibra óptica revestida com Teflon<sup>®</sup> 900  $\mu\text{m}$ , para identificar regiões quentes. Os resultados alcançados nos trabalhos demonstraram o potencial dos métodos propostos para o monitoramento contínuo de temperatura e deformação dinâmica em máquinas elétricas.

**Palavras-chave:** deformação dinâmica e sensoriamento de temperatura; máquinas elétricas rotativas; redes de bragg em fibra óptica; sensoriamento distribuído de temperatura; sensores óticos integrados em fibra de carbono.

## ABSTRACT

This thesis presents new methods for monitoring temperature and dynamic deformation in rotating electrical machines using two optical fiber sensors: 1) a smart fiber Bragg grating (FBG) sensor encapsulated in carbon fiber reinforced polymer (CFRP) and 2) a sensor based on distributed temperature sensing (DTS). In electrical machines, high temperatures and excessive vibrations, if not detected early, can wear out the electrical insulation, increasing the risk of short-circuit failures in stator coils. This thesis is a collection of four published papers: the first two deal with sensors based on FBG, and the last two with sensors based on DTS. Because sensors are mechanically fragile to shear stresses, CFRP encapsulations provide them robustness without significantly altering their sensitivity. The first FBG sensor was built in the shape of the stator core of a three-phase induction motor (TIM), and this design was patented. The dynamics of the motor operating with new and damaged bearings at no load and rated load were evaluated in an industrial environment. The second FBG sensor was designed to operate in contact with the bearing. In addition to allowing quick installation, the detection of defects focuses on the measuring. In the analysis of bearing defects, the test results were consistent with the theoretical results for both the FBG sensors. The third article aimed to monitor the temperature using a DTS sensor in the end-winding region of the stator bar of a 355 MW generator that overheats and has dimensions smaller than 50 cm. However, the optical interrogator of the DTS sensor does not accurately detect signals with spatial resolution below 1 m. To overcome this problem, a signal reconstruction algorithm based on signal deconvolution by total variation was used to improve the spatial resolution up to 15 cm. The fourth article focused on the thermal mapping of a 20 hp TIM operating in the paper-manufacturing industry. The DTS instrumentation is performed in all stator core slots with optical fiber coated with Teflon<sup>®</sup> 900  $\mu\text{m}$ , to identify hot regions. The results achieved in the works demonstrated the potential of the proposed methods for the continuous monitoring of temperature and dynamic deformation in electrical machines.

**Keywords:** distributed temperature sensing; dynamic strain and temperature sensing; fiber bragg gratings; optical sensors integrated in carbon fiber; rotative electrical machine.

## Thesis Contributions - Papers and patents

- Journal Papers

J. de Pelegrin, U. J. Dreyer, C. Martelli and J. C. C. da Silva, "Optical Fiber Sensor Encapsulated in Carbon Fiber Reinforced Polymer for Fault Detection in Rotating Electrical Machines," in **IEEE Sensors Journal**, vol. 20, no. 19, pp. 11364-11371, 1 Oct.1, 2020, doi: 10.1109/JSEN.2020.2997597.

Pelegrin, J.d., Bazzo, J.P., Dreyer, U.J., Martelli, C., Pipa, D.R., Silva, E.V.d. and Cardozo da Silva, J.C. (2020), "Raman distributed temperature sensing for end winding of high-power generator". **IET Optoelectron.**, 14: 343-349. <https://doi.org/10.1049/iet-opt.2020.0037>.

J. de Pelegrin, U. J. Dreyer, J. P. Bazzo and J. C. C. d. Silva, "Faults Diagnosis in Induction Motors Through Thermal Mapping Produced by the RDTS System," in **IEEE Sensors Journal**, vol. 21, no. 18, pp. 20061-20068, 15 Sept.15, 2021, doi: 10.1109/JSEN.2021.3097940.

J. De Pelegrin, U. J. Dreyer, K. M. Sousa and J. C. C. Da Silva, "Smart Carbon-Fiber Reinforced Polymer Optical Fiber Bragg Grating for Monitoring Fault Detection in Bearing," in **IEEE Sensors Journal**, doi: 10.1109/JSEN.2022.3180305.

- Conference Papers

J. d. Pelegrin, J. P. Bazzo, I. B. Vieira da Costa, C. Martelli, D. R. Pipa and J. C. Cardozo da Silva, "Total Variation Deconvolution of Raman Distributed Temperature Sensing Signals,"2019 SBMO/IEEE MTT-S International Microwave and Optoelectronics Conference (IMOC), 2019, pp. 1-3, doi: 10.1109/IMOC43827.2019.9317415.

- Patent Deposit

Dispositivo para medição simultânea de vibração, temperatura e campo magnético rotativo no estator de máquinas elétricas rotativas. Número do Processo INPI: BR 20 2020 001730  
1 Autores/Inventores:PELEGRIN, Jesse de; MARTELLI, Cicero ; SILVA, Jean Carlos Cardozo.

## SUMÁRIO

<b>1</b>	<b>INTRODUCTION . . . . .</b>	<b>10</b>
<b>1.1</b>	<b>Current Perspective and Motivations . . . . .</b>	<b>10</b>
<b>1.2</b>	<b>GENERAL OBJECTIVE . . . . .</b>	<b>15</b>
<b>1.2.1</b>	<b>SPECIFIC OBJECTIVE . . . . .</b>	<b>16</b>
<b>1.3</b>	<b>Thesis Structure . . . . .</b>	<b>16</b>
<b>2</b>	<b>PAPER 01: OPTICAL FIBER SENSOR ENCAPSULATED IN CARBON FIBER REINFORCED POLYMER FOR FAULT DETECTION IN ROTATING ELECTRICAL MACHINES . . . . .</b>	<b>19</b>
<b>3</b>	<b>PAPER 02: SMART CFRP-OFBG FOR MONITORING FAULT DETECTION IN BEARING . . . . .</b>	<b>28</b>
<b>4</b>	<b>PAPER 03: RAMAN DISTRIBUTED TEMPERATURE SENSING FOR END WINDING OF HIGH-POWER GENERATOR . . . . .</b>	<b>37</b>
<b>5</b>	<b>PAPER 04: FAULTS DIAGNOSIS IN INDUCTION MOTORS THROUGH THERMAL MAPPING PRODUCED BY THE RDTS SYSTEM . . . . .</b>	<b>45</b>
<b>6</b>	<b>CONCLUSION . . . . .</b>	<b>54</b>
<b>6.1</b>	<b>General Conclusions . . . . .</b>	<b>54</b>
<b>6.2</b>	<b>SUGGESTIONS FOR FUTURE WORKS . . . . .</b>	<b>56</b>
	<b>REFERÊNCIAS . . . . .</b>	<b>57</b>
	<b>ANEXO A AUTHORIZATION OF JOURNALS FOR THE AVAILABILITY OF ARTICLES . . . . .</b>	<b>63</b>

## 1 INTRODUCTION

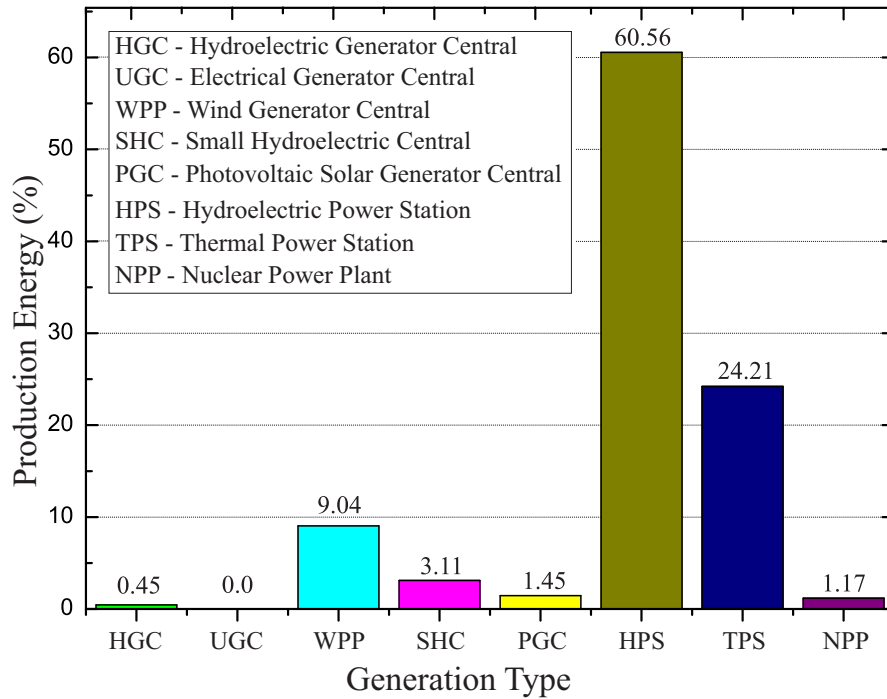
### 1.1 Current Perspective and Motivations

Generators and electric motors are fundamental to electrical energy generation and energy conversion systems. The lifespan of these machines significantly depends on their electrical insulation. Materials that withstand high temperatures and have adequate electrical insulation are used to construct the stator coil windings of these machines for their longevity. However, premature aging may occur owing to vibration and heat caused by bearing failures, voltage imbalances, excessive loads, eccentricities, and phase imbalances (GRUBIC *et al.*, 2008). In Brazil, the industrial sector consumes approximately 43.7 % of the total energy generated. Industrial electrical machines account for 68 % of this consumption. In addition, industrial machinery driven by electric motors consumes approximately 30 % of all electrical energy produced in the country (ANEEL, 2015). Electric generators are the primary machines for generating electricity, whether through hydroelectric, thermoelectric, or wind power (ANEEL, 2020).

Electric generators and motors are essential to socio-economic development. The growth of every economic segment depends on the use of electrical energy to operate machinery and devices. Global energy consumption increased by 3.5 % in 2018, the industrial sector being the largest consumer (ANEEL, 2020). In Brazil, between November 2018 and November 2019, there was a 3.5 % growth in consumption (EPE, 2019). Brazil has approximately 170 GW of installed power, as shown in Figure 1 (ANEEL, 2020). Hydroelectric generators are the primary sources of energy production. The uninterrupted supply of electrical energy comes from the constant operation of electric generators, which stop only for scheduled maintenance.

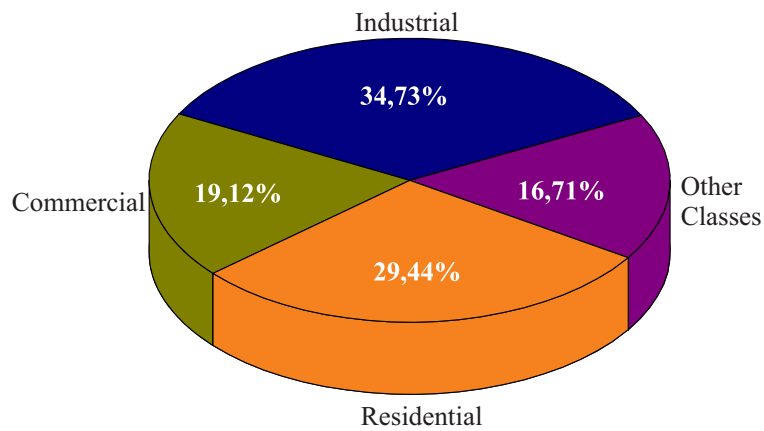
The Empresa de Pesquisa Energética (EPE) publishes monthly data on electricity consumption at the national, regional, and subsystem levels for segments such as residential, industrial, commercial, and others (rural, public service, and public lighting). In 2019, the total energy consumption in the country was 482 million MWh, and the sector-wise consumption (in percent) is shown in Figure 2 (EPE, 2020). Figure 3 shows the main industrial sectors based on their energy consumption (EPE, 2020). The metallurgical industry consumed 28.1 %, followed by the food (16.7 %) and chemical (12.8 %) industries. These energy-intensive industries use electric motors in various capacities to operate hydraulic pumps, agitators, and conveyor belts in the production line. These machines generally run continuously, stopping only for scheduled maintenance. Unexpected stoppages result in financial losses and inconvenience because of interruptions in water distribution, sewage treatment, food production, or electricity supply. Therefore, appropriate maintenance of these machines is crucial. Maintenance can be corrective or preventive: corrective measures are typically costlier than predictive ones. Preventive measures can be further classified into systemic (scheduled) and predictive (based on monitoring). For electric machines, predictive maintenance is the best option because performance is monitored through periodic analysis of physical parameters (CHANG; HONG; CHANG, 2018).

**Figura 1 – Energy production in Brazil according to the type of generation.**

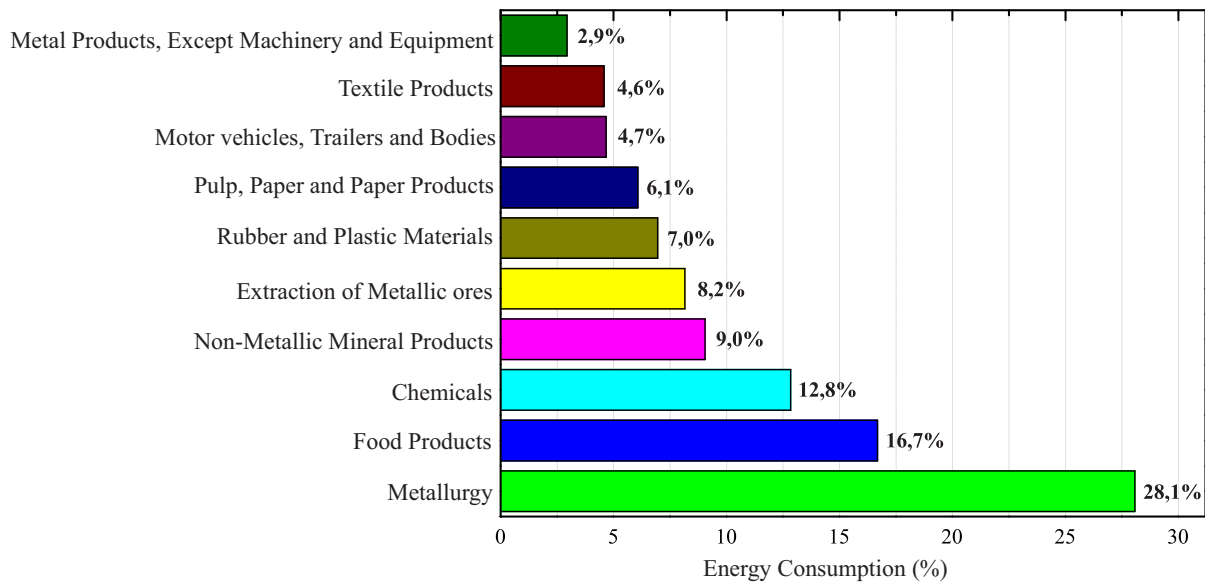


Source: Adapted from <https://www2.aneel.gov.br>  
(Updated on 07/01/22)

**Figura 2 – Energy consumption by residential, industrial, commercial, and other segments (rural, public service, and public lighting) in Brazil.**



Source: Adapted from <https://www.epe.gov.br/pt/publicacoes-dados-abertos/publicacoes>  
(Updated on 07/01/22)

**Figura 3 – Industrial sectors with the highest electricity consumption (2019).**

**Source: Adapted from <https://www.epe.gov.br>  
(Updated on 07/01/22)**

Temperature and vibration are the fundamental parameters to be monitored owing to the internal impact they cause in the machine. According to IEEE recommended practice (IEEE, 2006) 44 % of the failures caused in the three-phase induction motor (TIM) are related to bearings. In theory, through vibration sensing, it is possible to verify whether the bearing is damaged or a bearing element is defective (ORHAN; AKTÜRK; ÇELİK, 2006), (WANG *et al.*, 2018), (HAN Q.AND DING, 2019). The insulation of electrical machines can withstand temperatures between 100 °C and 200 °C. The heat generated during the operation of electrical machines must dissipate into the external environment. Constant temperature monitoring prevents the insulation from deteriorating prematurely and prolongs the life of machinery. The vibration sources in electric rotating machines may be bearing failure, shaft eccentricity, rotor balancing, and electrical voltage imbalance, among others. Excessive vibrations may damage the insulation and cause short circuits between turns and coils (ZHANG *et al.*, 2011).

Previous studies have developed sensors to measure the temperature and vibration in electric motors and generators to identify faults and demonstrated various ways of monitoring these variables (ZHANG, 2015), (BAZZO *et al.*, 2015), (RESENDIZ-OCHOA *et al.*, 2018), (RESENDIZ-OCHOA *et al.*, 2018), (HAN Q.AND DING, 2019), (MOHAMMED; MELECIO; DJUROVIĆ, 2019), (SARKAR *et al.*, 2021). Conventional temperature sensors such as resistance temperature detectors (RTDs) perform point measurements. Such sensors are installed in some parts of the machine: they are installed in slots in generators (HUDON *et al.*, 2013) and between coils in motors (RANSOM; HAMILTON, 2011).

Typically, the temperature is measured only between two coils in motors (WEG, 2019). Therefore, the temperature change must be uniform inside the motor, and it is difficult to detect

the heating source. The sensor is usually inserted on the head of coils in the stator (where the coil wires come out), a region with a higher heat concentration.

Vibration sensors are effective in monitoring the condition of rotating machinery, especially in diagnosing mechanical problems (TSYPKIN, 2017). Vibration data provide essential information about eccentricities, current and voltage imbalances, and problems in stator windings, rotor bars, and core conditions (Kumar; Singh; Naikan, 2018). Vibration sensors gather data using methods based on variable resistance, piezoelectricity, and electrodynamics. In electrical machines, sensors, usually attached to the frame, are used only intermittently. Because, there is no continuous monitoring, defects are not identified early. Many studies have demonstrated the use of external vibration sensors in identifying electrical machine faults, including broken rotor bars (KANOVIC *et al.*, 2013), eccentricities (DEHINA *et al.*, 2019), and faults in the coils (Kumar; Singh; Naikan, 2018), drives (JOKIC; CINCAR; NOVAKOVIC, 2018) and bearings (DALVAND *et al.*, 2014). However, these sensors are susceptible to environmental interference, which compromises measured data.

Another promising line of research employs artificial intelligence (AI) based techniques and classical sensors (YAN *et al.*, 2020). The measurements by sensors act as input data for algorithms that diagnose faults. Lu *et al.* (2020) proposed using convolutional neural networks (CNNs) to diagnose *in situ* engine failures with an embedded system consisting of a Raspberry Pi and signal acquisition and processing circuits. Similarly, Palacios *et al.* (2017) used the discretization of current and voltage amplitude signals in the time domain to identify multiple faults in induction motors. Three types of intelligent classifiers were employed to diagnose engine failures: artificial neural networks, k-nearest neighbor algorithm, and support vector machines with minimal sequential optimization. Regarding mechanical failures, Lee *et al.* (2014) reviewed methodologies that use algorithms and proposed fault analysis through prognostics of rotating machines. Seera *et al.* (2014) proposed an ensemble intelligent hybrid model useful for monitoring induction motor conditions through motor current signature analysis (MCSA). The hybrid intelligent model comprises the fuzzy min-max (FMM) neural network, random forest (RF), and classification and regression tree (CART) models.

In the last decade, several studies have focused on identifying every possible component failure in electrical machines. Generally, the physical parameters like current, voltage, vibration, torque, and magnetic field are measured, and the readings are processed and analyzed through time function, frequency response function (FRF), fast Fourier transform (FFT), predictive torque control (PTC), rotational magnetic field (RMF) analysis, frequency response analysis (FRA), magnetic field signature analysis (MFSA), fuzzy logic, wavelet analysis, or a combination of these. Table 1 presents a summary of research according to fault types and the corresponding analysis methods.

Typically, Hall sensors are used in measurements; as transducers, these sensors detect the magnetic field and convert it into voltage signals using the Hall effect. These signals processed through intelligent algorithms, such as neural networks (BAZAN *et al.*, 2019), have

**Tabela 1 – Bibliographies according to types of failures found in electric rotative machines.**

Types of Faults	Identification Unit	Analysis / Processing	Reference
Bearing	Current	FRF	(FROSINI; BASSI, 2010)
	Vibration	FRF	(IMMOVILLI <i>et al.</i> , 2013)
	Vibration	Neural Networks	(PRIETO <i>et al.</i> , 2013)
	Voltage	FRF	(DALVAND <i>et al.</i> , 2014)
	Vibration	FFT	(ZHANG <i>et al.</i> , 2020)
Rotor	Voltage / Torque	PTC	(NEMEC <i>et al.</i> , 2010)
	External Magnetic Field	FFT	(CEBAN; PUSCA; ROMARY, 2012)
	Current	MCSA	(LEE <i>et al.</i> , 2016)
	Internal Magnetic Field	RMF	(SOLEIMANI; CRUZ; HAGHJOO, 2019)
Stator	Vibration	DFT	(TREML <i>et al.</i> , 2019)
	Current	Fuzzy Logic	(AZGOMI; POSHTAN, 2013)
	Current	3D Ellipse of Currents	(EFTEKHARI <i>et al.</i> , 2014)
	Impedance	FRA	(RATHNAYAKA; SEE, 2017)
	Current	Wavelet	(DEVI; SARMA; RAO, 2016)
Eccentricity	Current	Neural Networks	(BAZAN <i>et al.</i> , 2019)
	Current	MCSA/FFT	(BESSOUS <i>et al.</i> , 2017)
	Current e Torque	Wavelet	(AHMADI; POSHTAN; POSHTAN, 2013)
	Acoustic Noise	Finite Element	(KIM <i>et al.</i> , 2014)
	External Manetic Field	MFSA	(XU; QIU; WU, 2017)
	Internal Magnetic Field	Time	(MIRZAEVA; SAAD, 2018)

been used to identify failures in electrical machines. However, these methods require accurate and instantaneous data, which may be difficult to acquire using conventional sensors. Moreover, electromagnetic interference may limit the functioning of conventional electric sensors. In the case of copper transmission lines using conventional sensors, the distance between the installed sensors and command cabins and the number of sensors are limited.

Optical fiber sensors overcome these difficulties in monitoring temperature and vibration for identifying faults in electrical machines (TWERDOCHLIB; EMERY; BRANDT, 1989), (THEUNE *et al.*, 2002), (BAZZO *et al.*, 2015), (SOUSA *et al.*, 2016), (LINESSIO *et al.*, 2016). The primary advantages of optical fiber sensors over conventional sensors are immunity to electromagnetic interference, high galvanic isolation, and small size (KERSEY, 2000), (MOHAMMED; DJUROVIĆ, 2018). In distributed temperature sensing (DTS), the entire machine can be monitored with only one optical fiber embedded with numerous sensors throughout the structure (HUDON *et al.*, 2013), (BAZZO *et al.*, 2015).

DTS sensors have stimulated several industrial applications, particularly for large systems. Most commercial equipment uses DTS technology. DTS sensors are based on the thermal sensitivity of optical fibers, which act as sensor elements (HU *et al.*, 2011). In this study, sensors based on Raman distributed temperature sensing (RDTS) (hereinafter called RDTS sensors) was used, whose working principle is Raman scattering (BOLOGNINI, 2013). RDTS sensors emit a short-duration laser pulse in optical fiber and analyze the intensity of the backscattered light spectrum through photodetectors. For the temperature measurements, the Stokes and anti-Stokes Raman spectra were considered.

However, a using the RDTS system in small and medium-sized electrical machines is disadvantageous because its spatial resolution is in the order of meters. The spatial resolution of

RDTs sensors indicate the minimum length over which the fiber must be sensitized to guarantee the accuracy of the measurements. The stator size varies according to motor power, and most slot lengths are less than 1 m, which RDTs sensors fail to measure accurately. However, some signal-reconstruction algorithms used with available RDTs sensors may overcome the problem caused by the order of spatial resolution. Some studies have demonstrated that this technique significantly improves the signal (WANG *et al.*, 2018), (SAXENA *et al.*, 2015), (BAZZO J. P.; PIPA, 2016). This thesis presents a signal processing algorithm to improve the spatial resolution of RDTs sensors validated experimentally. This experiment was conducted to identify faults in the busbar of a hydroelectric generator and stator of the induction motor.

In addition to temperature, vibration is another important parameter in the analysis of electrical machines. The RDTs sensors could only monitor the temperature. However, fiber Bragg grating (FBG) sensors can overcome this limitation. Measurements performed with FBG and optical frequency domain reflectometry (OFDR) sensors have numerous advantages owing to the characteristics of the fiber (SOUSA *et al.*, 2012), (MOHAMMED; DJUROVIĆ, 2018) (MOHAMMED; MELECIO; DJUROVIĆ, 2019), (ZHU *et al.*, 2019). OFDR is an optical interrogation technique that allows meticulous analysis of the measured signal (EICKHOFF; ULRICH, 1981). Optical fibers are fragile and should be handled with extreme care, limiting the large-scale deployment of FBG sensors. This study focused on identifying techniques to protect the optical fiber without altering its measurement capacity. One such technique is encapsulating the FBG sensors in carbon fiber reinforced polymer (CFRP) (GALVAO *et al.*, 2018). The properties of carbon fibers, such as their high mechanical strength, low density, and high elastic modulus, make the sensor more robust and adaptable.

Because of these advantages, a sensor integrated into a CFRP was built and a utility model application for this novel system was filed (INPI: BR 20 2020 001730 1). The sensor design, based on the shape of a TIM stator core, was built and tested in an industrial environment. Vibration analyses were performed under actual operating conditions and the effects of the new and used bearings were compared. The frequency analysis results indicated similarity with the theoretical calculations of the bearing defects. Based on the results, this device shows great potential for vibration analysis in electrical machines of any size. This study provides a new technique to prevent significant damage with continuous monitoring of the functional parameters of electric motors and generators.

## 1.2 GENERAL OBJECTIVE

This work aims to develop measurement techniques with optical sensors to monitor temperature, dynamic deformation, voltage imbalance, and eccentricity in rotating electrical machines.

### 1.2.1 SPECIFIC OBJECTIVE

- Experimentally identify the leading causes that generate defects in rotating electrical machines;
- Apply optical sensors without having to change the machine design;
- Evaluate the feasibility of applying distributed optical sensors (DTS) for monitoring the stator temperature of medium and large electrical machines;
- To evaluate the feasibility of applying FBGs sensors integrated into carbon fiber composite to measure temperature and dynamic deformation;
- Develop a sensor based on FBGs integrated into carbon fiber reinforced composite for easy application in rotating electrical machines;
- Implement the sensor developed in induction motors to carry out experimental tests and verify the performance of the proposed device;
- Implement instrumentation (DTS) in the stator slots of the induction motor without interfering with the operating mode;
- Perform dynamic tests on the induction motor, induce failures and analyze instrumentation data in order to identify defects;
- Analyze the experimental results obtained with proposed methods and verify the possibility of making it a predictive maintenance tool for rotating electrical machines.

### 1.3 Thesis Structure

This thesis comprises four papers published in reputable engineering journals. The first two articles focus on FBG sensors encapsulated in CFRP and the last two on DTS sensors.

The first paper presents the design of an FBG sensor encapsulated in CFRP for monitoring rotating electrical machines. The sensor underwent manufacturing, calibration, experimental validation in the laboratory, and testing in an industrial environment. The measurements were carried out at the Induspel Paper Mill (Morretes, PR, Brazil). The new sensor provides data that allow the evaluation of the state of rotating electrical machines during operation based on continuous monitoring of temperature variables and dynamic deformation of the stator. Signal acquisition is a recurring problem in hostile environments. The first article, therefore, focuses on the analysis of bearings. By measuring the dynamic deformation, the frequencies generated by the bearing were diagnosed, and the bearing elements with defects were identified.

The second paper presents a dedicated FBG sensor encapsulated in CFRP for monitoring bearing failures. There are numerous sources of vibration in the industry, such as rotating

electrical machines, compressors, pipelines, transport vehicles, etc. These vibrations can wear out bearings, form cracks, loosen screws, and cause structural failures and short circuits (RAO, 2008). Bearing failures can be divided into two groups: premature and regular steel fatigue failures (IMMOVILLI *et al.*, 2009). Failures are usually attributed to faulty lubrication, improper handling, wrong bearing selection, and carelessness during shaft or housing design (NSK, 2019). In electric motors, the damaged bearing can burn the stator coils and cause an imbalance of the rotor allowing it to touch the stator core and damage the motor. The bearing consists of an outer race, an inner race, a rolling element, and a cage. When these constituent elements become defective, they cause an increase in vibrational energy. This increase appears as a pulse at a single frequency and can be determined from the dimensions of the bearing (ORHAN; AKTÜRK; ÇELİK, 2006). In electrical machines, vibration analysis is an excellent technique for monitoring the operating conditions and identifying faults at a stage that precedes major damage (JANDA; MAKKI; KONICEK, 2014). Studies related to vibration monitoring have mostly focused on identifying machine faults, detecting excessive vibration levels, and determining when to shut down the machine to avoid possible damage caused by severe vibration. The measured vibration data can be compared to a standard of vibrations (RILEY *et al.*, 1999). Vibration sensors available on the market can be installed in the machine housing. However, this region is susceptible to interference from external oscillations. The difference between the developed FBG sensor and the conventional sensor is the position where they are installed. The developed sensor is installed in contact with the bearing under examination, allowing early detection of faults.

The third paper discusses monitoring with DTS sensors to identify hot regions of the stator bar of a 355 MW hydroelectric generator in the laboratory. Although this method has limitations in terms of spatial resolution, a technique that applies reconstruction algorithms to the measured signal was implemented, validated, and experimentally tested. The results indicate the possibility of measuring the temperature every 15 cm from the end of the bar where the optical fiber is installed. The region of the coil heads where connection closures are performed is an important area for temperature monitoring. With hundreds of interconnected bars and anti-vibration shims, the heads of the coils form a complex region to maintain adequate ventilation. High temperatures above 100 °C in the stator bars limit the useful life of insulating materials (KOKKO, 2012). Overheating can damage the insulation system, causing critical generator failure (LIU *et al.*, 2007), (WANG *et al.*, 2018). To avoid installing dozens or hundreds of conventional sensors, DTS is a plausible technique for monitoring each bus with as many points as possible.

The fourth article presents the diagnosis of faults and voltage imbalances in an electric motor through thermal mapping by RDTS sensors. Motors heat naturally because of the Joule heating. The electric current flowing through the coils produces heat, which is dissipated outside the motor housing with help of a fan mounted on the motor shaft. The wind produced by the fan is directed by the deflector cover through the fins, removing hot air. Adequate dissipation depends on the efficiency of the ventilation system, total dissipation area of the housing, and temperature difference between the external surface of the housing and ambient air ( $T_{ext} - T_a$ ) (WEG, 2019).

According to the Weg Specifications Guide, obtaining the winding temperature with conventional sensors is difficult because of the temperature difference between any two points on the motor . The maximum operating temperatures allowed for the induction motors are defined according to ABNT NBR 17094, and IEC 60034-1 (IEC, 2010). The temperature exceeding this thermal limit causes gradual insulation degradation in motors and reduces their expected life. According to Pawlus (PAWLUS; KHANG; HANSEN, 2017), the life of a motor is reduced by 50 % for each increase of 10 °C above the thermal limit.

## **2 PAPER 01: OPTICAL FIBER SENSOR ENCAPSULATED IN CARBON FIBER REINFORCED POLYMER FOR FAULT DETECTION IN ROTATING ELECTRICAL MACHINES**

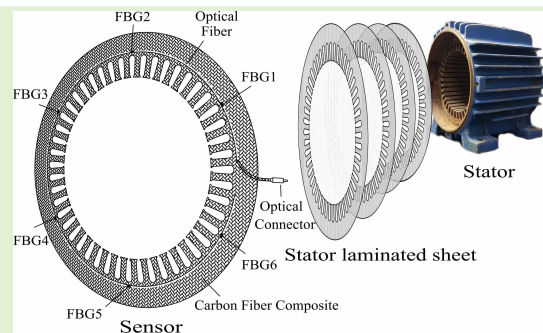
J. de Pelegrin, U. J. Dreyer, C. Martelli and J. C. C. da Silva, "Optical Fiber Sensor Encapsulated in Carbon Fiber Reinforced Polymer for Fault Detection in Rotating Electrical Machines," in IEEE Sensors Journal, vol. 20, no. 19, pp. 11364-11371, 1 Oct.1, 2020, doi: 10.1109/JSEN.2020.2997597.

# Optical Fiber Sensor Encapsulated in Carbon Fiber Reinforced Polymer for Fault Detection in Rotating Electrical Machines

Jessé de Pelegrin, Uilian José Dreyer, Cicero Martelli, and Jean Carlos Cardozo da Silva<sup>1</sup>

**Abstract**—This paper introduces a novel fiber-based sensor for dynamic strain and temperature measurements in the stator of rotating electrical machines. Fiber Bragg grating sensors were integrated into carbon fiber reinforced polymer. The encapsulation has appropriate mechanical energy transfer to measure dynamic strain and temperature. The proposed sensor is installed in the stator of the induction motor allowing to analyze the dynamic strain generated by the machine. The main failure in induction motors is attributed to bearing failures. In this work, the tests were performed operating at full load with new and defective bearings. The results show the main peaks of frequency caused by strain observed coincide with the electrical supply frequency (60 Hz) and mechanical bearing forces (30 Hz), with harmonic components at 120, 180, and 240 Hz. However, for the damaged bearings frequencies of 89.8, 116.5, 146.4, and 149.7 Hz were identified. These frequency components were generated by defects in the outer race, rolling element and inner race. The fundamental components of 30 and 60 Hz between the new and damaged bearings presents an increase of more than 75 %. Results show the potential of the proposed sensor in the monitoring of temperature and dynamic strain in electrical machines.

**Index Terms**—Carbon fiber reinforced polymer, fiber Bragg gratings, rotative electrical machine, dynamic strain and temperature sensing.



## I. INTRODUCTION

**E**LECTRIC generators and motors are fundamental elements in the electromechanical energy conversion process. Approximately 40 % of the total global consumption of energy can be attributed to electric motors [1]. The global power generation matrix is based on rotating electrical machines. Therefore, it is very important to operate these machines for as long as possible.

The identification of faults in rotating electrical machines has been the focus of considerable research interest over the

last 30 years [2]. Such faults are often caused by premature aging, which occurs due to vibrations and excessive heat caused by bearing failures, electrical voltage imbalance, overload, and eccentricity [3]–[6].

With an increase in the production of electric vehicles [7] and wind turbines [8], along with the use of machines in the industrial sector, new research is being conducted to improve energy efficiency and prevent machine failure. Three-phase induction motors (TIM) represent about 68 % of the electricity consumed in the Brazilian industrial sector [9].

According to an IEEE study [10], 44 % of failures in TIMs can be attributed to bearing faults, 26 % to stator faults, 8 % to rotor faults, and 22 % to other factors. Several studies have proposed methods to monitor machines to predict possible failures. Glowacz and Glowacz [11] used thermal image processing with neural networks to identify machine failures through analysis and comparison. Dalvand *et al.* [12] used the frequency component analysis of the machine's electrical supply voltage to identify bearing failures. Similarly, Giantomassi *et al.* [13] and Han *et al.* [14] used spectral analysis of the electric current to identify motor failures. Although these studies have proposed solutions for monitoring electrical machines, there are some difficulties in implementing them in the industrial sector. To obtain a thermal

Manuscript received April 22, 2020; revised May 21, 2020; accepted May 22, 2020. Date of publication May 25, 2020; date of current version September 3, 2020. This work was supported in part by the CAPES—Coordenação de Aperfeiçoamento de Pessoal de Nível Superior, in part by the CNPq—Conselho Nacional de Desenvolvimento Científico e Tecnológico, in part by the FINEP—Financiadora de Estudos e Projetos, in part by the Fundação Araucária, in part by the SETI—Secretaria da Ciência, Tecnologia e Ensino Superior, in part by the Federal Institute Catarinense—IFC, and in part by the Federal University of Technology—Paraná (UTFPR). The associate editor coordinating the review of this article and approving it for publication was Dr. Carlos Marques. (Corresponding author: Jean Carlos Cardozo Da Silva.)

The authors are with the Graduate Program in Electrical and Computer Engineering, Federal University of Technology-Paraná, Curitiba 80230-901, Brazil (e-mail: jesse.pelegrin@ifc.edu.br; uilian-dreyer@utfpr.edu.br; cmartelli@utfpr.edu.br; jeanccs@utfpr.edu.br).

Digital Object Identifier 10.1109/JSEN.2020.2997597

1558-1748 © 2020 IEEE. Personal use is permitted, but republication/redistribution requires IEEE permission. See <https://www.ieee.org/publications/rights/index.html> for more information.

image, it is necessary to easily access an electrical machine, which is generally not possible in industrial plants. In the case of voltage and current analysis, these components are susceptible to electrical network noise. Depending on the type of machine start-up, the results can differ due to the high inertia loads. This condition generates voltage fluctuations and noise in the electrical network [15].

Other types of sensors have gained popularity in recent years. This work is focused on optical fiber sensors, which have properties that are essential for electrical machine applications, such as small dimensions, fast responses, and immunity to electromagnetic interference. Generally, optical sensors are applied to measure temperature and strain to indicate possible machine failures. To check for rotor broken bars, Sousa *et al.* [16] used optical fiber Bragg grating (FBG) sensors installed in the stator tooth to analyze the frequency characteristics between a rotor in good condition and that with a broken bar. To identify faults in the stator, Mohammed *et al.* [17], [18] installed FBGs inside the grooves and between the coil turns to observe thermal behavior. For temperature distribution and vibration, among other physical quantities, Fabian *et al.* [19] presented a FBG-based system allowed for the simultaneous monitoring of the machine.

Commercial electrical sensors, which are used in vibration measurement, are installed on the outside of electrical machines. Owing to their high cost, they are only used in specific applications [20]. In such cases, measurements must be made with the system in operation, which makes performing the task difficult and puts the person responsible for the measurement at risk. In industrial areas of great product demand as electric generation, mining, and water/sewage treatment, the electric machines are frequently unavailable due to its importance within the process. In such cases, there must be an online detection tool for measurements to take place even during the uninterrupted machine operation.

Since the bearing faults are the major reasons for the failure of the TIM, the sensor was developed to identify these faults. The FBG is sensitive to shear; the fiber was encapsulated in CFRP, which allows for higher stress limits, flexibility and fracture resistance [21]. The encapsulation of the FBG influences the sensitivity of the sensor. However, some compensation methods can be used [22], [23]. Since the optical fiber and the CFRP in which it is embedded have different material properties, strain in both materials will not be equal when load is applied [24]. The measurements with the proposed sensor are intended to identify the difference between TIM in good condition and with defects, so the encapsulation does not influence the results.

This paper is organized as follows: Section II presents the theoretical analysis of the bearings. Section III presents the materials and methods with the development of the sensor, which includes FBGs integrated into a carbon fiber composite material, its calibration and installation, and tests on the TIM applied in an industrial plant environment. Section IV presents the results and discussion of the measurements made with the proposed sensor during two specific conditions: one with new

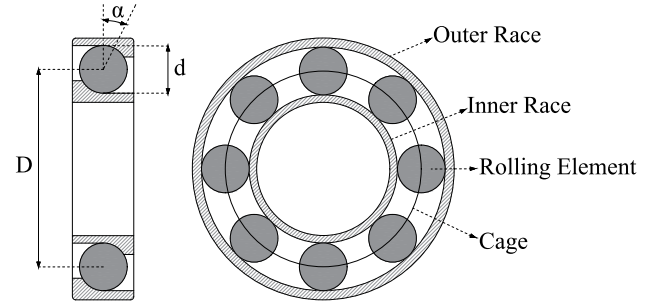


Fig. 1. Mechanical construction of the rolling bearing.

bearings and one with faulty bearings. Section V presents the conclusions.

## II. THEORETICAL ANALYSIS

A TIM may exhibit undesirable behavior during operation due to problems of electrical, magnetic, or mechanical origin. These defects can be detected by analyzing the frequencies in the electromechanical vibration spectrum of the machine [25]. Problems of electromagnetic origin are caused by voltage imbalance between the phases, failures in the stator winding, dynamic, and static eccentricity that cause variations in the magnetic flux [26]. Mechanical problems are related to imbalance, misalignment, and mechanical looseness, usually caused by bearing failure. In this paper, bearings faults are addressed in the bearings and their associated frequencies.

The bearing comprises an inner race, outer race, rolling element, and cage, as shown in Fig. 1. Each part introduces a frequency element within the vibration spectrum. Radially loaded rolling element bearings generate vibrations even if they are geometrically perfect. It happens due to the use of finite rolling elements. The bearing races generate vibrations owing to a change in the direction of the contact forces applied by the rolling elements [27]. Hence, it is possible to calculate the natural frequency from the bearing's geometric dimensions and operating conditions.

In TIM, the rolling element bearings are commonly used to provide rotor support [28]. Each bearing element has a characteristic rotation frequency which can be calculated using equations 1, 2, 3, and 4 [29]:

$$F_c = \frac{f_r}{2} \left[ 1 - \frac{d}{D} \cos(\alpha) \right], \quad (1)$$

$$F_{re} = f_r \left( \frac{d}{D} \right) \left[ 1 - \frac{d^2}{D^2} \cos^2(\alpha) \right], \quad (2)$$

$$F_{ir} = N_b \frac{f_r}{2} \left[ 1 + \frac{d}{D} \cos(\alpha) \right], \quad (3)$$

$$F_{or} = N_b \frac{f_r}{2} \left[ 1 - \frac{d}{D} \cos(\alpha) \right], \quad (4)$$

where  $F_c$  is the cage fault frequency,  $F_{re}$  is the rolling element fault frequency,  $F_{ir}$  is the inner raceway fault frequency,  $F_{or}$  is the outer raceway fault frequency,  $N_b$  is the number of rolling element,  $d$  is the diameter of the rolling element,  $D$  is the

pitch diameter,  $\alpha$  is the contact angle, and  $f_r$  is the rotational frequency [29].

Bearings can have defects such as roughness, waviness, misaligned races, off-size rolling elements, cracks, pits, and spalls on the rolling surfaces [28]. The presence of defects causes a significant increase in the level of mechanical vibration in the amplitude of spectral components. Through the spectral analysis of vibration, it is possible to determine the wear level of the bearings. For a vibration sensor to identify the beginning of the problem, it must perform continuous monitoring. In this paper, a robust optical fiber sensor that is intrinsic to the electric machine was developed to measure the dynamic strain and temperature.

### III. MATERIALS AND METHODS

#### A. Sensor Development

The proposed sensor consists of FBGs recorded in optical fibers that are integrated into a carbon fiber composite material. FBG is a periodic refractive index modulation into the fiber core inscribed when it is exposed to a transversal UV light interference pattern of laser light [30]–[32]. According to Bragg's law, a fraction of the incident power is reflected around the Bragg wavelength, which is given by:

$$\lambda_B = 2\Lambda n_{eff}, \quad (5)$$

where  $n_{eff}$  is the effective refractive index of the fiber in the fundamental mode in which the FBG is imprinted and  $\Lambda$  is the period of the refractive index modulation of the FBG [33].

The wavelength reflected by the FBG structure shifts with a variation in the strain and/or temperature to which it is exposed. The wavelengths reflected by the grating to change; these wavelengths change with the variation in the mechanical deformation ( $\Delta\epsilon$ ) and temperature ( $\Delta T$ ) to which they are exposed. Equation 6 represents the displacement of the Bragg wavelength ( $\Delta\lambda_B$ ) [34],

$$\Delta\lambda_B = \lambda_B [(\alpha_f + \zeta)\Delta T + (1 - \rho)\Delta\epsilon], \quad (6)$$

where  $\alpha_f$  is the thermal expansion coefficient, which has a typical value of  $0.55 \times 10^{-6} \text{ }^\circ\text{C}^{-1}$ , for silica. The term  $\zeta$  represents the thermo-optic coefficient ( $\approx 6 - 9 \times 10^{-6} \text{ }^\circ\text{C}^{-1}$ ) and  $\rho$  is the photoelastic coefficient that represents the physical elongation of the fiber [30].

The FBGs were recorded using the phase mask technique onto a Ge-doped photosensitive fiber (fiber type: GF1, (SMF) Nufern®). The FBGs were written using an excimer laser (Xantos XS 500 - 193 nm-XS-L Coherent®) as the ultraviolet (UV) light source with 25 W, 5 ns pulses, frequency ranging from 250 to 300 Hz, and pulse energy ranging from 3 to 4.5 mJ/pulse. A total of six FBGs were written with different wavelengths (1526, 1532, 1537, 1550, 1556, and 1560 nm).

In order to protect the FBGs, the optical fiber was integrated between two layers of carbon fiber composite of both bidirectional and unidirectional carbon-fiber fabric twill type ( $200 \text{ g/m}^2$ ) and epoxy resin (331), and thermosetting type with hardener (043), manufactured by Dow Chemical Company. The carbon fiber reinforced polymer (CFRP) has a low

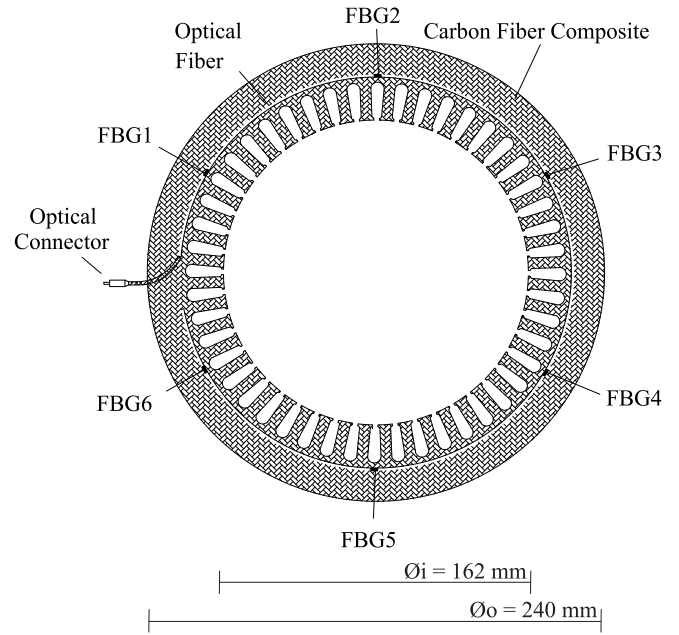


Fig. 2. Diagram of the developed sensor with six evenly distributed FBGs integrated in CFRP.

coefficient of thermal expansion of approximately  $1.10^{-6}/^\circ\text{C}$  [35], [36]. The elasticity coefficient depends on the number of layers of the CFRP; for two layers, it corresponds to 3.8 GPa [37].

The first layer of the carbon fiber was impregnated with epoxy resin, hermetically sealed, and heated to perform the curing process. A vacuum pump removed the air particles while the compound was cured at  $120 \text{ }^\circ\text{C}$  for 8 h. This first layer was cut into the shape of the stator core plates and is the basis for positioning the FBGs. The FBGs were evenly distributed, as one can see in Fig. 2. The second layer of the CFRP is placed over the first layer with the FBGs and underwent the same vacuum curing process.

The encapsulation has the mechanical energy transfer characteristics appropriate for measuring vibration and temperature [21]. This format assisted in measurements and facilitated installation in the machine's core. Fig. 2 shows the model of the sensor built with six FBGs integrated into the CFRP and an optical connector.

#### B. Calibration

To verify the sensor's behavior integrated into the carbon fiber, a sample of a sensor with the same characteristics was subjected to thermal analysis. For thermal characterization, it was used a LAUDA model ECO RE415 thermal bath. Data acquisition was performed using the SM130 optical interrogator, manufactured by Micron Optics, which has a sample rate of 1 kHz. The sample was subjected to thermal variation in the range of  $20\text{--}90 \text{ }^\circ\text{C}$  at intervals of  $5 \text{ }^\circ\text{C}$ . Four repetitions were performed, and the average of the points obtained was linearly adjusted. This generated a correlation coefficient of 0.99821. The thermal sensitivity was found to be  $0.00526 \text{ nm}/^\circ\text{C}$ .



Fig. 3. Experimental setup in field with pump and motor used for water treatment.

The temperature sensitivity of an FBG is normally between 8 and 12  $pm/^\circ C$  [33]. For encapsulated FBG sensors, the temperature sensitivity is influenced by the material used to integrate the sensor [38]. That is why the found thermal sensitivity in this work differs from the one found in the literature.

The electrical machine's internal temperature is related to the silicon steel sheets that make up the stator core. These sheets present a thermal expansion coefficient of  $11.9 \times 10^{-6}/^\circ C$  at temperatures between 20 and 100  $^\circ C$  [39]. Considering the thermal expansion of the CFRP [21] and the core plates, the average expanded uncertainty was 5  $pm$ , which corresponded to 1  $^\circ C$ . This uncertainty was sufficient to monitor the TIM temperature, as the thermal limits for the insulation classes presented this magnitude [17], [40].

### C. Industrial Plant Tests

The developed sensor was applied to a TIM operating in a recycled paper processing plant. The motor is coupled to a pump that recirculates the water through a closed-loop system, thereby avoiding environmental contamination. This plant plays an important role as being environmentally friendly; its production depends exclusively on recycled paper, and it operates at the lowest possible water consumption levels. During recycled production, all the water removed is reused after treatment. Fig. 3 shows the motor, pump, and tank. The hydraulic pump must not be inoperative for more than two consecutive hours; otherwise, production problems may occur.

The motor operates in a hostile environment and is exposed to high humidity. Thus, the bearings suffer frequent wear, requiring constant replacement to avoid damage to the motor and losses in production. The bearings of this motor are replaced every 6 months following a preventive maintenance procedure.

In this study, the spare motor was used to install the sensor integrated with the composite. The motor underwent a reconditioning process, enabling instrumentation with the proposed sensor in the stator core. Table I presents the parameters of the TIM.

TABLE I  
PARAMETERS OF INDUCTION MOTOR

Rated Power	14920 W (20 Hp)
Poles	4
Rated Voltage	380 V
Rated Current	30 A
Frequency	60 Hz
Speed	1755 rpm

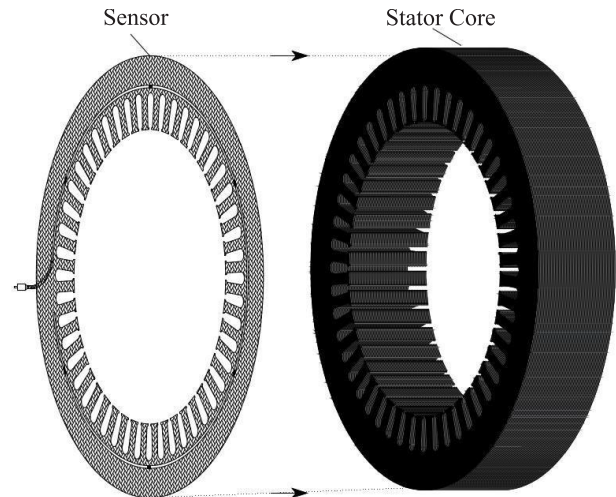


Fig. 4. Schematic of the sensor installation on the TIM stator core.

The sensor was fixed to the stator core using Araldite LY5052 epoxy resin and HY5052 amine hardener with a mixture ratio of (LY) 100: 40 (HY) parts by weight, parallel to the core, as shown in Fig. 4. The bonding was performed in the entire contact area of the core and the sensor, including the stator tooth, which provided greater sensitivity in measuring vibration and temperature. The schematic drawing of the experimental setup with the acquisition, optical interrogator, FBG sensor encapsulated in CFRP, and sensor attached to the TIM stator core are shown in Fig. 5. It can be seen from the shape of the sensor that it does not interfere with the stator reconditioning process, which is one of the advantages of this sensor. In addition to the shape, the thickness of the sensor (2 mm) aids in avoiding space loss inside the motor without the invasive effect that other conventional sensors can cause. For this motor, the coils have a 1:10:12 pass and are inserted concentrically in the grooves. At the end of the reconditioning process, the bearings were replaced, and the motor was tested.

Firstly, the motor was started under no-load conditions. This first test aimed to verify the simultaneous behavior of dynamic strain and temperature. Fig. 6 shows the measurements made by one of the FBGs during motor startup. Initially, the motor was not running, and the temperature measured was 22  $^\circ C$ . The motor started at 1.6 min; it was operated until 3.4 min and then turned off. When starting the motor, the sensor detected temperature and strain quick transient that is related to the moment of inertia of the rotor. During operation, the measured signal increased until the motor was switched off. The temperature measured by the sensor shifts of 12  $^\circ C$  was expected according to the thermal characteristics on the

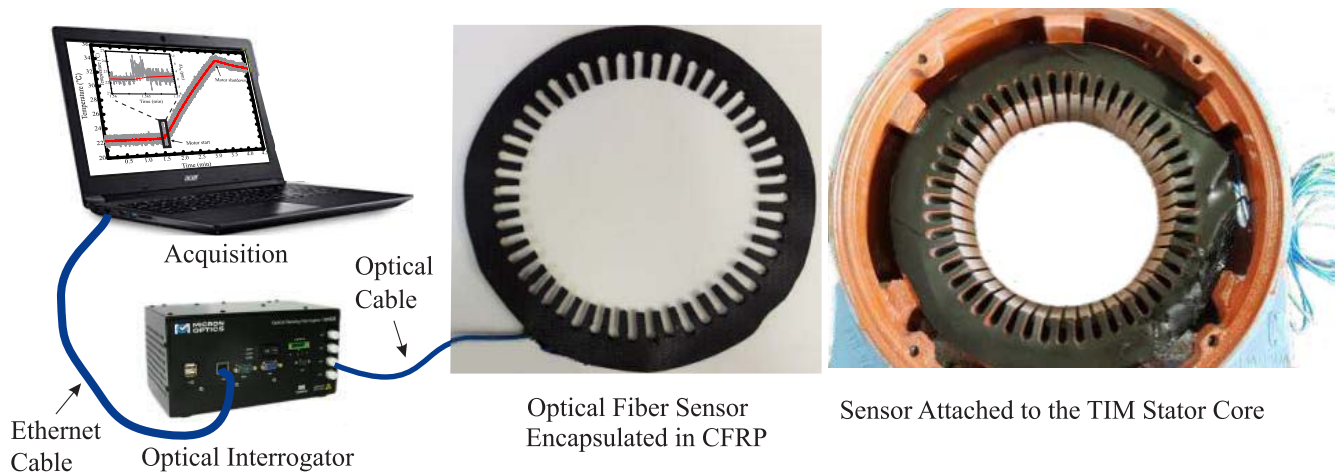


Fig. 5. Schematic drawing of the experimental setup with acquisition, optical interrogator, FBG sensor encapsulated in CFRP and sensor attached to the TIM stator core.

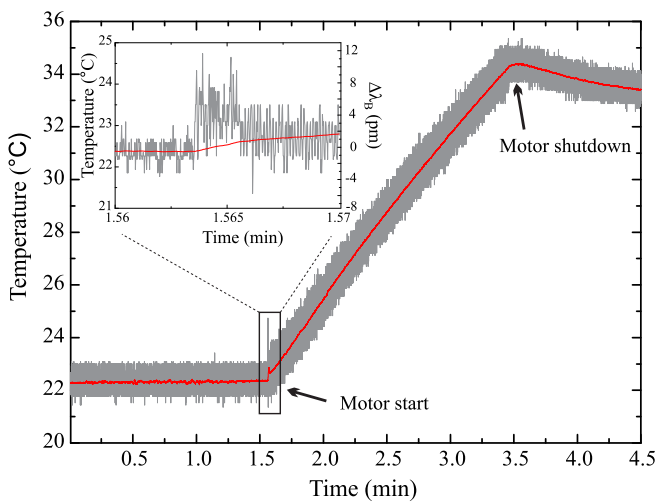


Fig. 6. Graphic showing the temperature and strain variation during a no load test of the instrumented TIM.

empty machine. In particular, a difference in the amplitude of dynamic strain in the motor between the turn off state and the running state was evident.

With the motor coupled to the hydraulic pump, tests were carried out initially with new bearings and then with damaged bearings. In the faulty bearing, visible defects are identified as ball fault (oxidation), inner raceway damage (broken), and outer raceway damage (snap), as shown in Fig. 7. The faulty bearings used are from the motor before reconditioning with six months of operation. Bearing 6309 had greater deterioration because of the motor side of the hydraulic pump connection.

Each part of the bearing construction contributes to a certain frequency component of the vibration spectra. Table II presents the physical dimensions of the bearings 6209 and 6309. Applying the data from each bearing in the equations 1-4, the following frequencies can be determined for each bearing: For bearing 6209, the following were obtained:  $F_c = 11.66$  Hz,  $F_{re} = 142.43$  Hz,  $F_{ir} = 138.71$  Hz

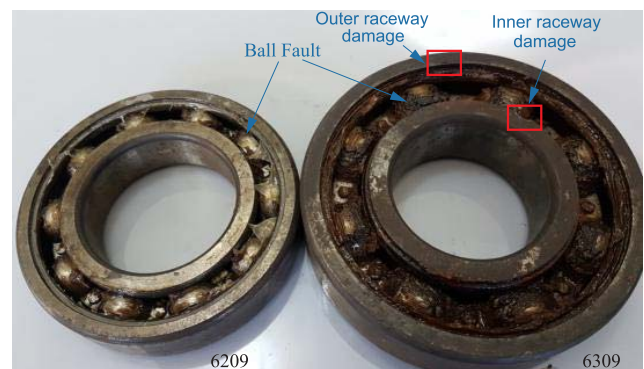


Fig. 7. Image of 6209 and 6309 ball bearings with visible defects identified: ball fault (oxidation), inner raceway damage (broken), and outer raceway damage (snap).

TABLE II  
PARAMETERS OF INDUCTION MOTOR BEARINGS

Parameters	Types of Bearings	
	6209	6309
Number of Balls ( $N_b$ )	8	8
Ball diameter ( $d$ )	13 mm	17.6 mm
Outer diameter ( $O_d$ )	75.19 mm	86.7 mm
Inner diameter ( $I_d$ )	57.60 mm	62.18 mm
Pitch diameter ( $D = (O_d + I_d)/2$ )	66.39 mm	74.44 mm
Contact angle ( $\alpha$ )	0	0

and  $F_{or} = 93.28$  Hz. For bearing 6309, the following were obtained:  $F_c = 11.16$  Hz,  $F_{re} = 116.79$  Hz,  $F_{ir} = 144.66$  Hz and  $F_{or} = 89.33$  Hz.

Moreover, the tests performed with faulty and good bearings were carried out with direct start-up of the motor. The current supply was kept at 30 A by controlling the pump-tank water flux valve with this intention. The supply current was maintained at 30 A, which was possible due to the regulation of the opening of the pump valve.

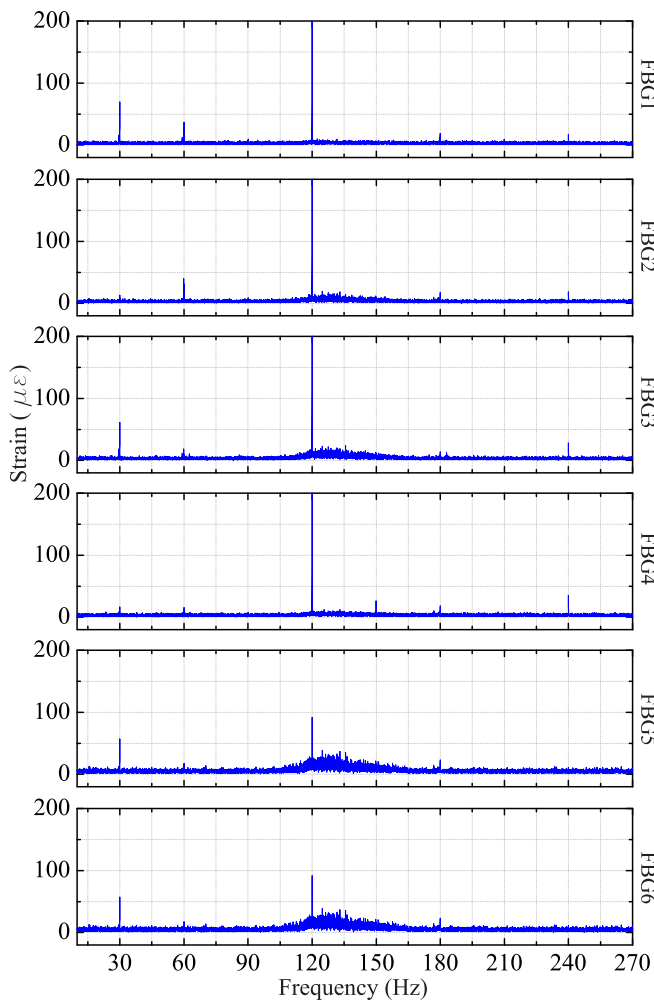


Fig. 8. Frequency response of the six FBGs that constitute the sensor installed on the motor with new bearings.

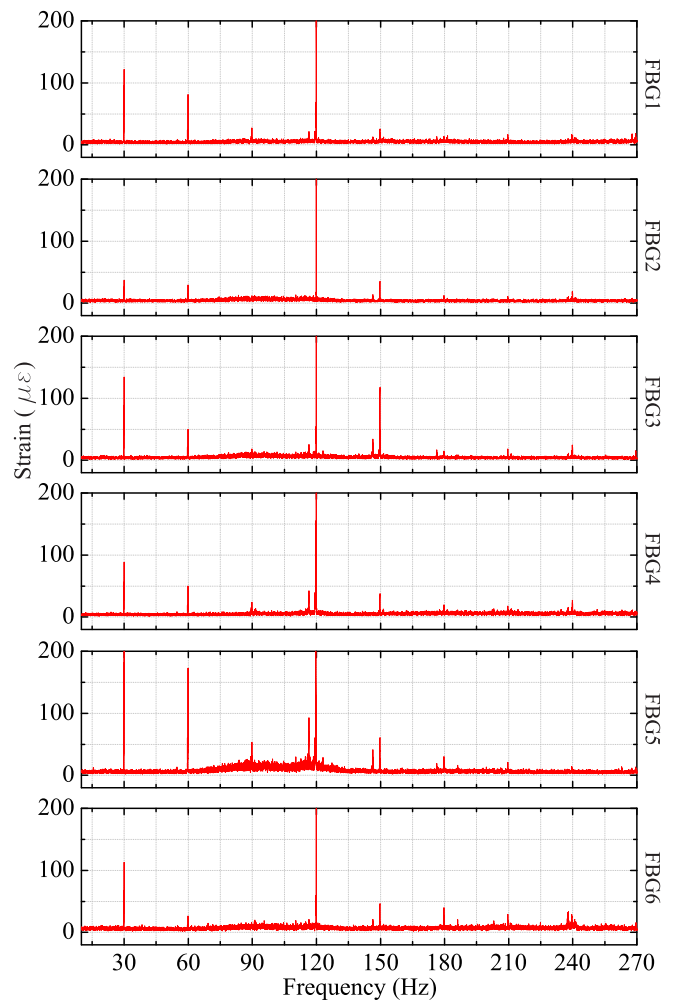


Fig. 9. Frequency response of the six FBGs that constitute the sensor installed on the motor with damaged bearings.

#### IV. RESULTS AND DISCUSSION

The frequency response of the six integrated FBG sensors measuring vibration with new bearings is shown in Fig. 8. It is possible to note that the frequencies that stood out are only those of the mechanical origin at 30 Hz, electrical origin at 120 Hz, and its harmonic components at 60, 180, and 240 Hz [26], [33]. In FBG5 and FBG6, the signal amplitude at 120 Hz was smaller than the others, likely due to the fixation position in the carbon fiber impregnation process. There were no other frequency components observed as the bearings were new.

The results with the faulty bearings are shown in Fig. 9. A comparison of the measurements between the new and the damaged bearings showed that in the 6 FBGs, there was an increase of up to 130 % (FBG3) in the amplitude of the mechanical frequency (30 Hz) and up to 100 % (FBG5) in the electrical frequency (120 Hz). In addition to the frequencies of 30 and 120 Hz, new components were identified at 89.8, 116.5, 146.4, and 149.7 Hz.

The new frequency components appeared due to the faults in the components of the damaged bearings. The six integrated FBGs presented these frequencies, and the signals

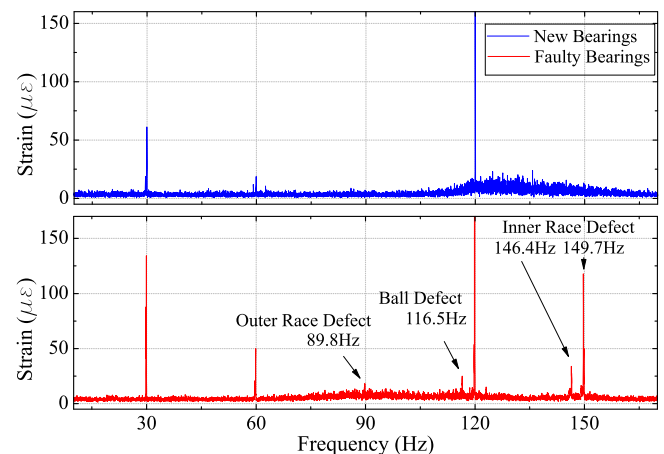


Fig. 10. Comparative analysis of the results between the new and damaged bearings loaded with sensor FBG3.

from FBG3 and FBG5 were analyzed to assess the strain in two different phases. Fig. 10 shows the measurements made with FBG3 using both new and damaged bearings, where the components appeared due to the outer race defect at 89.9 Hz,

TABLE III  
CALCULATED FREQUENCIES AND MEASUREMENTS  
OF THE ELEMENTS THAT MAKE UP THE BEARINGS

Frequency of each element	Types of Bearings			
	6209		6309	
	Calculated	Measured	Calculated	Measured
$F_c$	11.66 Hz	-	11.16 Hz	-
$F_{re}$	142.43 Hz	146.4 Hz	116.79 Hz	116.5 Hz
$F_{ir}$	138.71 Hz	-	144.66 Hz	149.7 Hz
$F_{or}$	93.28 Hz	-	89.33 Hz	89.89 Hz

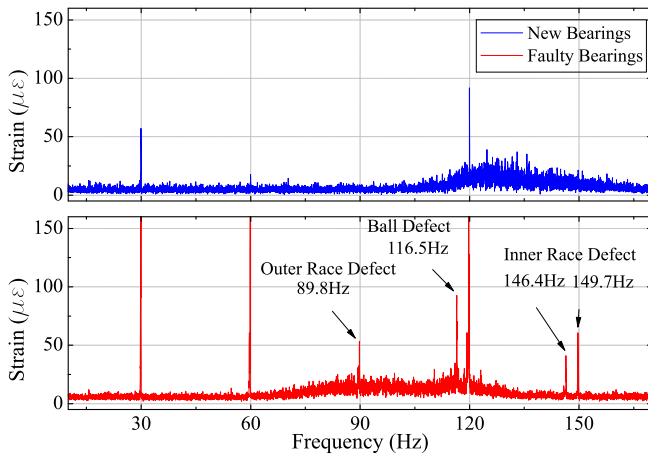


Fig. 11. Comparative analysis of the results between the new and damaged bearings loaded with sensor FBG5.

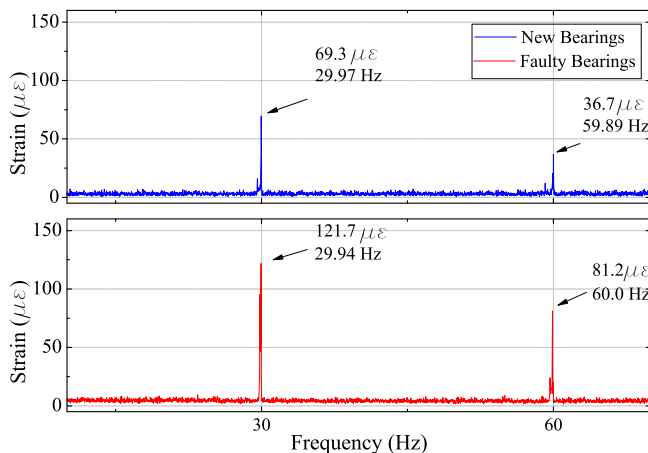


Fig. 12. Comparative analysis of the results between the new and damaged bearings loaded with the sensor FBG1.

ball defect at 116.5 Hz, and inner race defect at 146.4 and 149.7 Hz. Fig. 11 shows the FBG5 frequency response for the damaged bearings; the outer race defect and ball defect presented a strain of  $52 \mu\epsilon$  at 89.8 Hz and  $83 \mu\epsilon$  at 116.5 Hz, respectively. A comparison between the frequencies calculated by the dimensions of the bearings and the frequencies measured by the sensor is shown in Table III. The cages of both bearings did not present frequency measurements. For the bearing 6209, the inner race and the outer race also did not identify any frequencies; this implies that these elements had no defects.

As shown in Fig. 12 the strain at a frequency of 29.97 Hz was  $69.3 \mu\epsilon$  for the new bearings and increased to  $121.7 \mu\epsilon$ , for the damaged bearings; an increase of 75.6 %. Strain at the frequency of 59.89 Hz was  $36.7 \mu\epsilon$  for the new bearings. For the damaged bearings, the frequency shifted to 60 Hz, and the strain was  $81.2 \mu\epsilon$ , which was approximately 121 % higher.

## V. CONCLUSION

In this paper, a new sensor based on fiber optics integrated into a carbon fiber composite material was presented. The developed sensor was installed in the core of a TIM during its reconditioning process. In this condition, the sensor is protected from external interference, environmental noise. These results were obtained in an industrial environment under real operating conditions. The tests were carried out in two situations: one with new bearings and one with damaged bearings. The dynamic readings showed results that helped identify the faults in the elements that made up the bearings. The strain levels between the new and the damaged bearings were measured through the frequency spectrum. For the new bearings, the sensor measured only the mechanical (30 Hz) and electrical (120 Hz) frequencies. However, for the damaged bearings, the sensor identified frequencies at 89.8, 116.5, 146.4, and 149.7 Hz, which corresponded to the defects in the elements that comprised the bearings. Using the fault detection bearing theory, the frequencies generated by each bearing element were calculated. The frequencies measured by the sensor coincided with match the calculated frequencies. Therefore, the proposed sensor showed to be able to identify the defects in the inner race, outer race and rolling element. Also, at the mechanical frequency of 30 Hz, there was an increase of up to 130 % and electrical frequency of 120 Hz, there was an increase of up to 100 %.

This sensor can be used in all rotating electrical machines, as it can be built in any radial dimension. Moreover, because it has a 2 mm thickness, it is adaptable to the designs of existing machines. Its intrinsic installation in electric machines allows dynamic and safe monitoring for the operator. New research is needed regarding the diagnosis of failures in electrical machines. This sensor offers a promising solution for the identification of eccentricity behavior, phase imbalance, rotating magnetic fields, and rotor bar failures.

## REFERENCES

- [1] S. Hesari and M. B. N. Sistani, "Efficiency improvement of induction motor using fuzzy-genetic algorithm," in *Proc. 30th Int. Power Syst. Conf. (PSC)*, Nov. 2015, pp. 210–216, doi: 10.1109/IPSC.2015.7827750.
- [2] H. Henao *et al.*, "Trends in fault diagnosis for electrical machines a review of diagnostic techniques," *IEEE Ind. Electron. Mag.*, vol. 8, p. 31–42, Jun. 2014, doi: 10.1109/MIE.2013.2287651.
- [3] S. Grubic, J. M. Aller, B. Lu, and T. G. Habetler, "A survey on testing and monitoring methods for stator insulation systems of low-voltage induction machines focusing on turn insulation problems," *IEEE Trans. Ind. Electron.*, vol. 55, no. 12, pp. 4127–4136, Dec. 2008.
- [4] M. Drif and A. J. M. Cardoso, "Stator fault diagnostics in squirrel cage three-phase induction motor drives using the instantaneous active and reactive power signature analyses," *IEEE Trans. Ind. Informat.*, vol. 10, no. 2, p. 1348–1360, May 2014.
- [5] P. G. Kini and R. C. Bansal, "Effect of voltage and load variations on efficiencies of a motor-pump system," *IEEE Trans. Energy Convers.*, vol. 25, no. 2, pp. 287–292, Jun. 2010, doi: 10.1109/TEC.2009.2032628.

- [6] K. M. Sousa, U. J. Dreyer, C. Martelli, and J. C. Cardozo da Silva, "Dynamic eccentricity induced in induction motor detected by optical fiber Bragg grating strain sensors," *IEEE Sensors J.*, vol. 16, no. 12, pp. 4786–4792, Jun. 2016, doi: [10.1109/JSEN.2016.2554885](https://doi.org/10.1109/JSEN.2016.2554885).
- [7] K. Hedegaard, H. Ravn, N. Juul, and P. Meibom, "Effects of electric vehicles on power systems in northern Europe," *Energy*, vol. 48, no. 1, pp. 356–368, Dec. 2012, doi: [10.1016/j.energy.2012.06.012](https://doi.org/10.1016/j.energy.2012.06.012).
- [8] M. Moness and A. M. Moustafa, "A survey of cyber-physical advances and challenges of wind energy conversion systems: Prospects for Internet of energy," *IEEE Internet Things J.*, vol. 3, no. 2, pp. 134–145, Apr. 2016, doi: [10.1109/jiot.2015.2478381](https://doi.org/10.1109/jiot.2015.2478381).
- [9] I. L. Sauer, H. Tatizawa, F. A. Salotti, and S. S. Mercedes, "A comparative assessment of Brazilian electric motors performance with minimum efficiency standards," *Renew. Sustain. Energy Rev.*, vol. 41, p. 308–318, Jan. 2015, doi: [10.1016/j.rser.2014.08.053](https://doi.org/10.1016/j.rser.2014.08.053).
- [10] *IEEE Recommended Practice for The Design of Reliable Industrial and Commercial Power Systems*, Standard 493-1997, 1997.
- [11] A. Glowacz and Z. Glowacz, "Diagnosis of the three-phase induction motor using thermal imaging," *Infr. Phys. Technol.*, vol. 81, pp. 7–16, Mar. 2017, doi: [10.1016/j.infrared.2016.12.003](https://doi.org/10.1016/j.infrared.2016.12.003).
- [12] F. Dalvand, A. Kalantar, H. Bevrani, and S. Shokoohi, "Time-domain bearing condition monitoring in induction motors using instantaneous frequency of motor voltage," in *Proc. Smart Grid Conf.*, Jul. 2015, pp. 1–12, doi: [10.1109/SGC.2014.7150708](https://doi.org/10.1109/SGC.2014.7150708).
- [13] A. Giantomassi, F. Ferracuti, S. Iarlori, G. Ippoliti, and S. Longhi, "Electric motor fault detection and diagnosis by kernel density estimation and Kullback–Leibler divergence based on stator current measurements," *IEEE Trans. Ind. Electron.*, vol. 62, no. 3, pp. 1770–1780, Mar. 2015, doi: [10.1109/TIE.2014.2370936](https://doi.org/10.1109/TIE.2014.2370936).
- [14] Q. Han, Z. Ding, X. Xu, T. Wang, and F. Chu, "Stator current model for detecting rolling bearing faults in induction motors using magnetic equivalent circuits," *Mech. Syst. Signal Process.*, vol. 131, p. 554–575, Jun. 2019, doi: [10.1016/j.ymssp.2019.06.010](https://doi.org/10.1016/j.ymssp.2019.06.010).
- [15] A. C. Binoj Kumar, B. Saritha, and G. Narayanan, "Experimental comparison of conventional and bus-clamping PWM methods based on electrical and acoustic noise spectra of induction motor drives," *IEEE Trans. Ind. Appl.*, vol. 52, no. 5, pp. 4061–4073, Sep. 2016, doi: [10.1109/TIA.2016.2584578](https://doi.org/10.1109/TIA.2016.2584578).
- [16] K. M. Sousa, I. B. da Costa, E. S. Maciel, J. E. Rocha, C. Martelli, and J. C. da Silva, "Broken bar fault detection in induction motor by using optical fiber strain sensors," *IEEE Sensors J.*, vol. 17, no. 3, pp. 3369–3376, Jun. 2017.
- [17] A. Mohammed and S. Djurovic, "Stator winding internal thermal monitoring and analysis using *in situ* FBG sensing technology," *IEEE Trans. Energy Convers.*, vol. 33, no. 3, pp. 1508–1518, Sep. 2018, doi: [10.1109/TEC.2018.2826229](https://doi.org/10.1109/TEC.2018.2826229).
- [18] A. Mohammed, J. I. Melecio, and S. Djurovic, "Stator winding fault thermal signature monitoring and analysis by *in situ* FBG sensors," *IEEE Trans. Ind. Electron.*, vol. 66, no. 10, pp. 8082–8092, Oct. 2019, doi: [10.1109/TIE.2018.2883260](https://doi.org/10.1109/TIE.2018.2883260).
- [19] M. Fabian, D. Hind, C. Gerada, T. Sun, and K. T. V. Grattan, "Multi-parameter monitoring of electrical machines using integrated fibre Bragg gratings," *2017 25th Opt. Fiber Sensors Conf. (OFS)*, Jeju, South Korea, 2017, pp. 1–4, doi: [10.1117/12.2264928](https://doi.org/10.1117/12.2264928).
- [20] R. Ajith, A. Tewari, D. Gupta, and S. Tallur, "Low-cost vibration sensor for condition-based monitoring manufactured from polyurethane foam," *IEEE Sensors Lett.*, vol. 1, no. 6, Dec. 2017, Art no. 6001504.
- [21] J. R. Galvão, C. R. Zamarreño, C. Martelli, J. C. D. Silva, F. J. Arregui, and I. R. Matías, "Smart carbon fiber transibial prosthesis based on embedded fiber Bragg gratings," *IEEE Sensors J.*, vol. 18, no. 4, pp. 1520–1527, Feb. 2018.
- [22] A. Leal-Junior, A. Theodosiou, C. Marques, M. J. Pontes, K. Kalli, and A. Frizera, "Compensation method for temperature cross-sensitivity in transverse force applications with FBG sensors in POFs," *J. Lightw. Technol.*, vol. 36, no. 17, pp. 3660–3665, Jun. 28, 2018, doi: [10.1109/jlt.2018.2848704](https://doi.org/10.1109/jlt.2018.2848704).
- [23] C. A. F. Marques *et al.*, "Fast and stable gratings inscription in POFs made of different materials with pulsed 248 nm KRF laser," *Opt. Express*, vol. 26, no. 2, pp. 2013–2022, 2018, doi: [10.1364/OE.26.002013](https://doi.org/10.1364/OE.26.002013).
- [24] G. Luyckx, E. Voet, W. De Waele, and J. Degrieck, "Multi-axial strain transfer from laminated CFRP composites to embedded Bragg sensor: I. parametric study," *Smart Mater. Struct.*, vol. 19, no. 10, Oct. 2010, Art. no. 105017.
- [25] W. R. Finley, B. J. Sauer, and M. Loutfi, "Motor vibration problems: How to diagnose and correct vibration errors," *IEEE Ind. Appl. Mag.*, vol. 21, no. 6, pp. 14–28, Nov. 2015, doi: [10.1109/MIAS.2014.2345811](https://doi.org/10.1109/MIAS.2014.2345811).
- [26] P. V. J. Rodríguez, A. Belahcen, A. Arkkio, A. Laiho, and A. and J. Antonino-Daviu, "Air-gap force distribution and vibration pattern of Induction motors under dynamic eccentricity," *Elect. Eng.*, vol. 90, no. 3, p. 209–218, May 2007.
- [27] N. Tandon and A. Choudhury, "A review of vibration and acoustic measurement methods for the detection of defects in rolling element bearings," *Int. J. Tribol.*, vol. 32, no. 8, pp. 469–480, Aug. 1999.
- [28] N. Tandon, G.S. Yadava, and K. M. Ramakrishna, "A comparison of some condition monitoring techniques for the detection of defect in induction motor ball bearings," *Mech. Syst. Signal Process.*, vol. 21, no. 1, pp. 244–256, Jan. 2007, doi: [10.1016/j.ymssp.2005.08.005](https://doi.org/10.1016/j.ymssp.2005.08.005).
- [29] A. Prudhom, J. Antonino-Daviu, H. Razik, and V. Climente-Alarcon, "Time-frequency vibration analysis for the detection of motor damages caused by bearing currents," *Mech. Syst. Signal Process.*, vol. 84, pp. 747–762, Feb. 2017, doi: [10.1016/j.ymssp.2015.12.008](https://doi.org/10.1016/j.ymssp.2015.12.008).
- [30] Y.-J. Rao, "In-fibre Bragg grating sensors," *Meas. Sci. Technol.* vol. 8, no. 4, p. 355, 1997.
- [31] K. Hill and G. Meltz, "Fiber Bragg grating technology fundamentals and overview," *J. Lightw. Technol.*, vol. 15, no. 8, p. 1263–1276, Aug. 1997.
- [32] C. Broadway, R. Min, A. Leal-Junior, C. Marques, and C. Caucheteur, "Towards commercial polymer fiber Bragg grating sensors: Review and applications," *J. Lightw. Technol.*, vol. 37, no. 1, pp. 2605–2615, Jan. 2019.
- [33] K. D. M. Sousa, A. A. Hafner, H. J. Kalinowski, and J. C. C. da Silva, "Determination of temperature dynamics and mechanical and stator losses relationships in a three-phase induction motor using fiber Bragg grating sensors," *IEEE Sensors J.*, vol. 12, no. 10, pp. 3054–3061, Oct. 2012.
- [34] M. M. Werneck, R. Allil, B. Ribeiro, and F. de Nazaá, "A guide to fiber Bragg grating sensors," *Current Trends in Short- and Long-Period Fibre Gratings*. Rijeka, Croatia: InTech, 2013, pp. 1–24, doi: [10.5772/54682](https://doi.org/10.5772/54682).
- [35] L. C. Pardini and A. Gonáalves, "Processamento de compósitos termoestruturais de carbono reforçado com fibras de carbono," *J. Aerosp. Technol. Manage.*, vol. 1, no. 2, pp. 231–241, 2009, doi: [10.5028/jatm.2009.0102231241](https://doi.org/10.5028/jatm.2009.0102231241).
- [36] C. Dong, K. Li, Y. Jiang, D. Arola, and D. Zhang, "Evaluation of thermal expansion coefficient of carbon fiber reinforced composites using electronic speckle interferometry," *Opt. Express*, vol. 26, pp. 531–543, 2018, doi: [10.1364/OE.26.000531](https://doi.org/10.1364/OE.26.000531).
- [37] G. G. Kuhn, K. de Moraes Sousa, and J. C. C. da Silva, "Dynamic strain analysis of transformer iron core with fiber Bragg gratings," in *Advanced Photonics* (BGPP, IPR, NP, NOMA, Sensors, Networks, SPPCom, SOF). Washington, DC, USA: OSA, 2018, pp. 1–2, Paper JTU2A.74, doi: [10.1364/BGPPM.2018.JTU2A.74](https://doi.org/10.1364/BGPPM.2018.JTU2A.74).
- [38] L. Liu, H. Zhang, Q. Zhao, Y. Liu, and F. Li, "Temperature-independent FBG pressure sensor with high sensitivity," *Opt. Fiber Technol.*, vol. 13, no. 1, pp. 78–80, Jan. 2007, doi: [10.1016/j.yofte.2006.09.001](https://doi.org/10.1016/j.yofte.2006.09.001).
- [39] GOES Strategic Business Unit—Bagdad Plant, "Grain-oriented electrical steel," Allegheny Technol. Incorporated, Pittsburgh, PA, USA, Tech. Rep., 2012, vol. 1, pp. 1–32.
- [40] *Motors and Generators*, document MG 1-2014, National Electrical Manufacturers Association (NEMA in the States), Arlington, VA, USA, 2014.

### **3 PAPER 02: SMART CFRP-OFBG FOR MONITORING FAULT DETECTION IN BEARING**

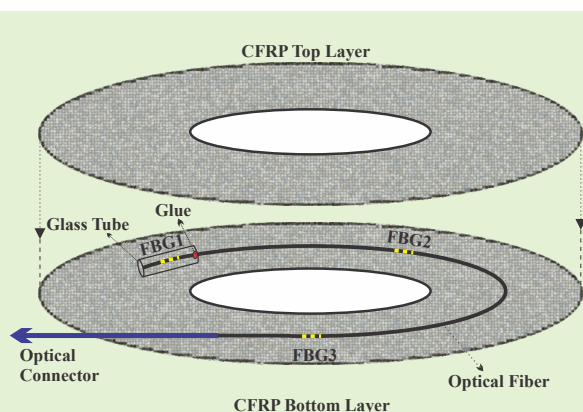
J. De Pelegrin, U. J. Dreyer, K. M. Sousa and J. C. C. Da Silva, "Smart Carbon-Fiber Reinforced Polymer Optical Fiber Bragg Grating for Monitoring Fault Detection in Bearing," in *IEEE Sensors Journal*, doi: 10.1109/JSEN.2022.3180305.

# Smart Carbon-Fiber Reinforced Polymer Optical Fiber Bragg Grating for Monitoring Fault Detection in Bearing

Jessé de Pelegrin, Uilian José Dreyer, Kleiton Morais Sousa, Jean Carlos Cardozo da Silva

**Abstract**— This article describes the development of a fiber Bragg grating (FBG) sensor encapsulated in carbon-fiber reinforced polymer to detect faults in rotating electrical machine bearings. The proposed sensor was based on the temperature and strain sensitivity of the FBG sensor and the robustness of carbon fiber as an encapsulation. The sensor was composed of three FBGs, one of which was packaged in a glass tube. The behavior characteristics of the developed sensor were evaluated in the calibration process. The experimental setup and measurement system were discussed and analyzed under dynamic conditions. The sensor was implemented in an induction motor operating at a controlled full load. The tests were performed with new and faulty bearings. The results, for the faulty bearing frequencies of 147.5, 296.6, and 439.0 Hz, were identified. These frequency components were generated by defects in the inner raceway. Comparing the amplitude spectrum between the signal of the new and faulty bearing, a variation of approximately 96% was found. The FBG reinforced sensor can identify bearing integrity in real-time and be a preventive maintenance tool for bearing monitoring.

**Index Terms**— Bearings faults, carbon fiber reinforced polymer, electrical machines, optical fiber Bragg grating.



## I. INTRODUCTION

**B**EARINGS are essential mechanical elements in transferring rotational movements. In rotating electrical machines, they are fundamental for the movement of the rotor. The bearings used in electrical machines are relatively inexpensive, but faults in these elements can cause the interruption of a production line, causing material and financial losses [1] [2]. Bearings are the leading cause of failures in electric machines, approximately 44% [3]. Because of the importance of induction motors (IMs) in the industrial environment, the prior diagnosis of bearing failures is essential to maintain the integrity of the machine and the operating system. Therefore, to have a reliable and safe system, it is necessary to monitor and diagnose the bearing faults continuously [4]. As important as diagnosing and characterizing the fault is to estimate its

This work was supported in part by the CAPES - Coordenação de Aperfeiçoamento de Pessoal de Nível Superior, in part by the CNPq - Conselho Nacional de Desenvolvimento Científico e Tecnológico, in part by the FINEP - Financiadora de Estudos e Projetos, in part by the Fundação Araucária, in part by the SETI - Secretaria da Ciência, Tecnologia e Ensino Superior, and in part by the Federal Institute Catarinense - IFC.

J.d. Pelegrin, U. J. Dreyer, K.M. Sousa, and J. C. Cardozo da Silva are with the Graduate Program in Electrical and Computer Engineering, Federal University of Technology-Paraná, Curitiba, Parana 80230-901, Brazil (e-mail:jesse.pelegrin@ifc.edu.br; uiliandreyer@utfpr.edu.br; kleitonsousa@utfpr.edu.br; Correspondence: jeancs@utfpr.edu.br).

severity [5].

In previous articles, several techniques and tools have been developed in the context of diagnosing bearing failures in their early stages [6]- [14]. In general, the methods use conventional sensors that can be installed on the machine frame, on the power cables, or through thermal imaging. Analyses can be performed by the grades of vibration [6] [7], current [8], magnetic field [9], and temperature [10]. The methods based on vibration signals are commonly used, as they measure and provide dynamic data that represent specific defects of the elements that make up the bearing [11]. Khadersab et al [12] experimentally investigated bearing failures using various vibration analysis techniques in the time, frequency, and time-frequency domains. Hoang et al. [13] established through vibration signals as input data an automatic fault diagnosis system with convolutional neural network and vibration image. Cui et al [14] have presented a dynamic analysis method for classifying fault severity and size estimation for ball bearings based on the vibration mechanism. The method consists of numerical analysis in the nonlinear dynamic ball bearing model, which considers the geometric properties and deformation of the balls.

In order to identify bearing faults, data must be collected with the system in operation. In oil, mining, paper, or mills industries, IMs are usually in difficult to access places. In addition, the collected signals are mixed with ambient noise

[15]. To get around these problems, this article presents the development of a sensor based on optical fiber Bragg grating (FBG) integrated in carbon-fiber reinforced polymer (CFRP). Fiber Bragg grating sensors have peculiar characteristics, such as good sensitivity, immune to electromagnetic interference, remote-sensing capability, and multiplexing [16] - [18]. These features are favored in electrical machine applications. Research using FBG in electrical machines showed promising results [19] - [21]. However, these works used bare optical fiber; because of the optical fiber fragility, application, and repeatability, this technique could be limited to laboratory tests. An alternative is to encapsulate optical sensors in a way that does not compromise measurement sensitivity. In this regard, CFRP is viable because it is a material that can be manufactured in various formats adaptable to each application [22].

The encapsulation of FBG sensors in CFRP, in addition to offering mechanical protection, does not significantly interfere with temperature and strain measurements [23] - [26]. Recently, some studies used FBG sensor encapsulated in CFRP in electrical machine applications. Kuhn et al [27] used the embedded FBG sensors in CFRP for vibration and temperature measurement in power transformer iron core. Pelegrin et al [28] developed the optical fiber sensor encapsulated in CFRP to detect the fault in rotating electrical machines' stator. The contribution of the present work is the development of a robust sensor capable of withstanding mechanical stresses without losing the measurement sensitivity characteristic of FBGs sensors. This sensor can be adapted to different dimensions, satisfying all bearing sizes. The advantages of the sensor in relation to the one developed by Pelegrin et al [28] are the direct contact of the sensor with the measurand. Direct contact makes it possible to identify incipient faults and significantly reduce the influence of external noise. Another novelty is the temperature measurement without the influence of strain due to the glass tube package in one of the FBGs, in addition to allowing an easy installation of the sensor without altering the machine's integrity.

This article proposes an optical fiber sensor based on dynamic strain and temperature measurements in the bearings of rotating electrical machines. The article is organized as follows: Section II presents the rolling-bearing design. Section III presents the development of the FBG reinforced sensor. The thermal calibration of the FBG reinforced sensor is shown in Section IV. Section V presents the experimental setup with sensor installation details. Section VI presents the results and discussion of the measurements performed. Finally, Section VII presents the conclusions and future perspectives.

## II. ROLLING BEARING DESIGN

The studied IM has installed the SKF-6310 ball bearing on the shaft side. Figure 1 presents the dimensions of the bearing that are used to determine the frequencies produced by the elements: balls, outer race, inner race, and cage. Defects in these elements generate frequencies that can be measured by frequency analyzers estimating the integrity of the bearing [29].

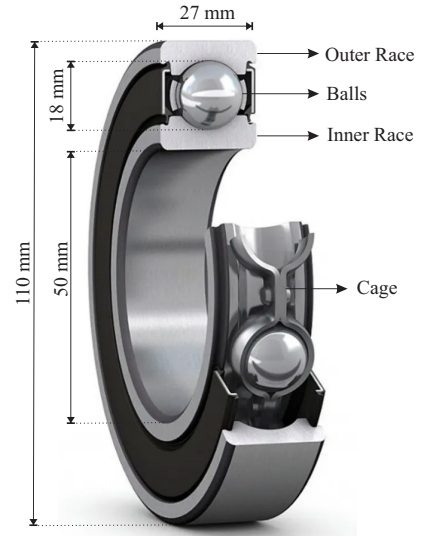


Fig. 1. Mechanical construction of the 6310 bearing.

The frequency analysis in IM bearings is detailed in the literature [1] - [4]. The bearings consist of an inner race, an external race, balls, and a cage. Defects caused by each bearing part generate a specific vibration frequency component. Each component can be calculated using Equations 1, 2, 3, and 4,

$$f_c = \frac{f_r}{2} \left[ 1 - \frac{d}{D} \cos(\alpha) \right], \quad (1)$$

$$f_b = f_r \left( \frac{d}{D} \right) \left[ 1 - \frac{d^2}{D^2} \cos^2(\alpha) \right], \quad (2)$$

$$f_{ir} = N_b \frac{f_r}{2} \left[ 1 + \frac{d}{D} \cos(\alpha) \right], \quad (3)$$

$$f_{or} = N_b \frac{f_r}{2} \left[ 1 - \frac{d}{D} \cos(\alpha) \right], \quad (4)$$

where  $f_c$  is the cage fault frequency;  $f_b$ , the ball fault frequency;  $f_{ir}$ , the inner raceway fault frequency;  $f_{or}$ , the outer raceway fault frequency;  $N_b$ , the number of balls;  $d$ , the diameter of the ball;  $D = ((d_i + d_o)/2)$ , the pitch diameter;  $\alpha$ , the contact angle; and  $f_r$ , the rotational frequency [30]. Table I shows the calculated frequencies of the 6310 bearing elements used for the 60 and 50 Hz power supply frequency.

TABLE I  
CALCULATED FREQUENCIES OF THE 6310 ELEMENTS THE BEARING TO 60 AND 50 HZ POWER SUPPLY FREQUENCY.

Dimensions	Frequency	60 Hz	50 Hz
Balls = 8	$f_r$	29.5 Hz	24.5 Hz
$d = 18$ mm	$f_c$	11.4 Hz	9.4 Hz
$D = 80$ mm	$f_{ir}$	144.1 Hz	120.1 Hz
$\alpha = 0$	$f_{or}$	91.2	76.0 Hz
	$f_b$	6.3 Hz	5.2 Hz

### III. DEVELOPMENT OF THE FBG REINFORCED SENSOR

Fiber Bragg gratings are the periodic refractive index modulation into the fiber core inscribed when exposed to a transversal UV light interference pattern of laser light [31] [32]. According to Bragg's law, a fraction of the incident power is reflected around the Bragg wavelength, which is given by:

$$\lambda_B = 2 \Lambda n_{eff}, \quad (5)$$

where  $n_{eff}$  is the effective refractive index of the fiber in the fundamental mode in which the FBG is imprinted and  $\Lambda$  is the period of the refractive index modulation of the FBG [34]. The FBG is sensitive to external disturbances, such as temperature and strain; these disturbances change the central wavelength, as it can be expressed as follows [32]:

$$\Delta\lambda_B = (1 - p_e)\Delta\epsilon + (\alpha + \xi)\Delta T, \quad (6)$$

where  $p_e$  is the photoelastic coefficient;  $\Delta\epsilon$  the strain change;  $\alpha$  is thermal expansion coefficient;  $\xi$ , the thermal-optic coefficient; and  $\Delta T$  is temperature change.

The CFRP has mechanical energy transfer characteristics appropriate for measuring temperature and vibration [25]. The CFRP has a low coefficient of thermal expansion, approximately  $1 \times 10^{-6} \text{ } ^\circ\text{C}^{-1}$  [26]. The elasticity coefficient depends on the number of layers of the CFRP; for two layers used in this work, it corresponds to 3.8 GPa [27].

The FBG reinforced sensor contains three FBGs multiplexed in one optical fiber and integrated in a carbon-fiber composite material. The FBGs were written using the phase mask technique onto a Ge-doped photosensitive fiber (fiber type: GF1, SMF Nufern) at the Photo Refractive Devices Unit at Universidade Tecnológica Federal do Paraná, with Bragg wavelengths of 1526, 1532, and 1554 nm. Each FBG is approximately 3 to 5 mm in length. The FBGs' main characteristics are the full width at half maximum of approximately 0.3 nm and reflectivity of 80%. Figure 2 presents the sensor developed for implementation in the ball bearing SKF-6310. FBG1 was encapsulated by a glass tube with an inner diameter of 1.0 mm and an outer diameter of 1.5 mm to eliminate the strain cross-sensitivity effect for temperature measurement. Cyanoacrylate glue was used at the ends of the glass tube. FBG2 and FBG3 were encapsulated directly in CFRP. The optical fiber was integrated between two layers of carbon-fiber composite of both bidirectional and unidirectional carbon-fiber fabric twill type ( $200 \text{ g/m}^2$ ) and epoxy resin (331), and thermosetting type with hardener (043), manufactured by Dow Chemical Company.

The first layer of the carbon fiber was impregnated with epoxy resin, hermetically sealed, and heated to perform the curing process. The optical fibers with the FBG sensors were positioned under the first layer and coated by the second layer. A vacuum pump was used to remove air particles, whereas the compound was cured at  $120 \text{ } ^\circ\text{C}$  for 8 hours. The dimensions of 108 and 52 mm in diameter, as well the thickness of approximately 3 mm, were defined because of the bearing and end shield measurements of the IM under study. The fiber was installed in the center of the CFRP (80 mm in diameter), and the FBGs were positioned at  $120^\circ$  of symmetry.

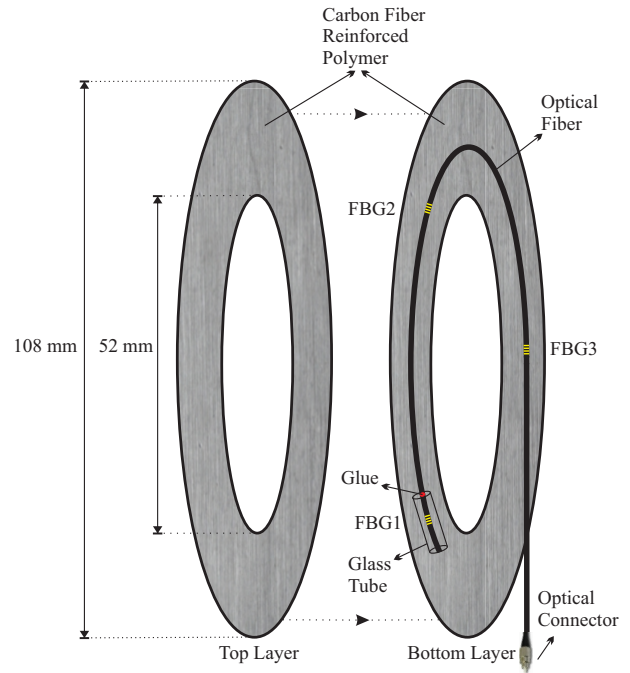


Fig. 2. Development of the FBG sensor encapsulated in CFRP.

Figure 3 shows the position of the sensor next to the bearing. This positioning allows identifying early bearing problems and as diminishing the influence of the external environment over the sensor. The end shield fixes the sensor to the bearing, without the need to use glue for example. The optical connector exits through the grease inlet as the bearing used is armored.

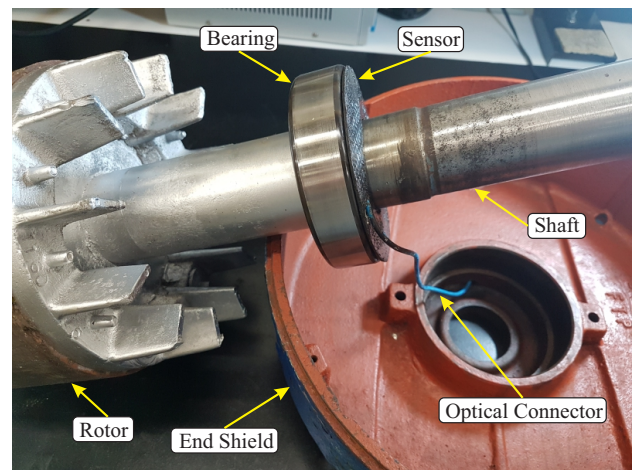


Fig. 3. Image of the FBG sensor positioned next to the bearing.

### IV. THERMAL CALIBRATION OF THE FBG REINFORCED SENSOR

The thermal calibration of the FBG reinforced sensor was carried out in two ways. First, the encapsulated sensor is calibrated using the thermal bath LAUDA model ECO RE415 submitting the sensor to different temperatures. The second

calibration process was performed with the encapsulated sensor already installed on the motor shaft, attached to the bearing, using the SOLAB thermal chamber model SL-100, according to Figure 4. Calibration procedures were the same for both situations. Data acquisition was performed using the SM130 optical interrogator, manufactured by Micron Optics, with a sample rate of 1 kHz. The sensor was subjected to thermal variation in the range of 20°C to 100°C at intervals of 10°C. This temperature was established because of the allowed operating range for the bearing model used [33]. Five repetitions were performed, and the average of the points obtained was linearly adjusted. A type K thermocouple probe sensor measured by a Fluke® 754 was inserted next to the sensor to confirm temperature stability. The sensor response was the same for the thermal bath and the chamber. Figure 4 shows the thermal chamber with the sensor in the measurement position. Despite being in contact with the bearing and end shield, there was no influence of the iron's thermal expansion for the analyzed temperatures as the maximum temperature was 100°C.

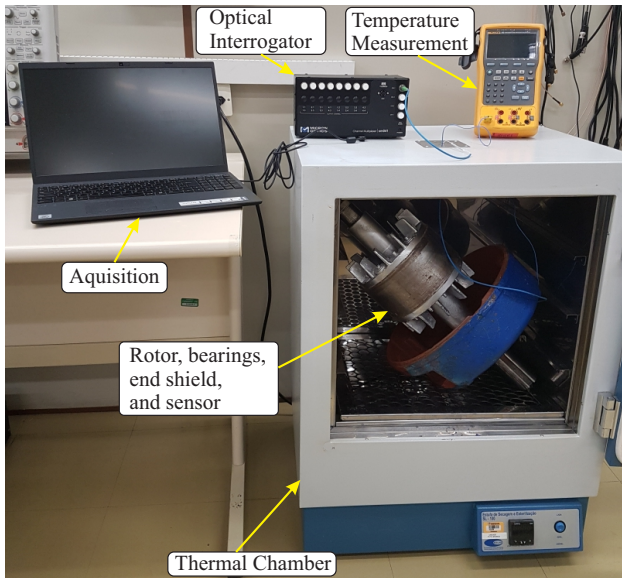


Fig. 4. Thermal calibration of the developed sensor.

Figure 5 presents the FBG1 calibration that is inside the glass tube. Because of the physical insulation of the tube, FBG1 does not demonstrate influences from the CFRP encapsulation. The calculated uncertainty for FBG1 at the measurement position was 1.0°C. The average temperature sensitivity determined by the calibration test was  $\approx 10.0 \text{ pm}/^\circ\text{C}$ , and correlation coefficient was 0.99976. Figure 6 presents the calibration of FBG2 and FBG3, which were encapsulated only in the CFRP. In this case, FBG2 and FBG3 were influenced by the CFRP encapsulation; the average temperature sensitivity determined by the calibration test was  $\approx 15.6$  and  $18.0 \text{ pm}/^\circ\text{C}$ , and generated a correlation coefficient of 0.99974 and 0.99854, respectively. The difference observed in FBG2 and FBG3 was due to the resin concentration in each FBG because the manufacturing process was manual. However, FBG1, being inside the glass tube, has a lower temperature sensitivity than

FBG2 and FBG3, influenced by CFRP.

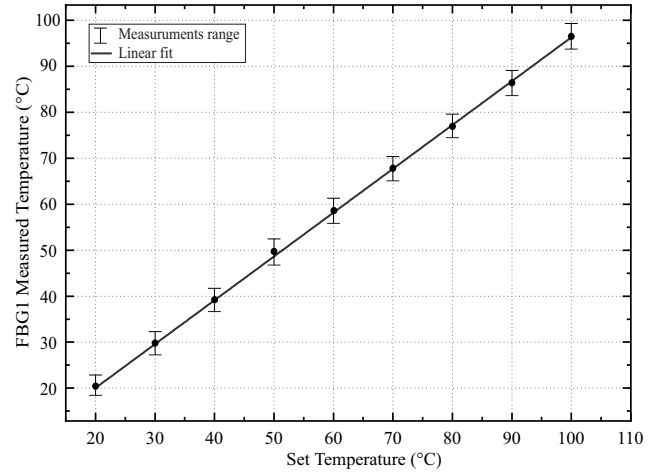


Fig. 5. Temperature calibration for FBG1.

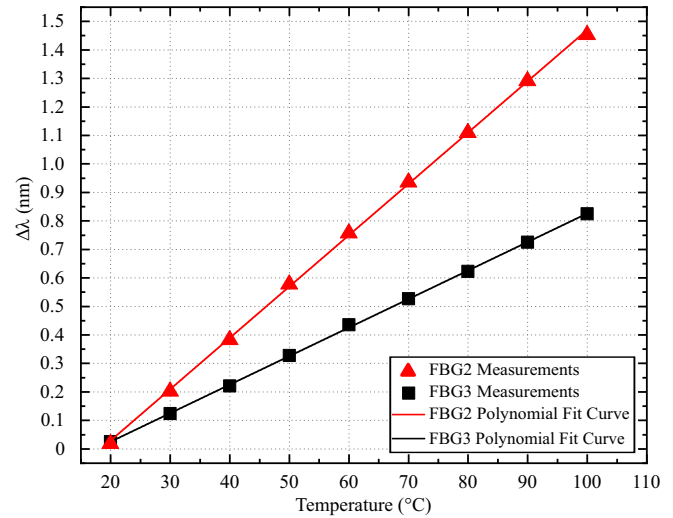


Fig. 6. Temperature calibration for FBG2 and FBG3.

## V. EXPERIMENTAL SETUP

The experimental tests were carried out on an IM, 4-poles, 15 HP, 1750 revolutions/min, and  $\Delta$ -connected and operated at 220 V. Figure 7 shows the test platform used to perform the tests. For loading purposes, the IM was coupled to an electric generator that was controlled to reach a desired operating point through resistive loads. Measurement of the bearing sensor was performed by the optical interrogator and analyzed with the commercial software catmanEasy – HBM®. The three-phase line current and voltage were measured by three Hall Effect Current Sensors LA 55-P (LEM®) and three Hall Effect Voltage Sensors LV 25-600/SP7 (LEM®), respectively. Current and voltage measurements were used to calculate the IM load.

The IM was started up at full load with direct-online starter. The frequency converter was not used in this test. The vibration tests were conducted with the bearing on the side of the shaft 6310, comparing new and faulty bearing. Figure 8

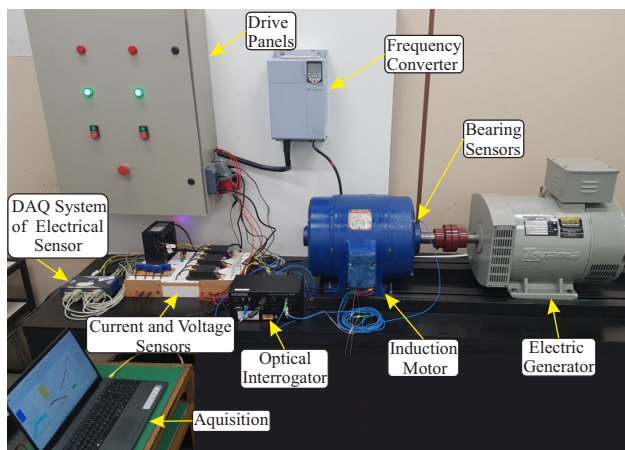


Fig. 7. Test platform for electrical machines.

shows the damaged bearing used in this article as the faulty bearing. The fault was generated by its use in an industrial plant over a period of 6 months.



Fig. 8. Faulty bearing removed from the IM after 6 months of operation showing crack in the inner raceway.

## VI. RESULTS AND DISCUSSION

### A. Temperature Analysis in FBG1

The IM was connected for 30 minutes at rated load condition. Figures 9 and 10 show the FBG1 measurements of the new and faulty bearings, respectively. The temperature variation measured during the operation was  $10.0^{\circ}\text{C}$  to new and  $15.0^{\circ}\text{C}$  to the faulty bearing. This variation of  $5.0^{\circ}\text{C}$  is due to the friction of the balls and the inner race of the bearing that has failures. When the motor started and shutdown, a wavelength quick transient was detected, which is related to the bearing friction and mechanical accommodation of the CFRP encapsulation. However, these transients do not influence the temperature measurement, as it has a slow response. The faulty bearing has wear in its elements; these problems generate losses that justify the increase in temperature because of time of use. It is important to emphasize that the allowable

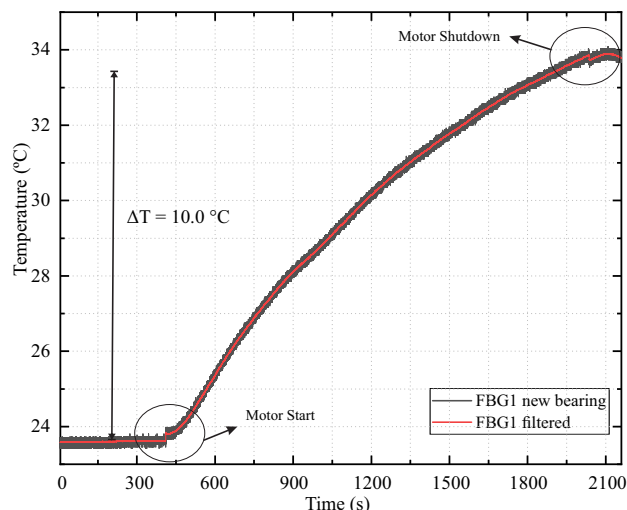


Fig. 9. Temperature measured by the new bearing with the motor operating at full load for 30 minutes.

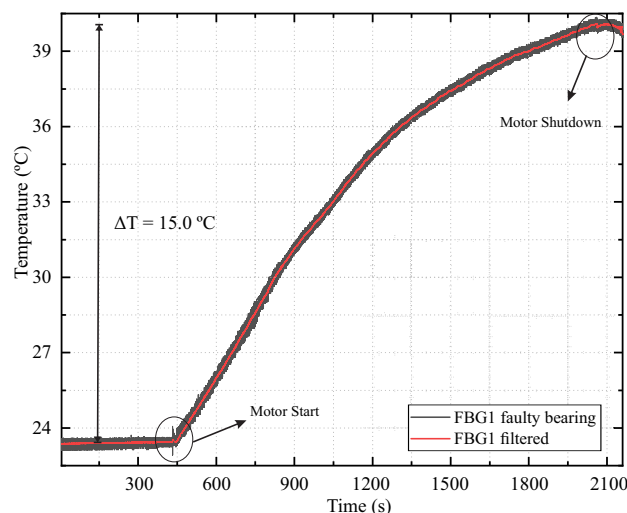


Fig. 10. Temperature measured by the faulty bearing with the motor operating at full load for 30 minutes.

operating temperature for deep groove ball bearings can be limited by the dimensional stability of the bearing rings and balls, cage, seals, and lubricant [33]. In addition, it is a region that does not have forced ventilation, contributing to the increase in temperature [19].

### B. Strain Analysis in FBG2 and FBG3

The frequency domain analysis is performed using the fast Fourier transform algorithm of MATLAB, applied to the acquired data at a 1.0 kHz sample rate. The obtained frequency spectrum provides the bearing integrity information when analyzing each frequency component related to the correspondent bearing elements. The FBG2 and FBG3 that integrate the FBG reinforced sensor are used to measure the bearing strain. According to this presented work the temperature events have temporal dynamics less than the dynamic strain events we are measuring to detect bearing failures.

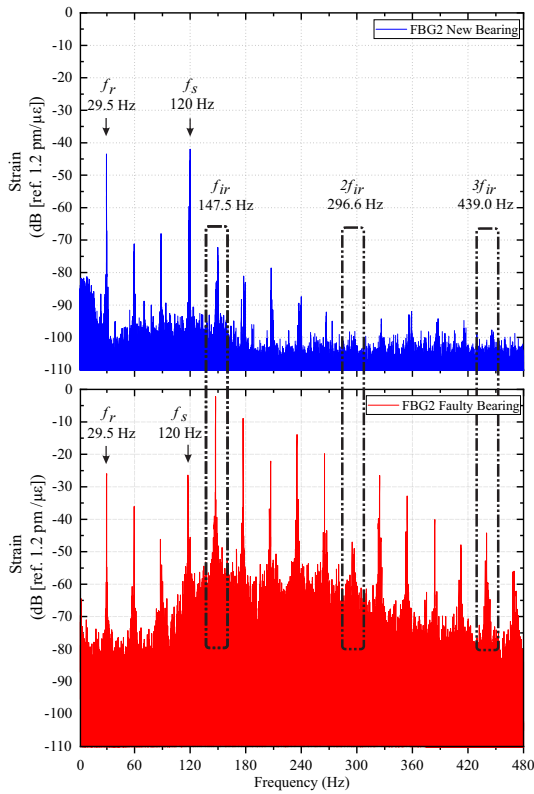


Fig. 11. Frequency response of strain measurement of the new and faulty bearing with FBG2, indicating frequencies based on the defects in the inner raceways, to the IM operating at 60 Hz.

Figures 11 and 12 show the strain measurement of the new (blue) and faulty (red) bearing of the FBG2 and FBG3 sensors, respectively. The observed frequency components were the mechanical frequencies ( $f_r$ ) at 29.5 Hz and harmonic components at 59.0, 88.5 Hz. The power supply frequency ( $f_s$ ) is also detected in 120 Hz. These components are under the influence of IM slip due to load and, for this reason, are slightly less than the power supply frequency [35]. When comparing the results between the new and the defective bearing, we highlight (dash dot), the frequency components in 147.5 Hz ( $f_{ir}$ ), 296.6 Hz ( $2f_{ir}$ ), and 439.0 Hz ( $3f_{ir}$ ).

Through the physical dimensions of the 6310 bearing, Table I determines the frequency of 144.1 Hz relating to the inner raceway. The frequency of the inner raceway had a difference of 3.4 Hz, which is related to the bearing wear. Because of the sensitivity of the FBG sensors, for the new bearing a certain level of amplitude is also identified for the frequencies related to the bearing. This amplitude increases as the bearing wore out. Fiber Bragg gratings were positioned in different positions, allowing to identify the failure at an early stage. The amplitude of the signal measured by FBG2 is greater than that of FBG3, meaning that FBG2 is closer to the defect; however, the same frequencies are identified by FBG3. In FBG2, the measured amplitude on the new bearing was -73 dB, and for the faulty bearing, -3 dB, an increase of approximately 24 times. Note that the amplitude of frequencies related to  $f_r$  and  $f_s$  increases for faulty bearing. This is due to

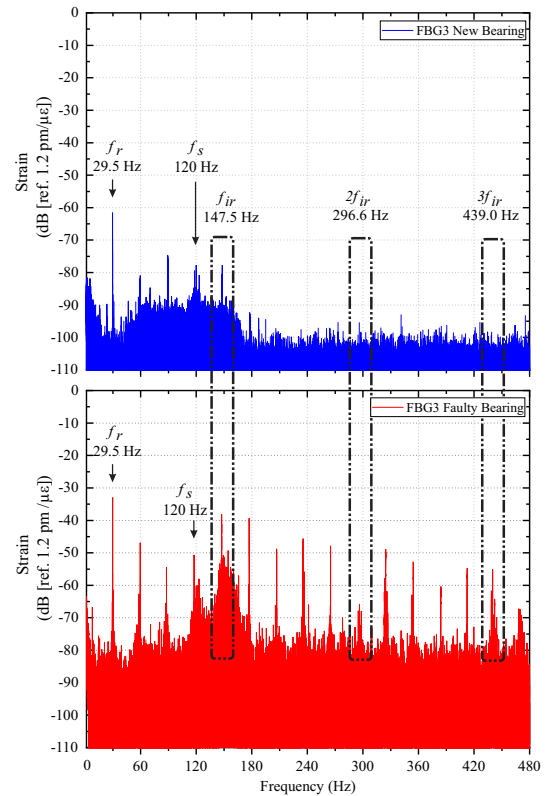


Fig. 12. Frequency response of strain measurement of the new and faulty bearing with FBG3, indicating frequencies based on the defects in the inner raceways, to the IM operating at 60 Hz.

the greater friction that bearing defects add to rotor movement.

In order to certify the frequencies measured by the FBG reinforced sensor, the tests were also performed with the IM operating at 50 Hz. Figures 13 and 14 show the strain measurement. As expected, the  $f_r$  measured was 24.7 Hz, and  $f_s$  100 Hz. Therefore, with the smaller rotor speed, the  $f_{ir}$  measured was 123.1 Hz, and harmonic components 246.6 ( $2f_{ir}$ ) and 369.6 Hz ( $3f_{ir}$ ). The frequencies measured based on the defects in the inner raceways coincide with the calculated values (Table I). The amplitude of the fundamental frequency measured at 50 Hz, was the same as that at 60 Hz, indicating the same degree of defect in the inner raceway.

The proposed sensor was subjected to repeatability tests to analyze the integrity due to friction and the related impact on bearing performance. The case analyzed was for the faulty bearing measured by the FBG3 to 60 and 50 Hz power supply frequency. Table II shows the results of three tests under the same conditions comparing ( $f_r$ ) e ( $f_{ir}$ ). The linear fittings present an  $R^2 > 0.99$ . The most significant uncertainties correspond to bearing failure on the inner race, possibly due to the gradual increase in wear. In terms of reproducibility, several tests were carried out over 3 months, with changes between new and faulty bearings. During this period, the proposed sensor did not present changes in its sensing capabilities, maintaining the sensitivity and integrity even in the face of bearing vibration. Therefore, the proposed sensor is reproducible.

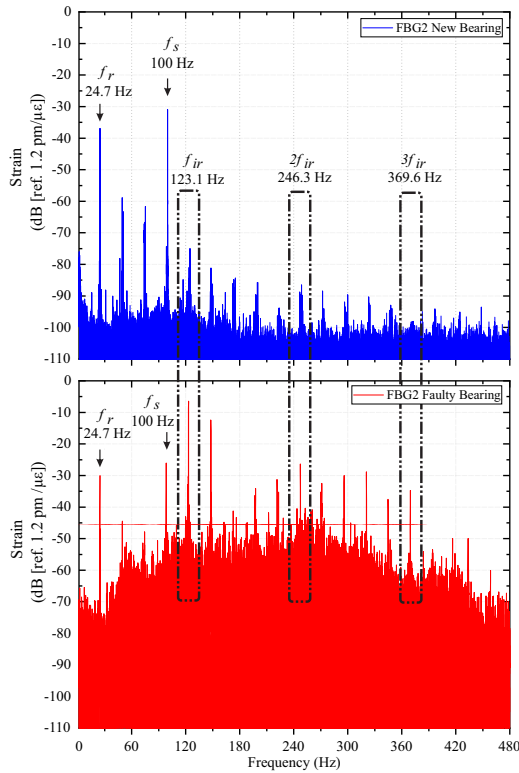


Fig. 13. Frequency response of strain measurement of the new and faulty bearing with FBG2, indicating frequencies based on the defects in the inner raceways, to the IM operating at 50 Hz.

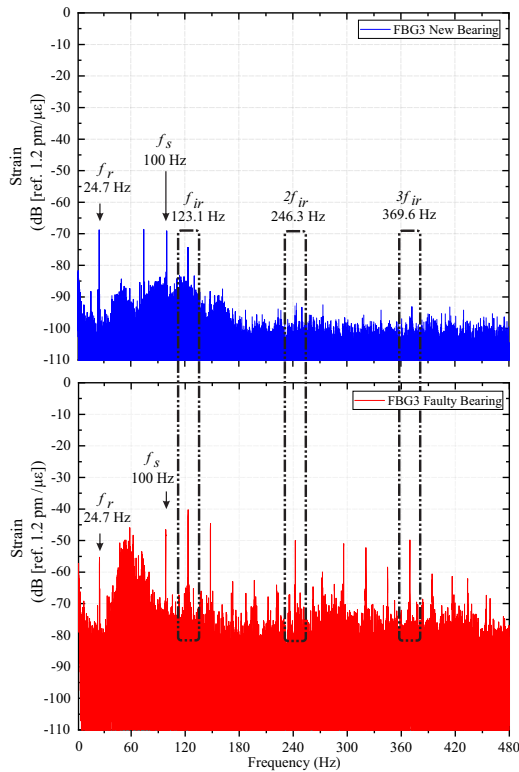


Fig. 14. Frequency response of strain measurement of the new and faulty bearing with FBG3, indicating frequencies based on the defects in the inner raceways, to the IM operating at 50 Hz.

TABLE II

FBG3 SENSOR UNCERTAINTY ANALYSIS FOR THREE TESTS PERFORMED AT 60 AND 50 Hz POWER SUPPLY FREQUENCY.

Frequency	60 Hz		50 Hz	
Variables	$f_r$ (Hz)	$f_{ir}$ (Hz)	$f_r$ (Hz)	$f_{ir}$ (Hz)
Calculated	29.5	144.1	24.5	120.1
Test I	29.5	147.5	24.7	123.1
Test II	29.4	146.8	24.6	122.5
Test III	29.5	147.1	24.5	121.8
Uncertainty	0.03	0.20	0.06	0.37

Although the FBG reinforced sensor was built manually, demonstrating limitations in relation to the positioning of the FBGs and possible curvatures, the results presented overcome such limitations. It is important to mention that the bearing defect was not produced manually, but caused by the time of use. Even so, the sensor was able to identify the faulty inner raceway. Comparing similar methods [21], which insert FGB sensor into a groove made in the bearing [36] [37], which fix the FBG sensor in the machine external region, the advantage of using the sensor presented in this article is the direct contact with the measuring, allowing the identification of vibrations at an early stage. In addition, to the practicality of installing the sensor without changing the bearing or machine structure. In this sense, the encapsulation with CFRP proved to be efficient to protect optical sensors and still allowed sensitivity for strain and temperature measurements of FBG sensors. Furthermore, the sensor can be built in any dimension, adaptable to different rotating electrical machines.

## VII. CONCLUSION

In this article, an FBG sensor encapsulated in CFRP to measure the temperature and strain of bearings of electrical machines was developed. The FBG reinforced sensor was based on three FBGs integrated into a carbon-fiber composite material. FBG1 was coated with capillary glass to diminish the dynamic strain influence and was used to measure temperature. FBG2 and FBG3 were encapsulated directly in the CFRP to measure strain. The sensor was subjected to two calibration processes, in a thermal bath and in situ operation, showing the same characteristics. The sensor was installed in an IM, and tests were performed for a new and faulty bearing. An increase of 5°C was observed between new and defective bearings at the same time and load conditions. The bearing strain measurements presented theoretically predicted frequencies, indicating faults in the inner raceways of the bearing. In the strain analysis, an increase of 96% was identified in the amplitude of faults in the inner raceways. The findings demonstrate an analysis of the mechanical and thermal integrity of the bearing during the IM operation, which, through constant reading, detects the gradual faulty of the bearing. The FBG reinforced sensor offers an effective solution to identify faulty bearings. As it is in direct contact with the bearing, the sensor allows detecting failures in its initial stage. The sensor opens the way for further research in different operating situations of electrical machines, for example, bearing service life, eccentricity, analysis of different IM starts and loads, unbalanced voltage, and broken bars.

## VIII. ACKNOWLEDGMENTS

The authors acknowledge CAPES (Coordination of Superior Level Staff Improvement), CNPQ (National Council for Scientific and Technological Development), FINEP (Funding Authority for Studies and Projects), Araucária Foundation, and SETI (State Secretary of Science, Technology, and Higher Education of Paraná), and Multi-User Photonics Facility - UTFPR-CT, IFC (Federal Institute of Catarinense) This study was financed in part by the Coordenação de Aperfeiçoamento de Pessoal de Nível Superior - Brasil (CAPES) - Finance Code 001.

## REFERENCES

- [1] S.E. Pandarakone, Y. Mizuno, H. Nakamura, Distinct fault analysis of induction motor bearing using frequency spectrum determination and support vector machine, *IEEE Trans. Ind. Appl.*, 53 (3) (2017), pp. 3049-3056.
- [2] J. Lee, F. Wu, W. Zhao, M. Ghaffari, L. Liao, D. Siegel, Prognostics and health management design for rotary machinery systems—reviews, methodology and applications, *Mech. Syst. Signal Process.*, 42 (2014), pp. 314-334.
- [3] G. Georgoulas, T. Loutas, C. D. Stylios, V. Kostopoulos, Bearing fault detection based on hybrid ensemble detector and empirical mode decomposition, *Mechanical Systems and Signal Processing*, vol. 41, issues 1–2, 2013, pp. 510-525, doi:10.1016/j.ymssp.2013.02.020.
- [4] A. Glowacz, W. Glowacz, Z. Glowacz, Early fault diagnosis of bearing and stator faults of the single-phase induction motor using acoustic signals, *Measurement*, 113 (2018), pp. 1-9.
- [5] F.B. Zhang, J.F. Huang, F.L. Chu, Lingli Cui, Mechanism and method for outer raceway defect localization of ball bearings, *IEEE ACCESS*, vol. 8, pp. 4351-4360, Apr, 2020.
- [6] F. Deng, Y. Qiang, Y. Liu, S. Yang, R. Hao, Adaptive parametric dictionary design of sparse representation based on fault impulse matching for rotating machinery weak fault detection, *Meas. Sci. Technol.*, 31 (6) (2020), p. 065101.
- [7] Q. Han, Z. Jiang, X. Xu, Z. Ding, F. Chu, Self-powered fault diagnosis of rolling bearings based on triboelectric effect, *Mechanical Systems and Signal Processing*, vol. 166, 2022, 108382, ISSN 0888-3270, <https://doi.org/10.1016/j.ymssp.2021.108382>.
- [8] F. Marouane, S. Abdenour, B. E. Mohamed El, Gear faults diagnosis based on the geometric indicators of electrical signals in three-phase induction motors, *Mechanism and Machine Theory*, vol. 138, pp 1-15, 2019, 10.1016/j.mechmachtheory.2019.03.030.
- [9] L. Frosini, C. Harlişca, L. Szabó, Induction machine bearing fault detection by means of statistical, processing of the stray flux measurement *IEEE Trans. Ind. Electron.*, 62 (3) (2015), pp. 1846-1854.
- [10] Z. Huo, Y. Zhang, R. Sath and L. Shu, Self-adaptive fault diagnosis of roller bearings using infrared thermal images, *IECON 2017 - 43rd Annual Conference of the IEEE Industrial Electronics Society*, 2017, pp. 6113-6118, doi: 10.1109/IECON.2017.8217062.
- [11] P.P. Khariche, S.V. Kshirsagar, Review of fault detection in rolling element bearing, *International Journal of Innovative Research in Advanced Engineering*, 1 (5) (2014), pp. 169-174.
- [12] A. Khadersab, S. Shivakumar, Vibration Analysis Techniques for Rotating Machinery and its effect on Bearing Faults, *Proceed Manufacturing*, vol. 20, 2018, pg 247-252, ISSN 2351-9789, doi: 10.1016/j.promfg.2018.02.036.
- [13] D. T. Hoang, H. J. Kang, Rolling element bearing fault diagnosis using convolutional neural network and vibration image, *Cognitive Systems Research*, vol. 53, 2019, pg 42-50, ISSN 1389-0417, doi: 10.1016/j.cogsys.2018.03.002.
- [14] L. Cui, Z. Jin, J. Huang e H. Wang, Fault Severity Classification and Size Estimation for Ball Bearings Based on Vibration Mechanism, *em IEEE Access*, vol. 7, pp. 56107-56116, 2019, doi: 10.1109 / ACCESS.2019.2911323.
- [15] H. Liu, J. Zhou, Y. Zheng, W. Jiang, Y. Zhang, Fault diagnosis of rolling bearings with recurrent neural network-based autoencoders, *ISA Transactions*, vol.77, 2018, pg 167-178, doi:10.1016/j.isatra.2018.04.005.
- [16] K. Dey, S Roy, P. Kishore, M. S. Shankara, R. K. Buddu, R. Ranjanc, Analysis and performance of edge filtering interrogation scheme for FBG sensor using SMS fiber and OTDR, in *Results in Optics*, vol. 2, jan. 2021. doi: 10.1016/j.rio.2020.100039.
- [17] K. Dey, R. Ranjanc, S. Roy, Performance of Etched Silica FBG for Simultaneous Strain Temperature Measurement Silicon, in *Springer*, jul. 2021. doi: 10.1007/s12633-021-01225-x.
- [18] D. Su, X. Qiao, F. Chen and W. Bao, "Compact Dual Fiber Bragg Gratings for Simultaneous Strain and High-Temperature Measurement," in *IEEE Sensors Journal*, vol. 19, no. 14, pp. 5660-5664, 15 July, 2019, doi: 10.1109/JSEN.2019.2906341.
- [19] K. M. Sousa, A. A. Hafner, H. J. Kalinowski, and J. C. C. da Silva, Determination of Temperature Dynamics and Mechanical and Stator Losses Relationships in a Three-Phase Induction Motor Using Fiber Bragg Grating Sensors, *IEEE Sensors Journal*, vol. 12, no. 10, Oct. 2012.
- [20] U. J. Dreyer et al., Quasi-Distributed Optical Fiber Transducer for Simultaneous Temperature and Vibration Sensing in High-Power Generators, in *IEEE Sensors Journal*, vol. 18, no. 4, pp. 1547-1554, 15 Feb.15, 2018, doi: 10.1109/JSEN.2017.2787681.
- [21] A. Mohammed and S. Djurović, Electric Machine Bearing Health Monitoring and Ball Fault Detection by Simultaneous Thermo-Mechanical Fibre Optic Sensing, in *IEEE Transactions on Energy Conversion*, vol. 36, no. 1, pp. 71-80, March 2021, doi: 10.1109/TEC.2020.3003793.
- [22] X. Geng, M. Jiang, L. Gao, Q. Wang, Y. Jia, Q. Sui, L. Jia, D. Li, Sensing characteristics of FBG sensor embedded in CFRP laminate, in *Measurement*, 98, 199–204. doi:10.1016/j.measurement.2016.12.003.
- [23] P. Zhu, J. Wu, M. Huang, Y. Wang, P. Liu, and M. A. Soto, Reducing Residual Strain in Fiber Bragg Grating Temperature Sensors Embedded in Carbon Fiber Reinforced Polymers, *J. Lightwave Technol.* 37, 4650-4656, 2019.
- [24] F. Li, Y. Du, X. Sun, W. Zhao, Sensing performance assessment of twisted CFRP with embedded fiber Bragg grating sensors subjected to monotonic and fatigue loading, *Sensors and Actuators A: Physical*, vol. 271, 2018, pg 153-161, ISSN 0924-4247, doi:10.1016/j.sna.2018.01.027.
- [25] J. R. Galvao, C. R. Zamarrero, C. Martelli, J.C.C Silva F.J. Arregui I.R. Matías, Smart carbon fiber transibial prosthesis based on embedded fiber bragg gratings, *IEEE Sensors Journal*, IEEE, v. 18, n. 4, p. 1520-1527, 2018.
- [26] C. Dong, K. Li, Y. Jiang, D. Arola, D. Zhang. Evaluation of thermal expansion coefficient of carbon fiber reinforced composites using electronic speckle interferometry, *Optics Express*, vol. 26, issue 1, pp. 531-543 jan. 2018. doi: 10.1364/OE.26.000531.
- [27] G. G. Kuhn, K. M. Sousa, C. Martelli, C. A. Bavastrri and J. C. C. d. Silva, Embedded FBG Sensors in Carbon Fiber for Vibration and Temperature Measurement in Power Transformer Iron Core, in *IEEE Sensors Journal*, vol. 20, no. 22, pp. 13403-13410, 15 Nov.15, 2020, doi: 10.1109/JSEN.2020.3005884.
- [28] J. de Pelegrin, U. J. Dreyer, C. Martelli and J. C. C. da Silva, Optical Fiber Sensor Encapsulated in Carbon Fiber Reinforced Polymer for Fault Detection in Rotating Electrical Machines, *IEEE Sensors Journal*, vol. 20, no. 19, pp. 11364-11371, 1 Oct.1, 2020, doi: 10.1109/JSEN.2020.2997597.
- [29] C. Xiao, H. Tang, Y. Ren, J. Xiang, A. Kumar, A fault frequency bands location method based on improved fast spectral correlation to extract fault features in axial piston pump bearings, *Measurement*, vol. 171, 2021, ISSN 0263-2241, doi:10.1016/j.measurement.2020.108734.
- [30] A. Prudhom, J. Antonino-Daviu, H. Razik, and V. Climente-Alarcon, Time-frequency vibration analysis for the detection of motor damages caused by bearing currents, *Elsevier*, pp. 747-762, Dec. 2015, doi:10.1016/j.ymssp.2015.12.008.
- [31] Rao, Yun-Jiang, In-fibre Bragg grating sensors, *Measurement science and technology* 8.4 (1997): 355.
- [32] K. Hill and G. Meltz, Fiber Bragg grating technology fundamentals and overview, *J. Lightw. Technol.*, vol. 15, no. 8, pp. 1263–1276, Aug. 1997.
- [33] SKF, SKF Maintenance and Lubrication Products, Jul. 2019.
- [34] A. D. Kersey et al., Fiber grating sensors, in *Journal of Lightwave Technology*, vol. 15, no. 8, pp. 1442-1463, Aug. 1997, doi: 10.1109/50.618377.
- [35] Sousa K. M., Dreyer U. J., Martelli C. and Silva J. C., Vibration measurement of Induction Motor under dynamic eccentricity using optical fiber Bragg grating sensors, 2015 SBMO/IEEE MTT-S International Microwave and Optoelectronics Conference (IMOC), 2015, pp. 1-5, doi: 10.1109/IMOC.2015.7369059.
- [36] H. Alian, et al., Bearing fault detection and fault size estimation using fiber-optic sensors, *Mechanical Systems and Signal Processing*, Vol. 120, 2019, Pg 392-407, doi:10.1016/j.ymssp.2018.10.035.
- [37] W. Peng, et al., Fault diagnosis of the rolling bearing with optical fiber Bragg grating vibration sensor vol.10155, *International Symposium on Optoelectronic Technology and Application 2016* doi: 10.1117/12.2247039.

#### **4 PAPER 03: RAMAN DISTRIBUTED TEMPERATURE SENSING FOR END WINDING OF HIGH-POWER GENERATOR**

Pelegrin, J.d., Bazzo, J.P., Dreyer, U.J., Martelli, C., Pipa, D.R., Silva, E.V.d. and Cardozo da Silva, J.C. (2020), "Raman distributed temperature sensing for end winding of high-power generator". IET Optoelectron., 14: 343-349. <https://doi.org/10.1049/iet-opt.2020.0037>

# Raman distributed temperature sensing for end winding of high-power generator

ISSN 1751-8768  
Received on 3rd March 2020  
Revised 8th April 2020  
Accepted on 13th May 2020  
E-First on 12th August 2020  
doi: 10.1049/iet-opt.2020.0037  
www.ietdl.org

Jessé de Pelegrin<sup>1</sup>, João Paulo Bazzo<sup>1</sup>, Uilian José Dreyer<sup>1</sup>, Cicero Martelli<sup>1</sup>, Daniel Rodrigues Pipa<sup>1</sup>, Erlon Vagner da Silva<sup>2</sup>, Jean Carlos Cardozo da Silva<sup>1</sup> ✉

<sup>1</sup>Federal University of Technology – Paraná (UTFPR), Curitiba, PR 80230-901, Brazil

<sup>2</sup>Engie Brasil Energia S.A., Saudade do Iguaçu, PR 85568-000, Brazil

✉ E-mail: jeanccs@utfpr.edu.br

**Abstract:** The temperature on the busbars of electric generators in the end-winding region needs to be monitored continuously. High temperature is associated with curvatures, seams, and poor ventilation. However, this solution has limitations, such as the number of measurement points. This article presents a reconstruction algorithm to estimate high-resolution signals, from readings of a distributed temperature system for monitoring high-power generator bars. The purpose of this work is to measure the temperature in the end-winding region with optical sensors based on Raman distributed temperature sensing (RDTS). The ability of RDTS equipment to perform a measurement is limited by its spatial resolution of 1 m. The proposed algorithm reduces spatial resolution through signal processing without changing the equipment hardware. Through the experimental results, it was possible to perform accurate temperature measurements for lengths up to 15 cm using the sensor element. With this method, the final winding of a generator bar of a 355 MW hydroelectric plant was instrumented in the laboratory. The results show that it is possible to monitor the temperature over this region, which has a length of 45 cm. Therefore, the proposed method has the potential for the use of RDTS systems for temperature acquisition of small, medium, and large electrical machines.

## 1 Introduction

Electric generators have an operational limit due to the overheating of the stator windings. The end winding of the generator experiences greater heating because the magnetic flux is not axial to the core segments [1–4]. Low ventilation in this region results in lowering the machine efficiency and further wearing of the bar's isolation materials leading to a generator shutdown. [5]. Temperature monitoring in this region is essential to ensure smooth operation and performance of the machine. Usually, conventional sensors used in the temperature measurement are PT100 or resistance temperature detector (RTD). These devices are suitable for monitoring point temperatures during the standard operation. However, to obtain monitoring along the bar, it is necessary to install several reading units, resulting in numerous power and measurement cables. Additionally, they use electronic transducers that are sensitive to magnetic interference [6, 7]. Regarding the presented, optical fibre sensors have characteristics that can solve several problems.

The evolution of photonic equipment, reduction in optical system costs, reliability and increased demand in industrial applications are part of the problems solved by optical fibre sensors. The oil and gas industry began the adoption of distributed optical sensor (DTS) technology in the 1990s in pipeline monitoring and fire detection [8]. Subsequently, other areas started to use it as a system of power, energy transmission and conveyor belts, among others [9–13].

The advantages of using the distributed systems include the elimination of the need for multichannel data acquisition systems instead of traditional methods; and identifying each channel and the location of the sensors is unnecessary. This allows a reduction in the number of cables connected. Another advantage is the ability to multiplex data; and a single fibre capable of producing two sets of vital information (that is regarding temperature and fault location), while conventional technology retains the need to deploy thermocouples, thermistors or RTDs. Furthermore, the calibration time is much shorter when compared to conventional technology. With the distributed fibre technology it is possible to determine the fail location within a metres range [14]. With these advantages, the

industrial sector is replacing conventional sensors for distributed sensors.

The DTS is a system with great potential for applications in electrical machines. Advantages include the possibility of using the fibre itself with a sensor element, immunity to electromagnetic interference, galvanic isolation and electrical passivity. The measurement was carried out based on the scattering of the backscattering of light, using the principles of Rayleigh, Brillouin or Raman. Among these, the Raman scattering stands out as commercial equipment [15]. Unlike traditional sensors, which measure point temperatures, the Raman distributed temperature sensing (RDTS) system is capable of measuring the temperature along the whole optical fibre. The equipment is generally applied in large systems because commercial DTS can measure temperature in fibres longer than 30 km, with a detection accuracy of 0.1°C and a spatial resolution of 1 m [16].

To correctly measure the temperature, the spatial resolution ( $\delta_s$ ) is the minimum length required for the RDTS system. It is defined as the spatial distance between the 10 and 90% levels of the response to a temperature step. For situations where the temperature reading is measured at length less than the spatial resolution, the measured temperature will not correspond with the actual temperature. This limitation imposes reading errors in systems that require measurements of temperature in fibres of length <1 m [16].

Other methods also allow the reduction of spatial resolution, such as scattering Brillouin (which performs distributed temperature and strain measurements) [17] and scattering Rayleigh's (which presents proper spatial resolutions in 10 cm) [15]. Although both methods demonstrate significant results, the equipment that incorporates them is expensive, with their costs being ~75% higher than that of RDTS.

To improve the spatial resolution of RDTS without interfering with the hardware, algorithms can be developed and implemented in temperature monitoring systems [18, 19]. This technique was implemented in a hydroelectric generator, where the temperature readings were obtained at a spatial resolution of 15 cm. [20, 21]

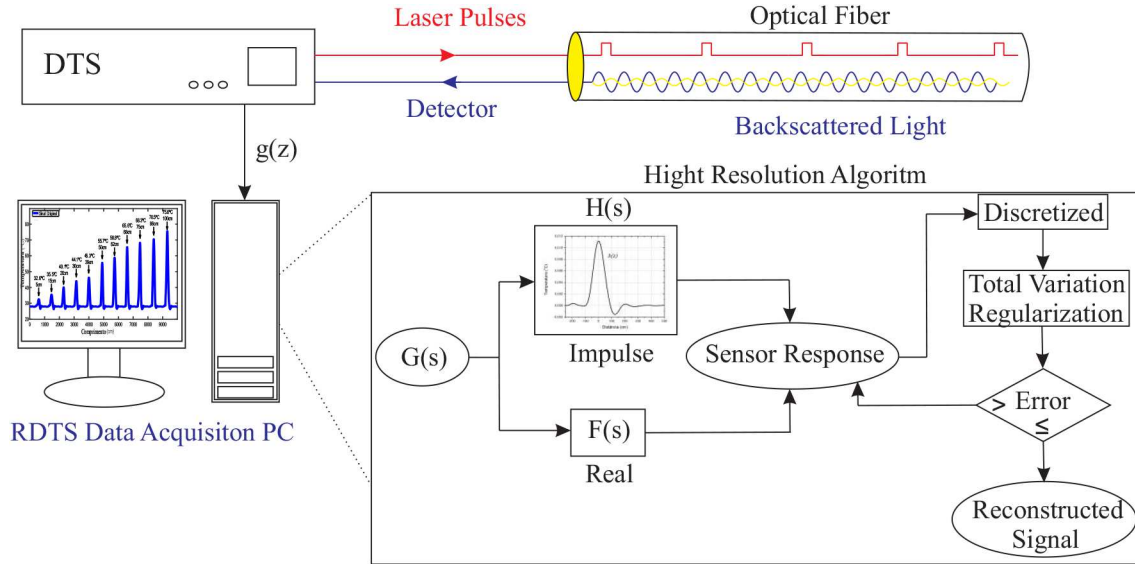


Fig. 1 Details of operation referring to high-resolution algorithm

In general, electrical machines need to be monitored, especially regarding their temperature [22]. High temperatures indicate possible failures of parts of the generator, such as the stator, rotor or bearings [23]. Generators often operate at their power limit constantly for hours, working at high temperatures that impair the insulation of the machine [24].

In this paper, a method is presented to improve the spatial resolution of equipment (RDTs) through a signal processing algorithm based on deconvolution by a *total variation* of temperature measurement in the end-winding of a high-power generator (355 MW). The reconstruction algorithm was tested and validated experimentally. The implementation of this proposed technique is performed on a segment of a bar that makes up the stator of a hydroelectric generator. This method can contribute to temperature measurements in regions of small, medium and large electrical machines.

## 2 Materials and methods

### 2.1 RDTs system model identification

The mathematical model of the RDTs system was built using techniques implemented for the identification of linear systems [25]. It was considered that the RDTs system is a linear time-invariant system, according (1), where  $f(z)$  is the real temperature profile,  $h(z)$  the impulse response of the RDTs system and  $g(z)$  is the signal convolution response. The Laplace transform was applied to obtain (2). The poles ( $\beta_i$ ) and zeros ( $\alpha_i$ ) of the function  $H(s)$  were estimated, according to (3) [18]:

$$g(z) = h(z) * f(z) \quad (1)$$

$$G(s) = H(s)F(s) \quad (2)$$

$$H(s) = \frac{b_0s^m + b_1s^{m-1} + \dots + b_m}{s^n + a_1s^{n-1} + \dots + a_n} = \frac{\prod_{i=1}^m (s - \alpha_i)}{\prod_{i=1}^n (s - \beta_i)} \quad (3)$$

We consider a discretised version of the observation model in (1). For better visualisation, it is rewritten in matrix notation, according to (4). The data obtained by the RDTs system are represented by  $\mathbf{g}$ , the impulse response is the matrix  $\mathbf{H}$ , the temperature profile  $\mathbf{f}$  and the vector  $\mathbf{n}$  represents all noise sources that are inherent to the measurement system, which can be originated by the optoelectronic circuit noise, connector coupling and environment where the equipment was installed. For approximation purposes, such noise sources are well represented by the white Gaussian noise:

$$\mathbf{g} = \mathbf{H}\mathbf{f} + \mathbf{n} \quad (4)$$

$$\begin{bmatrix} g(z_0) \\ \vdots \\ g(z_k) \end{bmatrix} = \begin{bmatrix} h(z_0) & h(z_{0-1}) & \dots & h(z_{0-k}) \\ \vdots & h(z_0) & \dots & \vdots \\ \vdots & \vdots & \dots & \vdots \\ h(z_k) & h(z_{k-1}) & \dots & h(z_0) \end{bmatrix} \begin{bmatrix} f(z_0) \\ \vdots \\ f(z_k) \end{bmatrix} + \begin{bmatrix} n(z_0) \\ \vdots \\ n(z_k) \end{bmatrix} \quad (5)$$

RDTs equipment has the characteristic of low-pass systems and impulse spreads. Thus, the solution discovered was the application of *total variation* that regulates the signal. Through (6), the reconstruction of images is acquired [18]:

$$\hat{\mathbf{f}} = \arg \min_f \|\mathbf{g} - \mathbf{H}\mathbf{f}\|_p^2 + \lambda \|\mathbf{D}\mathbf{f}\|_1 \quad (6)$$

The reconstructed signal  $\hat{\mathbf{f}}$  results from a balance between a data-fidelity term and a prior term based on finite differences. The balance is controlled by the parameter  $\lambda$ : higher values of  $\lambda$  yield to smoother reconstructed signals. Furthermore, one can control the assumed distribution of the residuals by changing  $0 < p \leq 2$ .

The high-resolution algorithm is illustrated in Fig. 1. The DTS detects the signal of the fibre optic sensor and generates a  $g(z)$  signal. Then, the temperature distribution is reconstructed by applying a deconvolution algorithm using the total variation regularisation in the signal  $g(z)$ . The regularisation parameter is determined using the L-curve method as the basis for the adjustment. This approach privileges temperature distributions that are piecewise constant while matching DTS readings. The implementation details in Matlab are shown in the Algorithm (see Fig. 2).

### 2.2 Experimental setup

**2.2.1 Design of validation plate:** The proposed algorithm enables the reading of distributed temperature sensors that can measure variations in structures with dimensions  $< 1$  m, reaching up to 15 cm. To validate this proposal, an experiment was set up, as shown in Fig. 3. An aluminium plate (1.40 m  $\times$  1.40 m), with a triangular cutout, was fixed on a wooden plate. Behind this aluminium plate, the electrical resistance was distributed following the same triangular shape. This distribution allows temperature measurements with resolutions ranging from 5 to 140 cm.

At the top of the plate, an optical fibre (50/125  $\mu\text{m}$  multimode gradual indexes) is glued to the aluminium plate with an insulating epoxy resin (ROYAPOX 512), with a spacing of  $\sim 5$  cm, which allows continuous measurements on the aluminium plate heated by the resistance. At each passage of the optical fibre through the aluminium plate, a buffer of  $\sim 3$  m was attached to the ends of the plate to ensure that the measured value returned to room temperature.

---

```

Require:  $\mathbf{g}$  % DTS Reading,  $\mathbf{H}$  % Sensitivity Matrix,  $\mathbf{D}$  % Finite Difference Matrix
Require:  $\lambda = 0.6$  % Regularization Parameter
Require:  $\hat{\mathbf{f}} = \mathbf{H}' * \mathbf{g}$  % Initial Solution
Require:  $e = 10^{-9}$  % Avoids Zero Division
1: while stop >  $1e - 3$  % Minimum Update to Stop
2:  $\hat{\mathbf{f}}_0 = \hat{\mathbf{f}}$ 
3:  $\mathbf{W}_h = \text{diag}(1./(\text{abs}(\mathbf{g} - \mathbf{H} * \hat{\mathbf{f}}) + e))$  % Data Term Weights
4:  $\mathbf{W}_l = \text{diag}(1./(\text{abs}(\mathbf{D} * \hat{\mathbf{f}}) + e))$  % Penalization Term Weights
5:  $\hat{\mathbf{f}} = (\mathbf{H}' * \mathbf{W}_h * \mathbf{H} + \lambda * (\mathbf{D}' * \mathbf{W}_l * \mathbf{D}))^{-1} (\mathbf{H}' * \mathbf{W}_h * \mathbf{g})$  % Leastsquares
6: stop =  $\text{norm}(\hat{\mathbf{f}} - \hat{\mathbf{f}}_0) / \text{norm}(\hat{\mathbf{f}}_0)$  % Stopping Criterion
7: end while

```

---

Fig. 2 Reconstruction algorithm

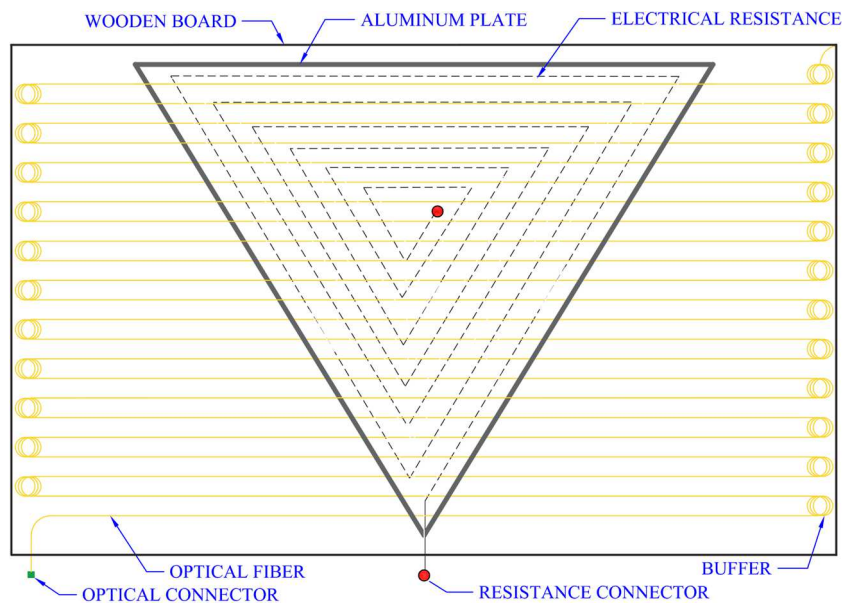


Fig. 3 Design of the validation plate, consisting of the base of wood, aluminium plate with resistive heating and fibre optic glued to the surface

The temperature measures were performed with the RDTS AP Sensing commercial equipment model N4385B with a spatial resolution of 1 m and sensitivity of  $\pm 0.1^\circ\text{C}/\text{m}$ . This equipment uses the multimode fibre, owing to a more significant numerical aperture, allowing higher coupling of backscattered light power, using the simplest detectors for Raman signals. This fibre is coated with Teflon  $\text{®}$  900  $\mu\text{m}$ , which facilitates handling, and offers more resistance to mechanical traction. Before the acquisition temperature, the RDTS is duly calibrated with a LAUDA thermal bath-model ECO RE415. When the temperature is stabilised at  $50^\circ\text{C}$ , the system is calibrated with 10 m of fibre dipped in the RDTS software as a reference. RDTS software is provided by the equipment manufacturer, which has a calibration tool for adjusting the measurement parameters.

**2.2.2 Instrumentation bar generator:** One of the stator bars from a 355 MW hydroelectric generator was instrumented in the region outside the magnetic core. This region in the generator stator has low ventilation due to the connection settings. In this way, overheating occurs, which must be monitored to avoid further damage such as the premature ageing of insulation. This bar is composed of copper, an inner layer of conductive tape, ground-wall insulation and an outer layer of the conductive tape. Fig. 4 shows the installation of the fibre in a segment of the stator bar, which is 45 cm long. To generate the heating of the bar, the electrical resistance of nickel-chrome tape (5 mm  $\times$  0.1 mm) was inserted at the bottom of the bar, with four connection outputs, allowing heating in different parts (15, 30 and 45 cm). The materials used for fixing the fibre are the same as those used in the

isolation of generators and mica paper tape. This way, it facilitates the implementation of this method on a generator in the operation.

The bars end winding have curvatures to assist in connections between bars. At these points, the heat produced limits the efficiency of the machine. Constant monitoring of temperature is fundamental, as the maximum generation can be extracted this way using the machine without the risk of heat failure.

### 2.3 Results and discussions

The results of the validation of the algorithm are presented through the plate test. The resistance power is turned on until the maximum temperature is reached ( $\sim 75^\circ\text{C}$ ). Heat is distributed throughout the aluminium plate, where the fibre is glued. The lengths of the measured fibre were 5, 15, 20, 30, 39, 50, 62, 68, 75, 86 and 100 cm. Fig. 5 shows the original RDTS reading for each length located on the heated plate. Using this result, the algorithm is applied to obtain Fig. 6, which shows the reconstructed signal.

To obtain the real temperature for each length, a PT100 sensor, type K, with Fluke  $\text{®}$  equipment 754 is employed. The ambient temperature during the whole test duration was  $28^\circ\text{C}$ . Note that for 100 cm, the temperature was  $75.6^\circ\text{C}$ , and because of the fibre length on the heated plate decreased, the temperature measured by RDTS was also lower. This occurs because the spatial resolution of the equipment is 1 m. Using the results measured by the RDTS system, the algorithm is applied for signal reconstruction.

To view the temperature distribution throughout the plate, a thermal camera was used with Fluke  $\text{®}$  Ti25. Fig. 7 shows a real image of the plate temperature (a) and the signal image

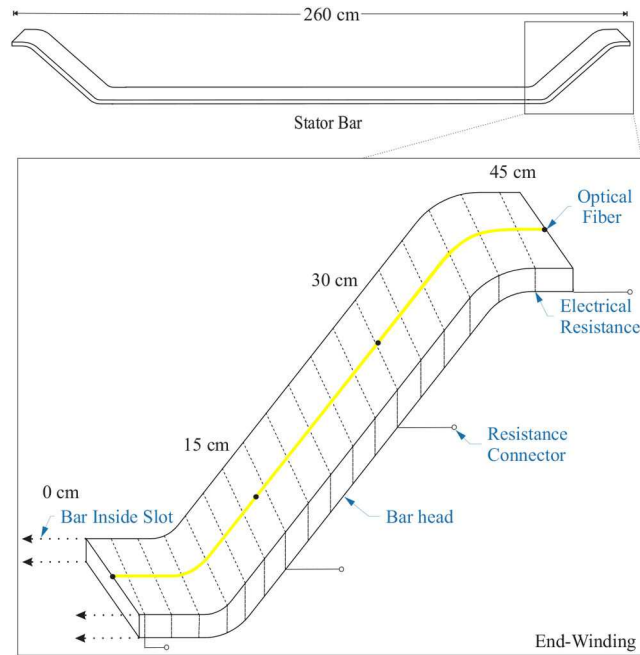


Fig. 4 Installation details of optical fibre in the end winding of generator bus

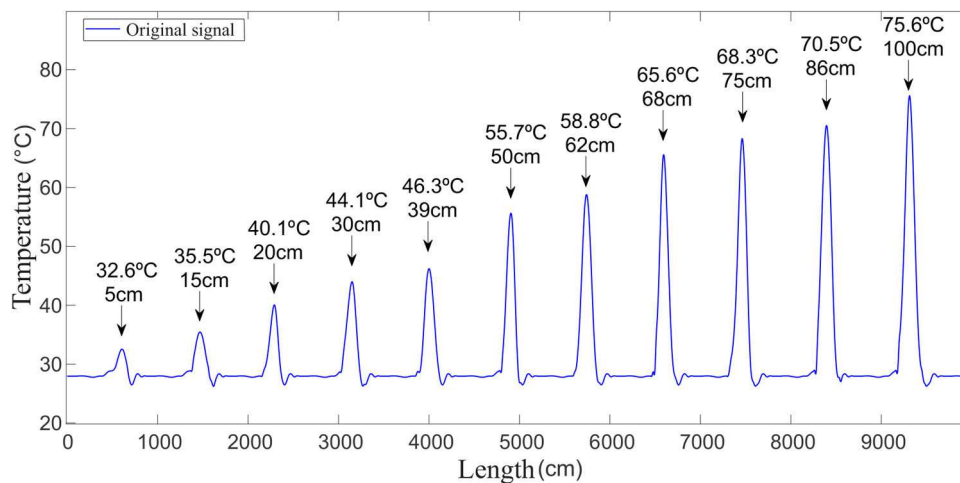


Fig. 5 Original RDTS measurement for the fibre installed on validation plate

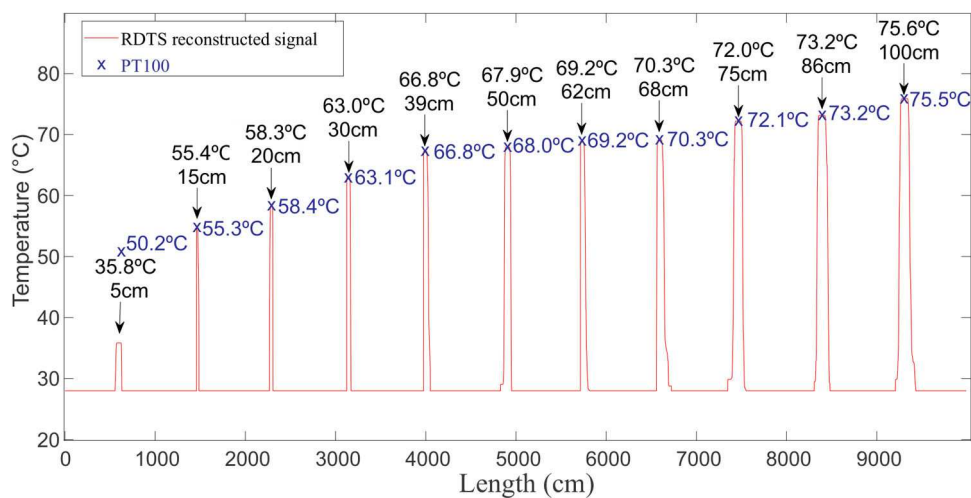
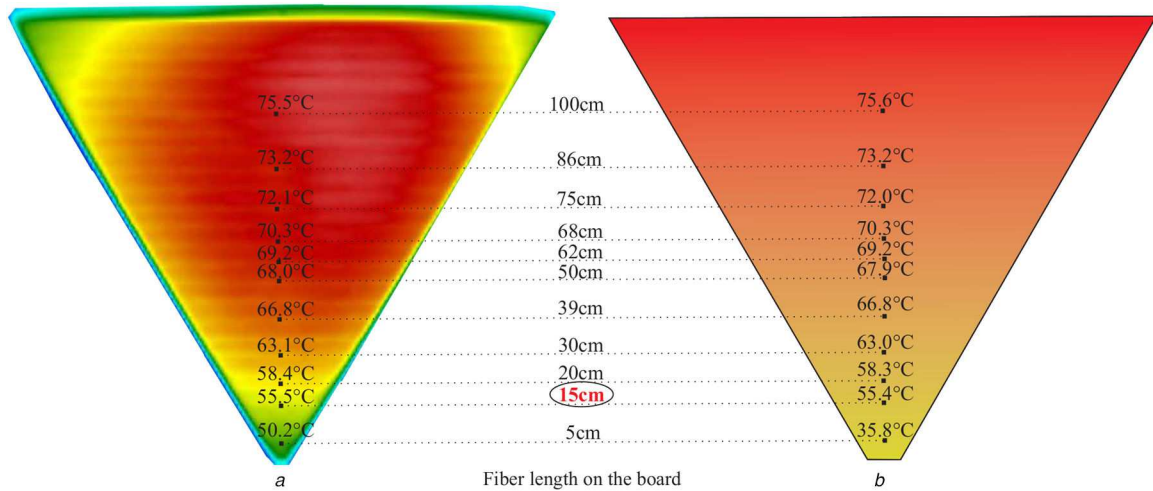


Fig. 6 Results measured by PT100 and reconstructed signal with the algorithm

reconstructed (b), which were generated from the data of the algorithm applied to the SolidWorks® software. This software presents a finite element system, which supplies temperatures to generate the temperature distribution, owing to its material (aluminium).

The proposed algorithm allows the reconstruction of the measured signal up to 15 cm in length. The value measured by the RDTS system was 35.5°C, and the reconstructed value was 55.4°C or an error of 0.2%. At a length of 5 cm, the temperature was not



**Fig. 7** Image of the plate

(a) Thermal image of the plate, highlighting the measured temperatures at the established lengths, (b) Results of image reconstruction, from the proposed algorithm, represented in the thermal analysis of the software SolidWorks®

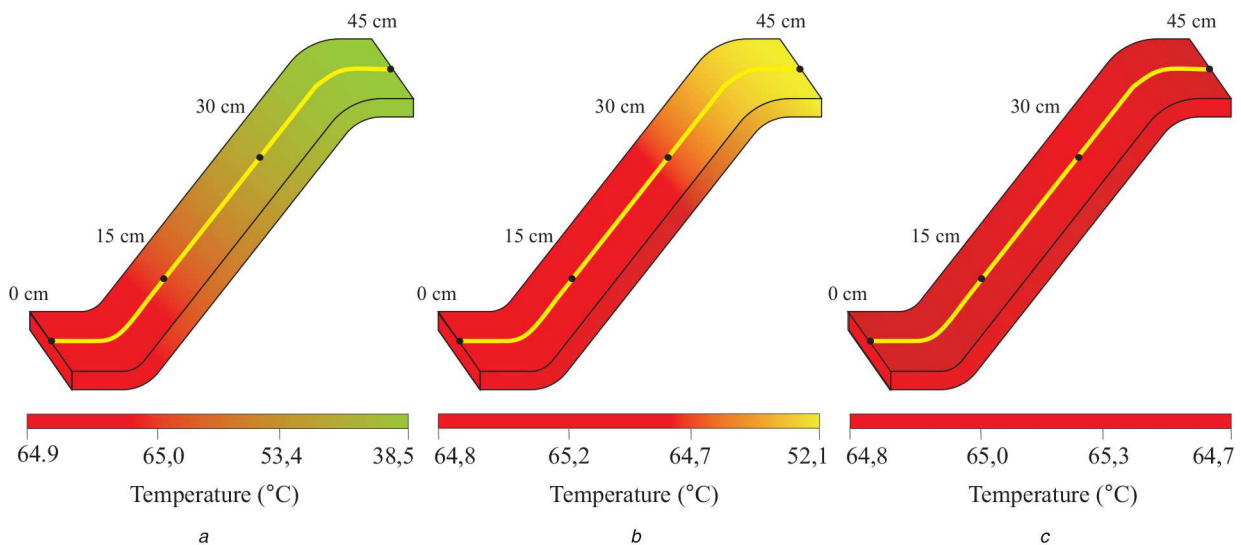


**Fig. 8** Bar segment temperature for the three tests performed

(a) Heating of 15 cm, (b) Heating of 30 cm, (c) Heating of 45 cm

close to the actual measured value 50.2°C, although an improvement was observed.

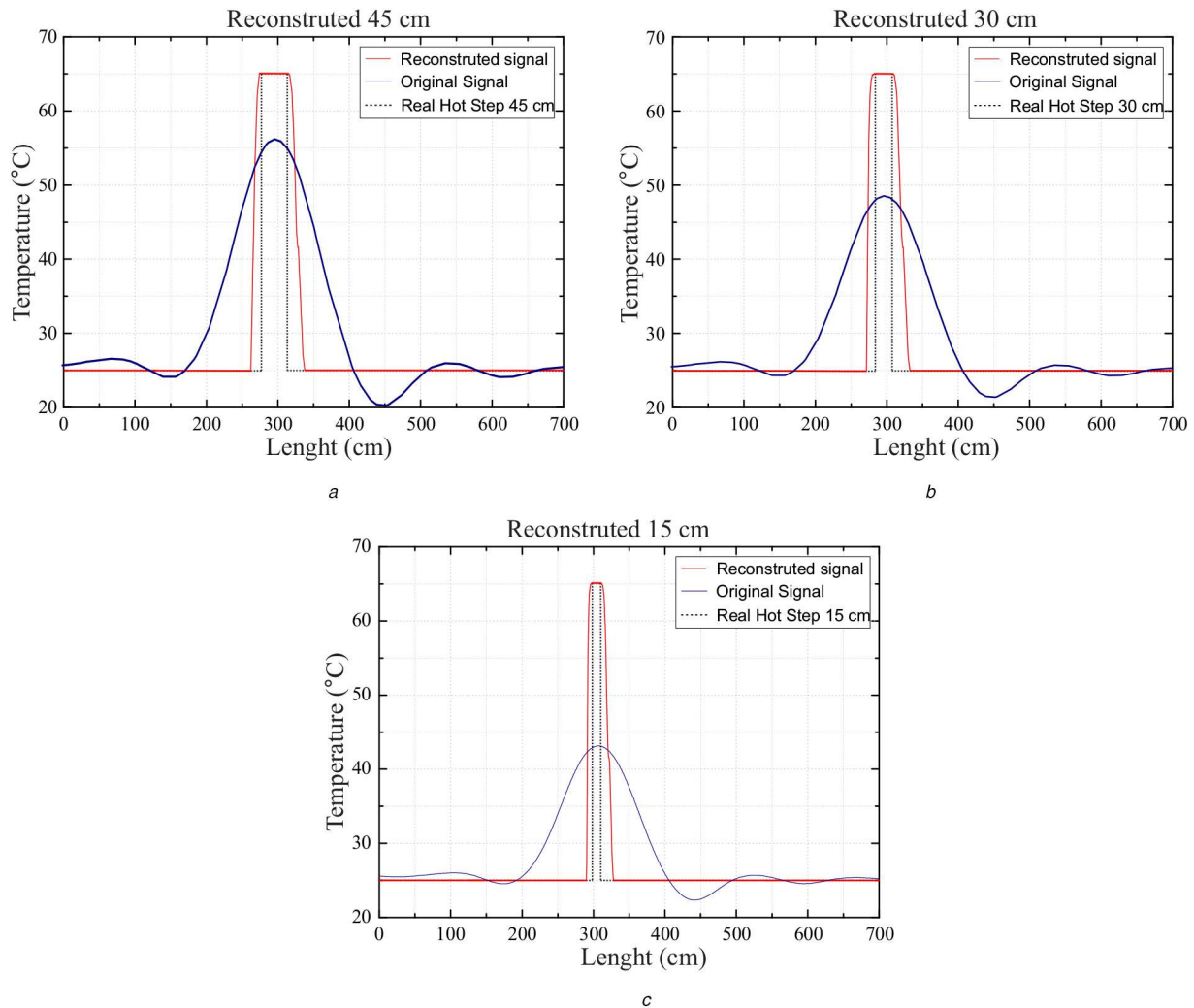
After the performance of the algorithm validation tests the temperature sensing of a stator bar was carried out. The ambient temperature during the whole test duration was 25°C. The installed electrical resistance has four terminals, so the tests were divided into three stages. First, 15 cm of resistance was heated until the surface of the bar reached a reference temperature of 65°C. Afterwards, 30 cm and finally 45 cm were heated, until the entire segment of the bar remained at approximately the same reference temperature. Fig. 8 shows the behaviour bar temperature for the three heating stages (a–c). In (a), the temperature remained at 65°C, in the 15 cm while the resistance was on, in the rest of the bar the temperature was dissipated until it reached 38.5°C. In (b) the resistance was heated to 30 cm at a temperature of ~65°C. In step (c), the entire end winding of the bar was heated and maintained at 65°C. As the bar is made of metal alloy, the temperature dissipates along the bar but does not affect the results.

Fig. 9 shows the result of the original signal, the real hot step and the signal reconstructed by the algorithm for 45 cm (a), 30 cm (b) and 15 cm (c). For the measured lengths, as the spatial resolution is 1 m, the result acquired by RDTs does not match the real value of 65°C established by the hot step. For 45 cm, the temperature at the maximum point measurement was 57°C, and an error of 12.3% with the temperature reconstruction algorithm was corrected to the actual value. Another critical factor was the length

estimated by the reconstruction on the step, which approached the real measurement of 44 cm. For the 30 cm, the measured temperature by RDTs was 48°C, and the reconstructed signal reached 65°C, with a step length close to the measured length, reaching 28 cm. For 15 cm, the temperature measured by the equipment was 33°C. As the algorithm can reconstruct the signal up to 15 cm, when applying it under these conditions, it was possible to re-establish the actual measured signal 65°C until this measurement. Besides, the reconstruction improved the step estimate, reducing the error observed at the start and end of the step, which reached 15 cm. The results show that the high resolution allows the correction of temperature measurements for hot regions with lengths up to six times smaller than the spatial resolution of RDTs.

### 3 Conclusion

This paper presents the development of a high-resolution algorithm implemented at an RDTs to monitor high-power generator bars. Using a commercial RDTs, which has a spatial resolution of 1 m, an algorithm was developed, capable of reconstructing the signal measured by the equipment. The method uses the equipment's original signal, and through the processing of signals by total variation deconvolution, the signal is reconstructed. With the construction of an experiment, the algorithm was validated, and it displayed an error of ~0.2% for 15 cm. The results demonstrate that it is possible to perform measurements in critical regions and



**Fig. 9** Comparison of results between the original and reconstructed signals using the proposed algorithm  
 (a) Reconstructed of 45 cm, (b) Reconstructed of 30 cm, (c) Reconstructed of 15 cm

small dimensions on electrical machines. The method also corrects the width of the measured section, approaching the real value. Using this algorithm, we were able to perform temperature measurements on the head generator coils. This region of the 355 MW generator bar has a length of 45 cm. Its mounting in the stator configuration presents dimensions that are difficult to access. Owing to these dimensions and the need to monitor along the bar, the RTDS system with its high-resolution algorithm is a good alternative. In the laboratory, a bar of this generator showed satisfactory results for monitoring the temperature in the end-winding region. Tests show that it is possible to measure the temperature in different boom segments with a single sensor element. The proposed method presents great potential for the monitoring of electrical machines because of the characteristics of the optical fibre and the high-resolution algorithm allows the identification of regions with temperature variations of up to 15 cm in length.

#### 4 Acknowledgments

The authors acknowledge the Federal University of Technology – Paraná (UTFPR), Federal Institute of Catarinense (IFC), (Coordination of Superior Level Staff Improvement), CNPQ (National Council for Scientific and Technological Development), FINEP (Funding Authority for Studies and Projects), Araucária Foundation, and State Secretariat of Science, Technology, and Higher Education of Paraná for the financial support.

#### 5 References

[1] Wang, N., Wang, H., Yang, S.: '3D eddy current and temperature field analysis of large hydro-generators in leading phase operations', *CES Trans.*

*Electr. Mach. Syst.*, 2019, **3**, (2), pp. 210–215. doi:10.30941/CESTEMS.2019.00028

[2] Maljković, Z., Gašparać, I.: 'Operating limits of underexcited synchronous generator'. 4th Int. Conf. on Power Engineering, Energy and Electrical Drives, Istanbul, 2013, pp. 1374–1377. doi: 10.1109/PowerEng.2013.6635814

[3] Bertalanic, Z., Maljkovic, Z., Pavlica, M.: 'Measurement of hydro-generator's end region temperature', 2008 18th Int. Conf. on Electrical Machines, Vilamoura, 2008, pp. 1–4. doi: 10.1109/ICELMACH.2008.4800076

[4] Krpal, O., Kučerová, E.: 'Comparison of voltage distribution in end-winding of synchronous generator'. Proc. of the 2014 15th Int. Scientific Conf. on Electric Power Engineering (EPE), Brno, 2014, pp. 575–578. doi: 10.1109/EPE.2014.6839410

[5] Chong, Y.C., Chick, J., Mueller, M.A., *et al.*: 'Thermal modelling of a low speed air-cooled axial flux permanent magnet generator'. 6th IET Int. Conf. on Power Electronics, Machines and Drives (PEMD 2012), Bristol, 2012, pp. 1–7. doi: 10.1049/cp.2012.0271

[6] Hudon, C., Lévesque, M., Zou, L., *et al.*: 'Determination of stator temperature profile using distributed sensing'. Proc. Electrical Insulation Conf., Ottawa, ON, Canada, June 2013, pp. 191–195

[7] Hu, C., Wang, J., Zhang, Z., *et al.*: 'Application research of distributed optical fiber temperature sensor in power system'. Proc. IEEE Communications and Photonics Conf., Shanghai, China, November 2011, pp. 1–6

[8] Kersey, A.D.: 'Optical fiber sensors for permanent downwell monitoring applications in the oil and gas industry', *IEICE Trans. Electron.*, 2000, **E83-C**, (3), pp. 400–404

[9] Yilmaz, G., Karlik, S.E.: 'A distributed optical fiber sensor for temperature detection in power cables', *Sens. Actuators A*, 2006, **125**, pp. 148–155

[10] Nokes, G.: 'Optimising power transmission and distribution networks using optical fibre distributed temperature sensing systems', *Power Eng. J.*, 1999, **13**, (6), pp. 291–296. doi: 10.1049/pe:19990608

[11] Downes, J., Leung, H.Y.: 'Distributed temperature sensing worldwide power circuit monitoring applications'. 2004 Int. Conf. on Power System Technology, 2004, PowerCon 2004, Singapore, 2004, vol. 2, pp. 1804–1809. doi: 10.1109/ICPST.2004.1460295

[12] Hoff, H.: 'Using distributed fibre optic sensors for detecting fires and hot rollers on conveyor belts'. 2nd Int. Conf. for Fibre-optic and Photonic Sensors for Industrial and Safety Applications (OFSIS), Brisbane, Australia, July 2017, pp. 70–76. doi: 10.1109/OFSIS.2017.9

- [13] Sha-lu, Z., Hui, G., Jian-yu, P., *et al.*: 'Application research of distributed optical fiber Raman temperature sensor in the security of oil depot'. Optoelectronics Global Conf. (OGC), Shenzhen, China, November 2015, 1–4, doi: 10.1109/OGC.2015.7336874
- [14] Cherukupalli, S., Anders, G.J.: 'Distributed fiber optic temperature sensing', *IEEE Distrib. Fiber Opt. Sens. Dyn. Rating Power Cables*, 2020, **1**, pp. 26–31. doi:10.1002/9781119487739.ch3
- [15] Ukil, A., Braendle, H., Krippner, P.: 'Distributed temperature sensing: review of technology and applications', *IEEE Sens. J.*, 2012, **12**, (5), pp. 885–892
- [16] Bolognini, G., Hartog, A.: 'Raman-based fibre sensors: trends and applications', *Opt. Fiber Technol.*, 2013, **19**, (6), pp. 678–688
- [17] Alem, M., Soto, M.A., Tur, M., *et al.*: 'Analytical expression and experimental validation of the Brillouin gain spectral broadening at any sensing spatial resolution'. Optical Fiber Sensors Conf. (OFS), Jeju, South Korea, June 2017, pp. 1–4, doi: 10.1117/12.2267639
- [18] Bazzo, J.P., Pipa, D.R., Martelli, C., *et al.*: 'Improving spatial resolution of Raman DTS using total variation deconvolution', *IEEE Sens. J.*, 2016, **16**, (11), pp. 4425–4430
- [19] Pelegrin, J., Bazzo, J.P., Costa, I.B.V., *et al.*: 'Total variation deconvolution of Raman distributed temperature sensing signals'. Int. Microwave and Optoelectronics Conf., Aveiro, Portugal, 2019 (IMOC)
- [20] Bazzo, J.P., Mezzadri, F., da Silva, E.V., *et al.*: 'Thermal imaging system for hydroelectric generator stator based on distributed optical sensors', *Advanced Photonic Communications (Optical Society of America)*, 2015, pp. JM3A.35
- [21] Mezzadri, F., Martelli, C., Silva, E.V., *et al.*: 'Thermal mapping of a radiator in a hydroelectric generator using fiber Bragg gratings', *Latin America Optics and Photonics Conf.*, Cancun, Mexico, 2014, pp. LTh4A–LTh40
- [22] Xue, S., Zhu, Z.Q., Wang, Y., *et al.*: 'Thermal-loss coupling analysis of an electrical machine using the improved temperature-dependent iron loss model', *IEEE Trans. Magn.*, 2018, **54**, (11), pp. 1–5, Art no. 8105005. doi: 10.1109/TMAG.2018.2842708
- [23] Tagare, D.M.: 'Risks, operation, and maintenance of hydroelectric generators', Piscataway, NJ, USA, 2011, pp. 15–43
- [24] Carunaiselvane, C., Chelliah, T.R., Khare, D.: 'Temperature distribution of 250 MW hydro turbine synchronous generator at continuous overloading conditions'. 2018 IEEE Int. Conf. on Power Electronics, Drives and Energy Systems (PEDES), Chennai, India, 2018, pp. 1–6. 10.1109/PEDES.2018.8707684
- [25] Aguilar, M.A.C., Contreras, B.M.G., Pulido, L.F., *et al.*: 'An identification technique for linear systems: application on a hydraulic testbed'. IEEE Ninth Electronics, Robotics and Automotive Mechanics Conf., doi: 10.1109/CERMA.2012.45

## **5 PAPER 04: FAULTS DIAGNOSIS IN INDUCTION MOTORS THROUGH THERMAL MAPPING PRODUCED BY THE RDTS SYSTEM**

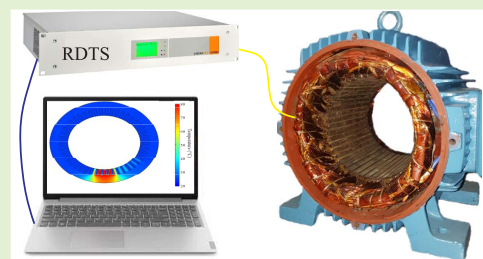
J. de Pelegrin, U. J. Dreyer, J. P. Bazzo and J. C. C. d. Silva, "Faults Diagnosis in Induction Motors Through Thermal Mapping Produced by the RDTS System," in IEEE Sensors Journal, vol. 21, no. 18, pp. 20061-20068, 15 Sept.15, 2021, doi: 10.1109/JSEN.2021.3097940.

# Faults Diagnosis in Induction Motors Through Thermal Mapping Produced by the RDTs System

Jessé de Pelegrin<sup>1</sup>, Uilian José Dreyer<sup>1</sup>, João Paulo Bazzo, and Jean Carlos Cardozo da Silva<sup>1</sup>

**Abstract**—In the industry, production lines depend on small and medium-sized electrical machines, and for this reason, continuous monitoring of these machines is important to avoid unexpected interruptions. Excessive rise in temperature during electric motor operation is usually associated with several causes, including voltage unbalance and overload. This article presents the measurements taken using a Raman Distributed Temperature Sensing (RTDS) device with 1 m spatial resolution to identify induction motor (IM) faults. In this regard, an algorithm to improving spatial resolution through signal processing allows measuring lengths of up to 15 cm. Experimental tests showed that it was possible to identify the temperature increase in four slots with an improvement of 60%. In addition, it was possible to detect faults in conditions of unbalanced voltage through temperature measurements. The proposed method shows that the measurements acquired by the distributed sensors installed in the IM stator allow thermal mapping of the machine's entire structure.

**Index Terms**—Distributed temperature sensing, electric machines, fault diagnosis, improving spatial resolution, optical fiber sensor.



## I. INTRODUCTION

INDUCTION motors (IMs) are used largely in the industry because of its reliability and robustness. These rotating electrical machines are fundamental in production systems, such as the oil industry, woodworking machines, mining industry, automotive industry, and railway applications [1]. Generally, these industries operate continuously, requiring uninterrupted operation of IMs. Therefore, continuous monitoring of the IM parameters is necessary to predict possible faults.

Faults occur primarily the stator, rotor or bearings, and are usually associated to an excessive rise in temperature and

vibration [2]. Rise in temperature and vibration levels are caused by voltage unbalance, eccentricity, and overload, which in turn lead to insulation degradation [3].

Stator faults represent 26% of defects occurring in electric motors [4]. These faults usually occur in the stator winding, such as short circuits between turns of phases, open circuit fault when winding develops breaks, turn to turn fault, and coil to coil fault [5]. Voltage unbalance is a common phenomenon in industrial plants, and contributes significantly in causing IM stator faults [6]. Voltage unbalance causes different current distributions that result in temperature asymmetry in the coils [7]. The presence of these faults generates punctual heating that deteriorates the electrical insulation [8].

Operating with IM at temperatures above the nominal value causes electrical insulation problems, reducing the motors durability. In operations where high torque is required, it is possible to apply a current higher than the rate for a period of time. This is allowed because the motor's thermal time constants are much larger than the electrical and mechanical [9]. When frequency converters are applied to supply motors and when the speed is below the nominal, the internal temperature increases because the ventilation cannot dissipate heat when there is no forced ventilation [10]. Among the temperature measurement techniques used in IMs, the most used are installation of thermocouple sensors, thermistors or

Manuscript received July 8, 2021; accepted July 13, 2021. Date of publication July 16, 2021; date of current version September 15, 2021. This work was supported in part by the Coordenação de Aperfeiçoamento de Pessoal de Nível Superior (CAPES) under Finance Code 001, in part by the Conselho Nacional de Desenvolvimento Científico e Tecnológico (CNPq), in part by the Financiadora de Estudos e Projetos (FINEP), in part by the Fundação Araucária, in part by the Secretaria da Ciência, Tecnologia e Ensino Superior (SETI), and in part by the Federal Institute Catarinense (IFC). The associate editor coordinating the review of this article and approving it for publication was Prof. Carlos Marques. (Corresponding author: Jean Carlos Cardozo da Silva.)

The authors are with the Graduate Program in Electrical and Computer Engineering, Federal University of Technology—Paraná, Curitiba, State of Paraná 80230-901, Brazil (e-mail: jesse.pelegrin@ifc.edu.br; uilianandreyer@utfpr.edu.br; jpbazzo@gmail.com; jeanccs@utfpr.edu.br).  
Digital Object Identifier 10.1109/JSEN.2021.3097940

semiconductor-based devices. However, these techniques do not provide adequate thermal mapping because of non-uniform heating of the IM components, including windings [11].

Thermal mapping through measurements of the IM's temperature distribution would be important to preserve integrity and ensure efficiency. However, for such measurements to be possible, it would be necessary to use dozens of punctual temperature sensors and/or the use of calculations methods to gather measurements in a 3D model, for example [12]. Another way of temperature mapping is by using finite element method (FEM) models applying current and voltage measurements [13]. As an alternative to these methods, this study proposes the alternative through optical sensors based on Raman distributed temperature sensing (RDTS). The optical fiber has characteristics such as small size, distributed measurement, and immunity to electromagnetic interference, which are essential for electrical machines [14]. In this way, Fiber Bragg Gratings (FBGs) sensors also have advantages, mainly due to recent researches seeking to reduce costs and improve durability through embedded sensors [15]–[17].

Bazzo *et al.* used the RDTS system for thermal imaging of hydroelectric generator stator [18]. The thermal image was generated by combining the information of temperature and the sensor's spatial position with the 3D model of the structure. The RDTS system used is based on Raman Optical Time-Domain Reflectometry technique (ROTDR). The commercial RDTS equipment available measures the temperature in fibers greater than 30 km, with detection precision of 0.1 °C and a spatial resolution of 1 m [19]. The spatial resolution is the minimum length required for the RDTS system to measure the temperature correctly. This 1 m spatial resolution feature has limitations when temperature monitoring should be performed in environments with dimensions smaller than 1 m. To work around this limitation Bazzo *et al.* proposed improving spatial resolution of RDTS using Total Variation Deconvolution [20]. This method uses the equipment's original signal, and through the processing of signals by total variation deconvolution, the signal is reconstructed. Following the same methodology, Pelegrin *et al.* validated and applied the strategy of the final winding of a generator bar of a 355 MW hydroelectric plant instrumented in the laboratory [21]. However, the researchers were carried out on machines with dimensions larger than 2 m. Thus, the main contribution of this work is the thermal mapping of small and medium-sized electrical machines, on the scale of centimeters, with the possibility of identifying faults that compromise the integrity of the IM. The proposed method can increase the machine's operational availability, avoiding interruptions in essential and aggressive systems such as water distribution, refineries, and mining.

## II. MATERIALS AND METHODS

### A. Distributed Temperature Sensing System

The main technologies of Distributed Temperature Sensing (DTS) are based on Rayleigh, Brillouin, and Raman scattering. Rayleigh scattering is usually thought to be insensitive to temperature, and special optical fibers have to increase sensitivity [22]. Brillouin scattering are caused by lattice vibrations from the propagating light pulse. These peaks are

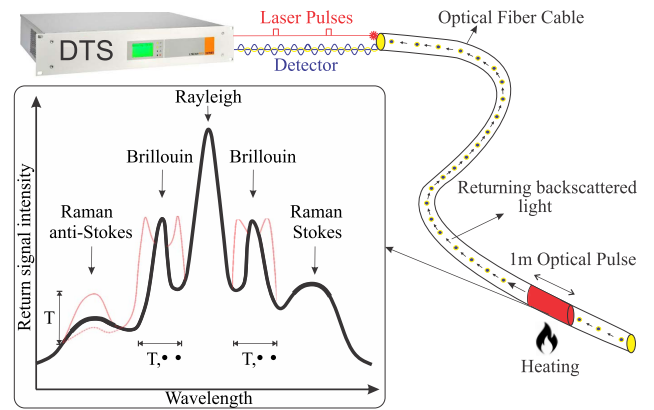


Fig. 1. Operation of the DTS from the emission of the pulsed laser, detection of heat in 1 m of fiber and return of backscattered light. In detail, backscattered spectral components.

spectrally close to the primary laser pulse, that it is difficult to separate them from the Rayleigh signal [23].

The RDTS system used is based on the varied properties produced in fiber optic cables through Raman scattering because of temperature changes. An optical source emits a laser pulse that propagates through the fiber, returning scattered light to a photodetector [24]. The pulsed laser interacts with the fiber molecules generating an energy exchange between the photons of the incident light and the fiber molecules. New electromagnetic fields are generated with different frequencies that are backscattered by the fiber. For backscattered light with a frequency lower than the incident light, the effect is known as Stokes and if the backscattered light has a higher frequency than the incident light, the effect is known as anti-Stokes [25].

Fiber molecules associated with light scattering are sensitive to temperature variations. Therefore, from the Stokes and anti-Stokes scattering, it is possible to estimate the fiber's temperature value [26]. Fig. 1 shows the DTS emitting the laser pulse and receiving the scattered light after detecting heat in 1 m of fiber. The analysis is performed in the bands referring to Raman anti-Stokes and Stokes, which are more sensitive to heat variation. The temperature can be determined by the relationship between the power of Stokes and anti-Stokes, according to Eq. 1 [27],

$$T(l) = \frac{\Delta E}{k} \cdot \frac{1}{\ln[C] - \ln\left[\frac{P_S(l)}{P_{aS}(l)}\right] + \Delta\alpha} \quad (1)$$

where  $T(l)$  is the temperature at a distance  $l$  along the fiber;  $\Delta E$  represents the difference in molecular energy states that drive Raman scattering;  $k$  is the Boltzmann constant;  $C$  is a calibration parameter at the DTS system;  $P_S(l)$  and  $P_{aS}(l)$  represent the power of the bands of Stokes and anti-Stokes at distance  $l$ , respectively;  $\Delta\alpha$  is the difference of attenuation between the power of the Stokes and anti-Stokes signals.

Although the RDTS system has easy applicability, the temperature measurement precision depends on the parameter determined spatial resolution ( $\delta_z$ ). The spatial resolution is the minimum length required for the RDTS to perform the correct measurement. It is defined as the spatial distance between the 10% and 90% levels of the response to a temperature step [19].

The spatial resolution of 1 m is related to the laser pulses width of the equipment, which is 10 ns. Temperature measurements performed on fiber length less than the equipment's spatial resolution indicated lower temperature, not corresponding to the actual temperature [28].

To apply RDTS to electrical machines a better spatial resolution must be achieved to monitor hot spots smaller than 1 m. There are commercial types of equipment with a spatial resolution of 10 cm, such as those using Brillouin backscattered components. These devices are complex and expensive. The pulse of light propagation is spectrally so close to the primary laser pulse that it is not easy to separate them from the Rayleigh signal [23]. Therefore, optical sensors based on RDTS are an appropriate option for monitoring electrical machines. However, to make it possible to apply this technique to smaller electrical machines, it is necessary to improve spatial resolution.

### B. Improving Spatial Resolution

Improving spatial resolution has been studied in the scientific community in recent years [29]–[31]. Early research generally focused on Eq. 2 that determines the spatial resolution [32],

$$\delta_z = \frac{C_o \cdot \tau}{2 \cdot n_{gr}} \quad (2)$$

where  $C_o$  is the speed of light vacuum,  $\tau$  is laser pulse duration, and  $n_{gr}$  is the group refractive index of the fiber core. The problem in this method is that the equipment hardware needs to be modified. Therefore, the methods that have been used are mathematical models [30]. With mathematical models, it is not necessary to change the hardware of the equipment, but implementing algorithms on the measured results are adequate.

In this article, an algorithm is used to improve the spatial resolution of the RDTS equipment through a signal processing algorithm based on deconvolution by a total variation to map the temperature of an IM. The method is based on the mathematical model developed by Bazzo *et al.* [20] and adapted for application in small and medium-sized electrical machines. The method is capable of improving spatial resolution by up to 15 cm. The algorithm is based on a signal deconvolution process that uses the linear model of the RDTS and total variation regularization. The working principle of the algorithm is summarized in block diagram shown in Fig. 2, where  $f(z)$  is the real temperature profile,  $h(z)$  is the impulse response of the RDTS system and  $g(z)$  is the signal convolution response. The Laplace transform was applied to obtain  $G(s)$ . The poles ( $\beta_i$ ) and zeros ( $\alpha_i$ ) of the function  $H(s)$  were estimated. It is rewritten in a matrix notation and considers vector  $\mathbf{n}$  as all noise sources that are inherent to the measurement system. To regulate the signal, total variation was applied because of the fact that the RDTS equipment has characteristics of a low-pass systems and impulse spreads.

The reconstructed signal  $\hat{\mathbf{f}}$  results from a balance between a data-fidelity term and a prior term based on finite differences. The balance is controlled by the parameter  $\lambda$ : higher values of  $\lambda$  yields to smoother reconstructed signals. Furthermore, one can control the assumed distribution of the residuals by changing  $0 < p \leq 2$ .

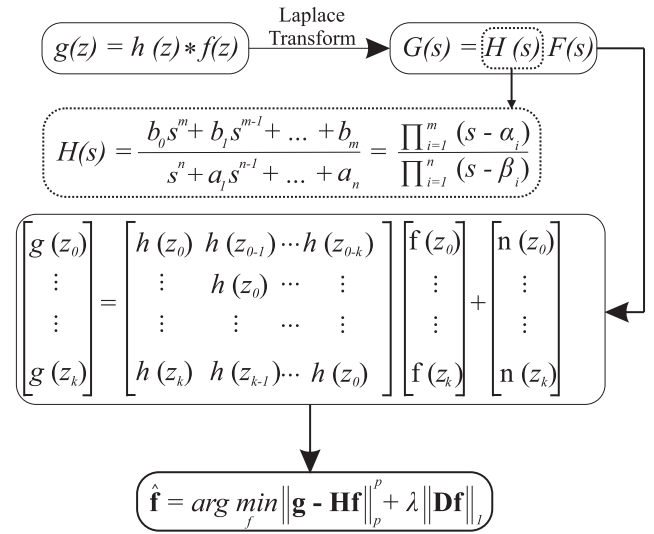


Fig. 2. Block diagram of the algorithm used improve the spatial resolution of the RDTS equipment.

The algorithm was tested experimentally and the results demonstrated the effectiveness of the proposed method [20]. The algorithm was applied to measure the temperature in the end-winding region with optical sensors based on RDTS [21].

### C. Unbalance Voltage on Induction Motor

The IM operates with best efficiency when connected to a perfectly symmetrical power source. However, industrial plants may show voltage fluctuations because of irregular distribution by phase and type of connected loads. IM operation under unbalanced voltages can cause serious effects, such as overheating, decreased efficiency, and reduced torque [33]. As it is a recurring problem in the industry and given the importance of the effects caused, this study, will investigate the effect of the voltage unbalance on the temperature in the IM stator. Although IMs support small unbalanced voltage, with the passage of time, the effects compromise the integrity of the IM. To avoid these problems, it is important to diagnose them at the incipient stage [34]. The unbalance of the phase voltage can be determined by Eq. 3 [35],

$$\%PVUr = \frac{MVD}{V_{AVG}} \cdot 100 \quad (3)$$

where MVD is the maximum voltage deviation from the average line voltage magnitude;  $V_{AVG}$  is the average line voltage magnitude.

According to IEEE Guide for AC Motor, voltage deviation is  $\pm 10\%$  of their rated value, and the ratio between the negative and positive sequence voltage components should not exceed 2%. Given the insulation system's dielectric properties for a 10°C increase in temperature, the life of the motor halves [36].

## III. DESIGN AND INSTALLATION PRINCIPLES

### A. Experimental Setup

The experimental setup is shown schematically in Fig. 3, where the yellow line indicates the optical fiber. The instrumentation is used to obtain the temperature of the IM when

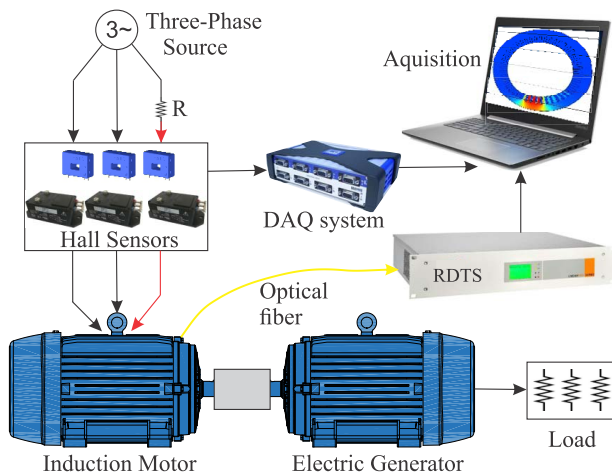


Fig. 3. Experimental setup.

subjected to unbalanced voltage. The electrical resistance is used to produce a voltage drop of about  $38 V_{rms}$ . Three tests were carried out with the IM operating with unbalanced voltage in each of the phases, respectively. The three-phase line current and voltage are measured by three Hall Effect Current Sensors LA 55-P (LEM<sup>®</sup>) and three Hall Effect Voltage Sensors LV 25-600/SP7 (LEM<sup>®</sup>), respectively. A data acquisition (DAQ) system is used for the signal conditioning of the current and voltage sensors. The used DAQ system was the Quantum X-840, with eight input channels and a maximum sampling rate of 20 kHz, manufactured by HBM<sup>®</sup>. The optical fiber is measured by RDTS AP Sensing commercial equipment model N4385B with a spatial resolution of 1 m and sensitivity of  $\pm 0.1$  °C/m.

Data acquisition was performed with the commercial software catmanEasy – HBM<sup>®</sup>, which allows the simultaneous acquisition of the current and voltage signals from the Hall sensors. For RDTS measurements, the software used is DTS Configurator - AP Sensing<sup>®</sup>.

### B. Stator Instrumentation

The instrumented IM comprises 4-pole, 15 HP, connected to 220 V, 60 Hz, insulation class F, 48 slots, 12 coils, double layer winding, and 1-11 coil span. Fig 4 shows a partial stator planified scheme to illustrate the electrical resistance and the optical fiber installation in the stator. The electrical resistance was inserted in four slots where a coil that constitutes one of the phases is inserted. This installation allows inducing heating in a small IM stator portion emulating the effect of an unbalanced voltage.

The stator's optical instrumentation used a multimode fiber 50/125  $\mu\text{m}$  graded-index coated with a protective Teflon<sup>®</sup> 900  $\mu\text{m}$  cover. This fiber is compatible with the specifications of RDTS, allowing greater power coupling of the back-scattered light. The coating with Teflon<sup>®</sup> 900  $\mu\text{m}$  provides greater resistance to mechanical traction allowing safe handling of stator rewinding. The fiber was installed inside the stator slot between the core and the insulating paper, before the insertion of the coils. The maximum hotspot temperature allowed in IMs is 155°C [36]. This temperature is compatible with the optical fiber installed, offering greater instrumentation

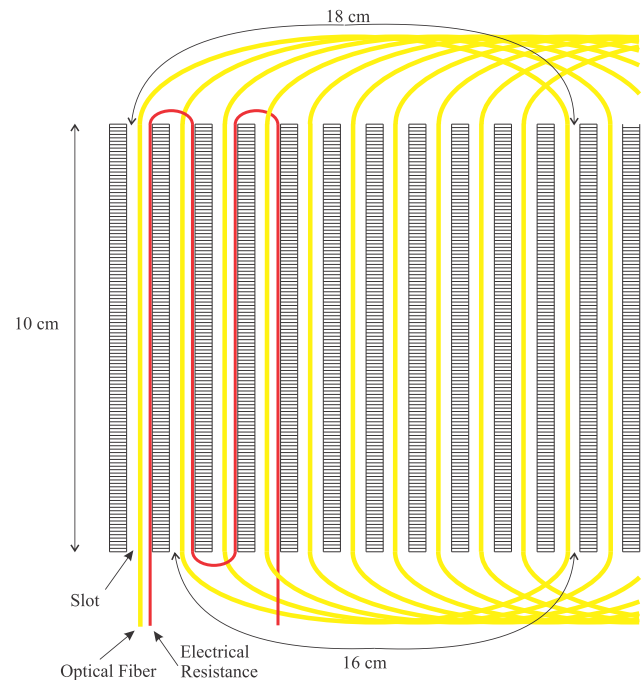


Fig. 4. Planified stator scheme with optical fiber and inner slots electric resistance.

durability. The configuration of the optical fiber installation must be uniform following the configuration of the coils. This way, there is no influence between temperature measurements of different coils, and it is possible to identify the heating region. The advantages of this instrumentation method are that the sensor is directly in contact with the measuring, can be installed on new or rewound machines, and it is easy to implement.

Fig. 4 shows the dimensions related to the length of the installed optical fiber. The length of the slot is 10 cm, the fiber at the top is 18 cm and the bottom is 16 cm, totaling approximately 16 m of fiber installed in the stator. The fiber curves do not present losses that could influence the system. In the slots with the resistance there are 40 cm of fiber, of which for each 1 m of fiber we have 20 cm in the region of the resistance. This length is enough for the algorithm to be able to reconstruct the temperature RDTS measurement. A type K thermocouple probe sensor, a Fluke<sup>®</sup> 754, installed inside the slot, was used to measure the resistance's accurate temperature.

### C. Testing Procedures

The thermal mapping of the IM stator is performed with the motor operating at rated load. An electrical generator connected to variable resistive loads is coupled to the IM, producing different load profiles. In the tests, the IM is activated until the temperature stabilizes at 43°C. This temperature was established through the simulation, and measured using the K thermocouple probe. A variable voltage source connects the inserted electrical resistance. The temperature produced by the electrical resistance is monitored by the K thermocouple sensor to prevent damage to the IM electrical insulation. To map the temperature, measurements are monitored by RDTS.

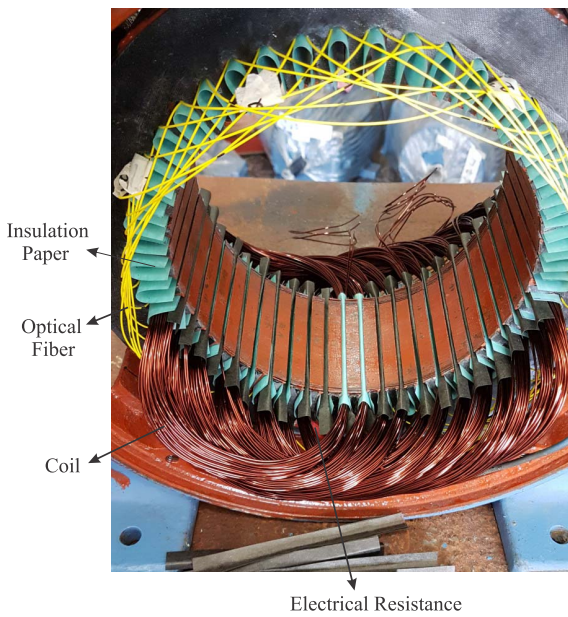


Fig. 5. Instrumentation of the fiber between the stator core and the insulating paper.

Before the acquisition temperature, the RDTs is duly calibrated with a LAUDA thermal bath-model ECO RE415. RDTs software is provided by the equipment manufacturer, which has a calibration tool for adjusting the measurement parameters.

In the calibration procedure, 20 m of optical fiber are immersed in the thermal bath at a temperature of 50°C, 10 m before instrumenting the IM, and 10 m at the end. This procedure is essential for the accurate measurement of the RDTs system, so that the algorithm also reaches the expected results.

To evaluate the use of the RDTs system to map the temperature and diagnose faults in the proposed IM, two faults were experimentally induced in the IM through the installed electrical resistance that produces heating in four slots and through the IM supply's unbalanced voltage. The electrical resistance is connected in series in one of the phases that supply the motor to generate the unbalanced voltage. Tests with the electrical resistance in series are implemented in the three phases separately. To predict the temperature in the IM, in Section IV-A, simulations were performed. Based on the theoretical results, experimental tests were conducted, maintaining the electrical insulation's integrity in the face of the increase in temperature.

#### IV. SIMULATION, EXPERIMENTAL RESULTS AND DISCUSSION

##### A. Temperature Simulation of the Instrumented IM

To compare the practical and theoretical effects of the temperature behavior in the instrumented IM, simulations were performed using the Motor-CAD software. Motor-CAD is the dedicated electric motor design software for multiphysics simulation of electrical machines. With the characteristics and dimensions of the IM, the simulation is performed under rated

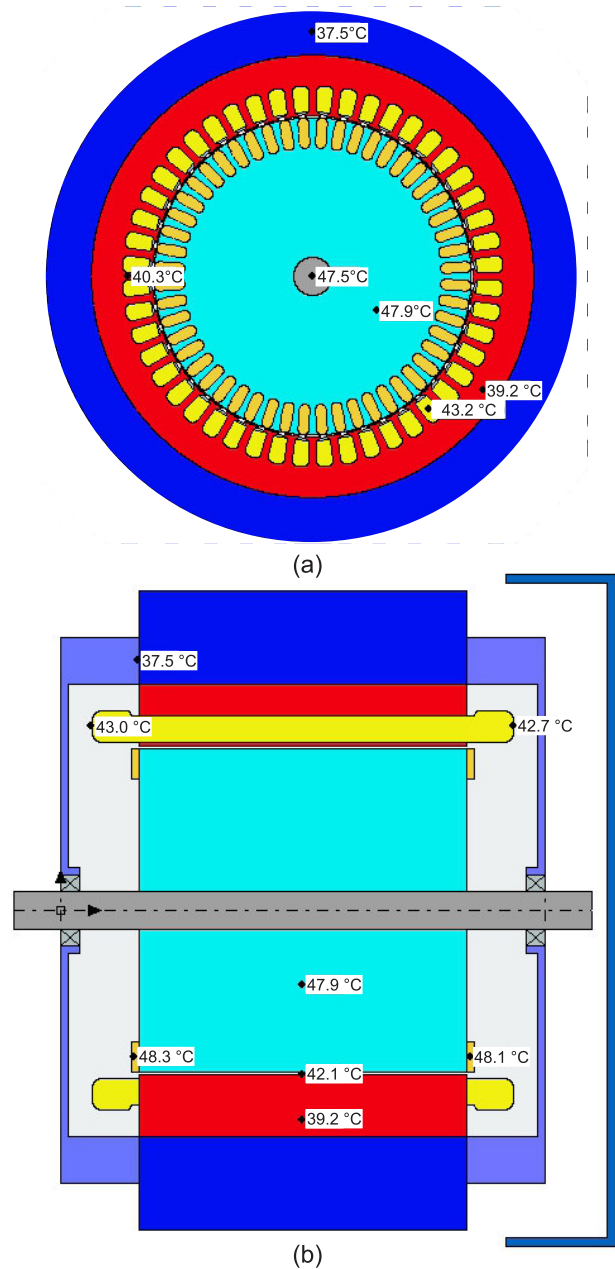


Fig. 6. Simulation of the IM temperature with the Motor-Cad software. (a) Cross section. (b) Longitudinal section of the IM.

load. Fig. 6 presents the simulated temperature results for the IM of 15 HP; with load, (a) shows a cross section, and (b) shows the longitudinal section of the IM.

The temperature in the simulation indicates 43.2°C in the inside the slot, stator iron 39.2°C, and enclosure 37.5°C. In the region between the slots, called teeth, the temperature is 40.3°C. Other temperature points are rotor bars 48.3°C, rotor 47.9°C, and top of the teeth 42.1°C. As the objective of the study is to monitor the temperature of the stator, we will concentrate on stator inside slots. Using the results of the simulation, the temperature limits are established allowing the experimental tests to be carried out without damaging the machine.

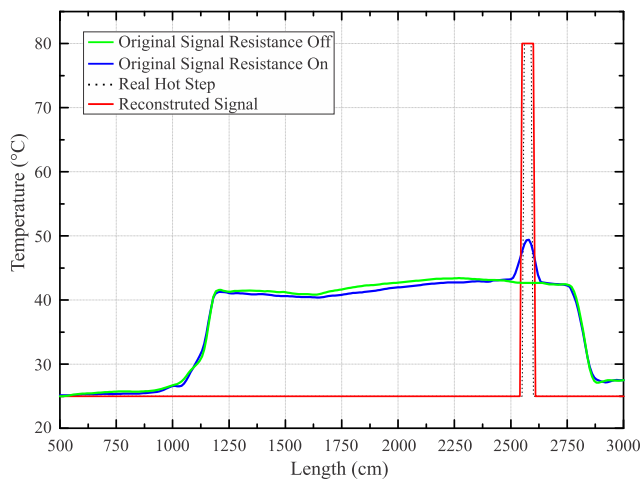


Fig. 7. Motor stator temperature measurement with induced heating in 4 slots.

### B. Faults Analysis Produced in a Coil by Heating the Resistance

Based on the experimental setup developed using the proposed instrumentation and the simulation, the tests are conducted to identify the temperature increase in the IM stator caused by faults. Fig. 7 shows the measurement of IM temperature with RDTS system at full load. The ambient temperature during the whole test duration was 25°C. The IM remained on until the temperature stabilized, approximately at 40°C (green line). Subsequently, the electrical resistance was switched on until the temperature reached 80°C measured by K thermocouple sensor installed inside the slot. This value, despite being high, does not damage the electrical insulation of the IM, as the insulating paper used supports 200 °C. As the temperature increases, the RDTS identifies the temperature increase between the lengths 2500 and 2625 cm of the fiber with a peak of 48°C (blue line). This value does not correspond to the actual temperature of the 80°C. This occurs because the spatial resolution of the equipment is 1 m. Using the results measured by the RDTS system, the algorithm is applied for signal reconstruction. The high resolution algorithm identifies the peak temperature and reconstructs the signal with the real temperature value. The algorithm allows the reconstruction of the measured signal up to 15 cm in length. As medium and large seized IMs have slots greater than 15 cm, it is possible to estimate the temperature with the proposed system. However, even without using the algorithm to improve spatial resolution, the peak temperature measured by RDTS is already an indication of fault to be considered.

To visualize the heating, COMSOL® software is used. The analysis is performed considering the thermal conductivity of copper and iron with 400 (W/m.K) and 150 (W/m.K), respectively. Fig. 8 shows that the IM stopped when the electrical resistance was connected indicating the spread of the temperature caused by the electrical resistance. The region near the resistance shows a temperature of 80°C that scatters through the stator iron core. Fig. 9 presents the IM operating under load and the electrical resistance connected. Knowing

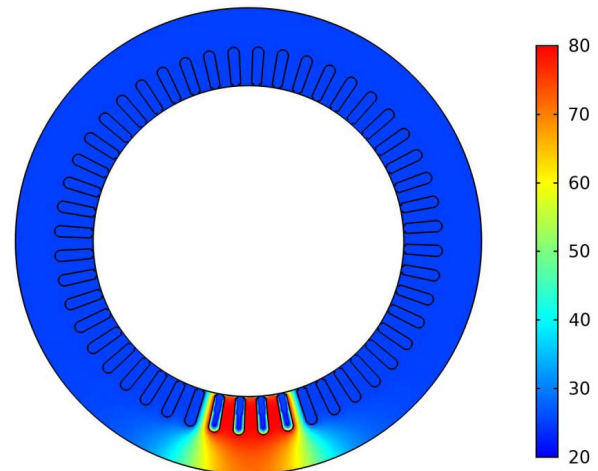


Fig. 8. Thermal image of the stator with the IM stopped and electrical resistance on.

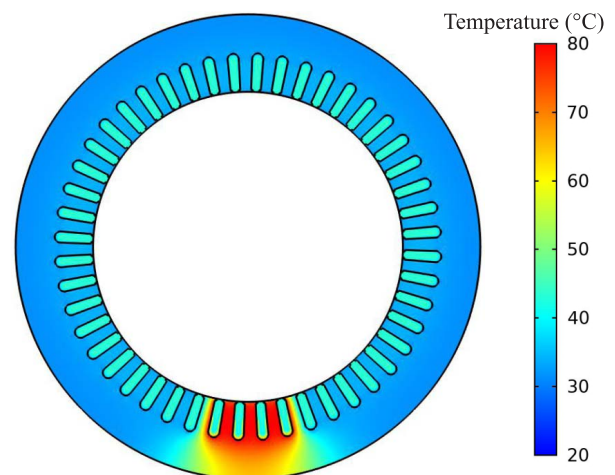


Fig. 9. Thermal image of the stator with the IM operating under load and electrical resistance on.

the length of the fiber, it is possible to verify the region in which the faults occur through the image.

### C. Temperature Rise During Voltage Unbalance

The efficiency and integrity of IM depends on balanced supply voltages. Under conditions of unbalanced voltage, the IM presents temperature variations that compromise the electrical insulation. Using the experimental setup described in Section III, unbalanced voltage tests were performed. The IM was activated with electrical resistance in series in one of the phases at time and operated at rated load at time. Fig. 10 shows the waveform of the voltages with the electrical resistance in the A phase. The voltage of phase B (blue line) and voltage of phase C (black line) maintained the rated peak voltage of 311 V (220  $V_{rms}$ ). The voltage of phase A (red line) presented a voltage drop of 18%. The waveform of the currents is shown in Fig. 11. The currents of phases B and C were measured to be 23.8  $A_{rms}$ . However, the current of phase A showed a reduction of 41% concerning the currents B e C and a delay of 4.6 ms concerning the original position. The delay occurs because of the weakening of the electromagnetic field

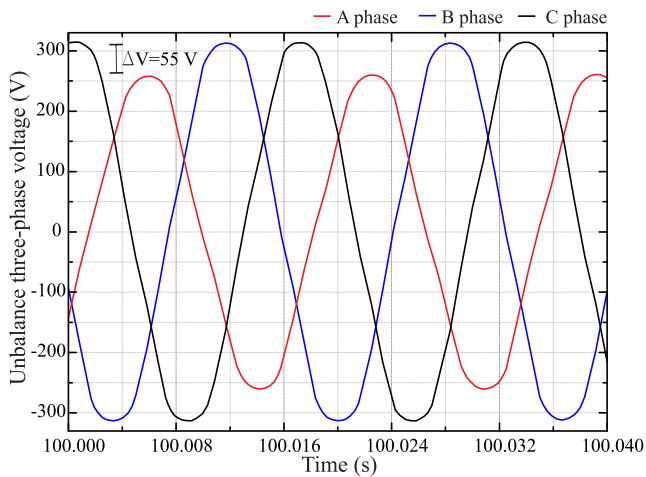


Fig. 10. Measurements of the electrical voltages the IM with unbalance voltage of phase A.

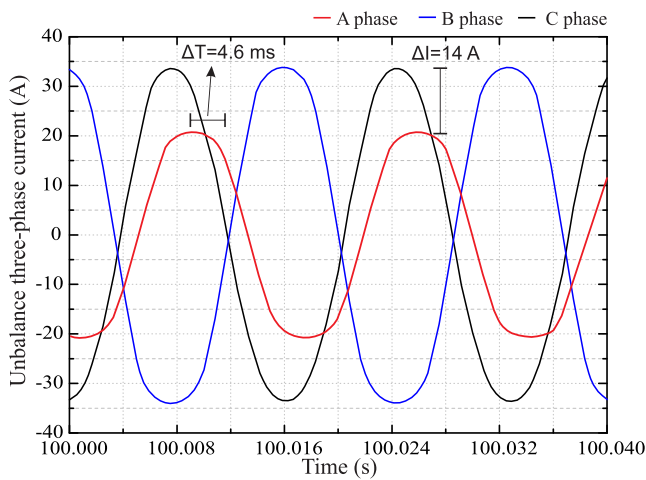


Fig. 11. Measurements of the electrical currents the IM with unbalance voltage of phase.

at A phase [37]. The electrical resistance was also inserted in series with the B and C phases, and they present the same unbalances shown in the A phase.

The unbalance voltage (UV) caused temperature variations in the IM measured by the RDTs system. Fig 12 presents four measurements, without UV, UV phase A, B and C. It was noted that under normal conditions the temperature remained constant throughout the structure, at approximately 40 °C. It can be seen that in the lower region of the IM where the maximum heat dissipation occurs, the temperature is slightly lower. However, for each phase in which the unbalanced voltage was subjected, the temperature measured changed according to the fiber distribution in the stator. Despite presenting little variation, a difference in temperature is perceived according to the phase in which the voltage unbalance occurs. Unbalanced voltage of phase A showed a higher temperature between 1180-1440 cm and 2280-2550 cm. In the unbalanced voltage of phase C, the temperature increased between 1600-1900 cm and 2430-2650 cm. In the unbalanced voltage of phase B, the increase in temperature was only in 1810-2425 cm. As the objective was to measure the

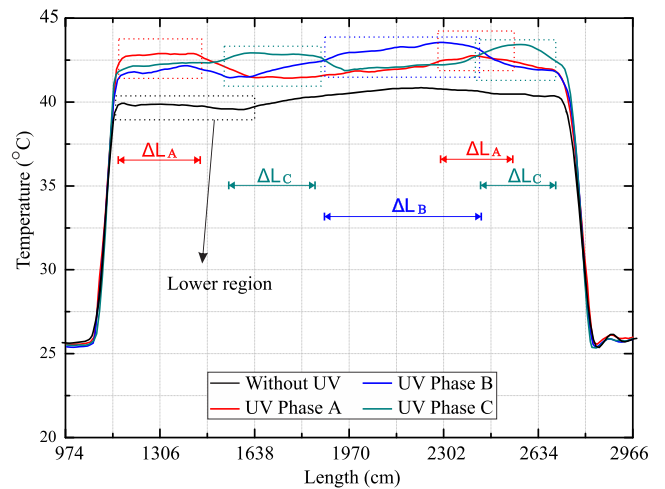


Fig. 12. IM temperature measurements, under normal conditions and with unbalance voltage.

temperature of the coils, there was no need to apply the algorithm, as the spatial resolution of 1 m was sufficient. That is because the distribution of the optical fiber is the same as that of the coils.

The results identify an imbalance in temperature in different parts of the IM structure. As the fiber installation followed the same settings as the coils that are a double layer winding (2 coils in the same slots), the measured temperature was influenced by the overlap of the coils. However, it was possible to identify the unbalance voltage even in a double layer winding. That is, even for a single layer winding, it is possible to detect the unbalanced voltage.

## V. CONCLUSION

This article presents a different technique for monitoring the stator temperature of medium sized induction motor using distributed temperature sensing. The experiments are performed in the induction motor instrumented internally with optical fiber before the insertion of the coils. Despite being a known method, they are generally used on large dimension machines, and this study shows that it can also be applied on smaller machines. Through improving the spacial resolution algorithm, it was shown that it is possible to obtain temperature measurements up to 15 cm in length. With the algorithm applied to the measured signal it was possible to obtain an improvement of 60% in relation to the original signal.

The results demonstrate that it is possible to diagnose faults in the windings as well as unbalanced voltage through temperature. With the uniform distribution of the optical fiber through the slots, if heat sources can be detected even in their initial stage, repairing becomes simpler, reducing downtime, thereby increasing the induction motor's operational efficiency.

The constant monitoring of the internal temperature of the induction motor can be a fundamental, predictive maintenance tool. As the high temperature degrades the electrical insulation, the proposed application method evaluates if the temperature degree has exceeded the limit. Another relevant factor is the possibility of identifying the region of the structure in which the defect occurred. Therefore, the instrumentation

described in this study offers a promising alternative in the thermal mapping of electrical machines. The instrumentation will allow detailing the 3D thermal mapping in future work. The proposed method can still be improved by changing the installation configuration of the optical fiber and through optical systems with better spatial resolutions.

#### ACKNOWLEDGMENT

The authors acknowledge Coordination of Superior Level Staff Improvement (CAPES), National Council for Scientific and Technological Development (CNPQ), Funding Authority for Studies and Projects (FINEP), Araucária Foundation, and State Secretary of Science, Technology, and Higher Education of Paraná (SETI), and Multi-User Photonics Facility—UTFPR-CT, Federal Institute of Catarinense (IFC).

#### REFERENCES

- [1] A. Glowacz and Z. Glowacz, "Diagnosis of the three-phase induction motor using thermal imaging," *Inf. Phys. Technol.*, vol. 81, pp. 7–16, Mar. 2017, doi: [10.1016/j.infrared.2016.12.003](https://doi.org/10.1016/j.infrared.2016.12.003).
- [2] A. Choudhary, D. Goyal, S. L. Shimi, and A. Akula, "Condition monitoring and fault diagnosis of induction motors: A review," *Arch. Comput. Methods Eng.*, vol. 26, no. 4, pp. 1221–1238, Sep. 2019, doi: [10.1007/s11831-018-9286-z](https://doi.org/10.1007/s11831-018-9286-z).
- [3] K. M. Sousa, U. J. Dreyer, C. Martelli, and J. C. C. da Silva, "Dynamic eccentricity induced in induction motor detected by optical fiber Bragg grating strain sensors," *IEEE Sensors J.*, vol. 16, no. 12, pp. 4786–4792, Jun. 2016, doi: [10.1109/JSEN.2016.2554885](https://doi.org/10.1109/JSEN.2016.2554885).
- [4] *IEEE Recommended Practice for The Design of Reliable Industrial and Commercial Power Systems*, IEEE Standard 493-1997, 1997.
- [5] X. Liang, M. Z. Ali, and H. Zhang, "Induction motors fault diagnosis using finite element method: A review," *IEEE Trans. Ind. Appl.*, vol. 56, no. 2, pp. 1205–1217, Mar. 2020, doi: [10.1109/TIA.2019.2958908](https://doi.org/10.1109/TIA.2019.2958908).
- [6] M. Al-Badri, P. Pillay, and P. Angers, "A novel technique for in situ efficiency estimation of three-phase IM operating with unbalanced voltages," *IEEE Trans. Ind. Appl.*, vol. 52, no. 4, pp. 2843–2855, Jul. 2016.
- [7] D. Springer, E. Stolz, and E. Wiedenbrug, "Experimental analysis of industry standards on derating of a three-phase induction motor due to thermal stress caused by voltage unbalance," in *Proc. IEEE Energy Convers. Congr. Expo.*, San Jose, CA, USA, Sep. 2009, pp. 1304–1308, doi: [10.1109/ECCE.2009.5316360](https://doi.org/10.1109/ECCE.2009.5316360).
- [8] S. Grubic, J. M. Aller, B. Lu, and T. G. Habetler, "A survey on testing and monitoring methods for stator insulation systems of low-voltage induction machines focusing on turn insulation problems," *IEEE Trans. Ind. Electron.*, vol. 55, no. 12, pp. 4127–4136, Dec. 2008.
- [9] M. O. Sonnaillon, G. Bisheimer, C. De Angelo, and G. O. García, "Online sensorless induction motor temperature monitoring," *IEEE Trans. Energy Convers.*, vol. 25, no. 2, pp. 273–280, Jun. 2010, doi: [10.1109/TEC.2010.2042220](https://doi.org/10.1109/TEC.2010.2042220).
- [10] H. Karkkainen, L. Aarniovuori, M. Niemela, and J. Pyrhonen, "Converter-fed induction motor efficiency: Practical applicability of IEC methods," *IEEE Ind. Electron. Mag.*, vol. 11, no. 2, pp. 45–57, Jun. 2017, doi: [10.1109/MIE.2017.2693421](https://doi.org/10.1109/MIE.2017.2693421).
- [11] F. Ahmed and N. C. Kar, "Analysis of end-winding thermal effects in a totally enclosed fan-cooled induction motor with a die cast copper rotor," *IEEE Trans. Ind. Appl.*, vol. 53, no. 3, pp. 3098–3109, Jun. 2017, doi: [10.1109/TIA.2017.2648780](https://doi.org/10.1109/TIA.2017.2648780).
- [12] Y. Xie and Y. Wang, "3D temperature field analysis of the induction motors with broken bar fault," *Appl. Thermal Eng.*, vol. 66, nos. 1–2, pp. 25–34, May 2014, doi: [10.1016/j.applthermaleng.2014.02.008](https://doi.org/10.1016/j.applthermaleng.2014.02.008).
- [13] J. Martinez, A. Belahcen, and A. Muetze, "Analysis of the vibration magnitude of an induction motor with different numbers of broken bars," *IEEE Trans. Ind. Appl.*, vol. 53, no. 3, pp. 2711–2720, May 2017, doi: [10.1109/TIA.2017.2657478](https://doi.org/10.1109/TIA.2017.2657478).
- [14] J. de Jesus Rangel-Magdaleno, R. de Jesus Romero-Troncoso, R. A. Osornio-Rios, E. Cabal-Yepez, and L. M. Contreras-Medina, "Novel methodology for online half-broken-bar detection on induction motors," *IEEE Trans. Instrum. Meas.*, vol. 58, no. 5, pp. 1690–1698, May 2009.
- [15] R. Min, C. Marques, O. Bang, and B. Ortega, "Moiré phase-shifted fiber Bragg gratings in polymer optical fibers," *Opt. Fiber Technol.*, vol. 41, pp. 78–81, Mar. 2018, doi: [10.1016/j.yofte.2018.01.003](https://doi.org/10.1016/j.yofte.2018.01.003).
- [16] H. P. Wang, L. Z. Jiang, and P. Xiang, "Improving the durability of the optical fiber sensor based on strain transfer analysis," *Opt. Fiber Technol.*, vol. 42, pp. 97–104, Nov. 2018.
- [17] C. Marques *et al.*, "Advances on polymer optical fiber gratings using a KrF pulsed laser system operating at 248 nm," *Fibers*, vol. 6, no. 1, p. 13, 2018, doi: [10.3390/fib6010013](https://doi.org/10.3390/fib6010013).
- [18] J. P. Bazzo, F. Mezzadri, E. V. da Silva, D. R. Pipa, C. Martelli, and J. C. C. da Silva, "Thermal imaging of hydroelectric generator stator using a DTS system," *IEEE Sensors J.*, vol. 15, no. 11, pp. 6689–6696, Nov. 2015, doi: [10.1109/JSEN.2015.2465862](https://doi.org/10.1109/JSEN.2015.2465862).
- [19] G. Bolognini and A. Hartog, "Raman-based fibre sensors: Trends and applications," *Opt. Fiber Technol.*, vol. 19, no. 6, pp. 678–688, Dec. 2013.
- [20] J. P. Bazzo, D. R. Pipa, C. Martelli, E. Vagner da Silva, and J. C. Cardozo da Silva, "Improving spatial resolution of Raman DTS using total variation deconvolution," *IEEE Sensors J.*, vol. 16, no. 11, pp. 4425–4430, Jun. 2016.
- [21] J. D. Pelegrin *et al.*, "Raman distributed temperature sensing for end winding of high-power generator," *IET Optoelectron.*, vol. 14, no. 6, pp. 343–349, Dec. 2020, doi: [10.1049/iet-opt.2020.0037](https://doi.org/10.1049/iet-opt.2020.0037).
- [22] J. Jin, H. Zhang, J. Liu, and Y. Li, "Distributed temperature sensing based on Rayleigh scattering in irradiated optical fiber," *IEEE Sensors J.*, vol. 16, no. 24, pp. 8928–8935, Dec. 2016, doi: [10.1109/jsen.2016.2615945](https://doi.org/10.1109/jsen.2016.2615945).
- [23] J. S. Cherukupalli and G. Anders, "Distributed fiber optic temperature sensing," in *Proc. Distrib. Fiber Optic Sens. Dyn. Rating Power Cables*, Jun. 2020, pp. 26–31.
- [24] T. Blume, S. Krause, K. Meinikmann, and J. Lewandowski, "Upscaling lacustrine groundwater discharge rates by fiber-optic distributed temperature sensing," *Water Resour. Res.*, vol. 49, no. 12, pp. 7929–7944, 2013.
- [25] L. C. B. D. Silva, M. J. Pontes, and M. E. V. Segatto, "Analysis of parameters for a distributed temperature sensing based on Raman scattering," *J. Microw., Optoelectron. Electromagn. Appl.*, vol. 16, no. 1, pp. 259–272, Mar. 2017, doi: [10.1590/2179-10742017v16i1886](https://doi.org/10.1590/2179-10742017v16i1886).
- [26] D. Di Francesca *et al.*, "Radiation hardened architecture of a single-ended Raman-based distributed temperature sensor," *IEEE Trans. Nucl. Sci.*, vol. 64, no. 1, pp. 54–60, Jan. 2017, doi: [10.1109/TNS.2016.2631539](https://doi.org/10.1109/TNS.2016.2631539).
- [27] M. B. Hausner, F. Suárez, K. Glander, N. van de Giesen, J. S. Selker, and S. W. Tyler, "Calibrating single-ended fiber-optic Raman spectra distributed temperature sensing data," *Sensors*, vol. 11, no. 11, pp. 10859–10879, 2011.
- [28] A. O. Chernutsky *et al.*, "High-spatial-resolution distributed temperature sensing system based on a mode-locked fiber laser," in *Proc. Int. Conf. Laser Opt. (ICLO)*, St. Petersburg, Russia, Nov. 2020, p. 1, doi: [10.1109/ICLO48556.2020.9285857](https://doi.org/10.1109/ICLO48556.2020.9285857).
- [29] S. D. Dyer, M. G. Tanner, B. Baek, R. H. Hadfield, and S. W. Nam, "Analysis of a distributed fiber-optic temperature sensor using single-photon detectors," *Opt. Exp.*, vol. 20, no. 4, pp. 3456–3466, 2012.
- [30] Y. Chen *et al.*, "A fast high-spatial-resolution Raman distributed temperature sensor," *Proc. SPIE*, vol. 9157, Jun. 2014, Art. no. 91575M, doi: [10.1117/12.2058109](https://doi.org/10.1117/12.2058109).
- [31] I. A. Ershov, O. V. Stukach, N. V. Myasnikova, I. B. Tsydenzhapov, and I. V. Sychev, "The resolution enhancement in the distributed temperature sensor with the extremal filtration method," in *Proc. Dyn. Syst., Mech. Mach. (Dynamics)*, Omsk, Russia, Nov. 2020, pp. 1–3, doi: [10.1109/Dynamics50954.2020.9306163](https://doi.org/10.1109/Dynamics50954.2020.9306163).
- [32] G. Yilmaz and S. E. Karlik, "A distributed optical fiber sensor for temperature detection in power cables," *Sens. Actuators A, Phys.*, vol. 125, no. 2, pp. 148–155, Jan. 2006.
- [33] E. C. Quispe, X. M. Lopez-Fernandez, A. M. S. Mendes, A. J. Marques Cardoso, and J. A. Palacios, "Experimental study of the effect of positive sequence voltage on the derating of induction motors under voltage unbalance," in *Proc. IEEE Int. Electric Mach. Drives Conf. (IEMDC)*, Niagara Falls, ON, Canada, May 2011, pp. 908–912, doi: [10.1109/IEMDC.2011.5994936](https://doi.org/10.1109/IEMDC.2011.5994936).
- [34] G. Donner, B. K. Oakes, and S. T. Evon, "Motor primer. III," *IEEE Trans. Ind. Appl.*, vol. 39, no. 5, pp. 1467–1474, Sep. 2003, doi: [10.1109/TIA.2003.816557](https://doi.org/10.1109/TIA.2003.816557).
- [35] *ANSI/NEMA, Motors and Generators*, Standard MG1-2003, 2004.
- [36] *IEEE Guide for AC Motor Protection*, IEEE Standard C37.96-2012 (Revision IEEE Standard C37.96-2000), vols. 1–160, Feb. 2013.
- [37] Z. Dong, Y. Yu, W. Li, B. Wang, and D. Xu, "Flux-weakening control for induction motor in voltage extension region: Torque analysis and dynamic performance improvement," *IEEE Trans. Ind. Electron.*, vol. 65, no. 5, pp. 3740–3751, May 2018, doi: [10.1109/TIE.2017.2764853](https://doi.org/10.1109/TIE.2017.2764853).

## 6 CONCLUSION

### 6.1 General Conclusions

This thesis presented the monitoring of dynamic deformation and temperature in rotating electrical machines using optical sensors. The monitoring techniques used the photorefractive optical FBG sensors integrated into CFRP and DTS sensors. Given the importance of rotating electrical machines in Industry 4.0, the sensors and methods proposed in this thesis offer promising alternatives. Compared to conventional sensing techniques, the main advantages of the fiber-optic sensors include immunity to electromagnetic interference, the use of only one optical cable as a sensor, reduced size, resistance to high temperatures, and robustness because of CFRP encapsulation. The experimental results performed in a 20 hp three-phase induction motor and the bar of a 355 kW hydroelectric generator instrumented in the laboratory have demonstrated the potential of optical sensors in monitoring the state of electrical machines.

The use of optical sensors to identify failures in electrical machines proved to be relevant in preventing damage that could compromise the performance and integrity of the machine. Conventional sensors such as RTDs, accelerometers, and piezoelectrics are complex to install, prone to electromagnetic interference, and punctual. These sensors are limited to the peripheral measurements of the installation point. By contrast, a DTS system has been shown to have many sensors embedded in a single optical cable, thus simplifying installation. Similar to DTS sensors, FBG sensors are immune to electromagnetic interference, a fundamental factor in the measurement of electrical machines. In addition, the thesis has outlined that the size of the optical sensors allows its installation close to the element under examination without interfering with the machine structure.

In terms of innovation, the first paper has presented a device to simultaneously measure vibration, temperature, and rotating magnetic field, resulting in a utility model application (INPI: BR 20 2020 001730 1). This sensor is adaptable to several machine designs because it can be constructed in any radial dimension and is only 2 mm thick. Its installation is intrinsic to the electrical machine, and the reading of several FBG sensors embedded in a single optical cable allows dynamic and safe monitoring. Because the sensor structure is fixed to the core, it must be installed before inserting the coils constitute the stator to ensure greater sensitivity. Despite this challenge, the results obtained during the experimental tests demonstrate the robustness and measurement sensitivity of FBG sensors encapsulated in CFRP.

Similarly, the second paper outlined a CFRP-encapsulated FBG sensor to monitor bearings. Owing to the difficulty in installing stator sensors, the newly developed sensor was installed next to the bearing without rewinding the machine. One of the highlights of this sensor is its direct contact with the bearing without damaging its measurement capacity and altering the integrity of the machine. Thus, the sensor can detect a failure in any element that constitutes the bearing at an early stage. In the analysis of the good and damaged bearings, the sensor detects faults in

the bearing elements. The paper demonstrated that the measurements remain the same despite several bearing changes and numerous tests. Therefore, it can be concluded that the bearing sensor exhibits good repeatability and reproducibility. Compared with existing sensors in the market, this sensor offers all the positive characteristics of optical sensors, particularly the reduced size and immunity to electromagnetic interference. Another critical factor is the possibility of applying this sensor to any system with bearings, for example, in a line of paper dryer cylinders, where all the bearings can be monitored simultaneously, with dynamic data in real-time, allowing reliability of the system.

Regarding the instrumentation of the stator bar of a hydroelectric generator in the laboratory, the thesis described a practical and safe way to install sensors in generators in operation. Thus, the fiber was installed longitudinally at the end of the bar, a region located outside the stator, known as the head of the coils. Because the DTS sensor has a spatial resolution of 1 m, a high-resolution signal reconstruction algorithm was used to measure the temperature in sections up to 15 cm in length. Compared with conventional sensors, the proposed method has advantages such as immunity to electromagnetic interference, reduced dimensions, and a single sensor element. The experimental results obtained in the stator bar of the generator have demonstrated the possibility of using this sensor for monitoring the temperature variation at the heads of the coils for the extraction of the maximum power without harming the insulation of the system.

Moreover, the thesis outlined a DTS sensor used to instrument a 20 hp TIM stator. Optical fiber was installed between the stator core and coils in all slots. Temperature monitoring in motors is typically spot-on, and a conventional sensor is mounted between two coils or in a slot, limiting the temperature measurement to a small region. With the distributed sensor, the entire internal region of the motor stator was monitored. The experimental results show an improvement of 60 % in the original signal measured by the RDTS when processed through the high-resolution signal reconstruction algorithm. This instrumentation is advantageous in the integrated monitoring of the internal region of the TIM. These data can reproduce three-dimensional images of the machine, allowing instantaneous monitoring of the temperature distribution, making it possible to identify anomalies, including voltage imbalance in the supply.

Tests performed on electrical machines have electromagnetic influences and are susceptible to the induction and circulation of electrical currents through the housing. Because optical fiber is an insulating material, there is no risk of damage to the measuring equipment. Another essential feature is the reduced fiber size, which made it possible to implement the sensors without changing the machine's constructive characteristics. In cases of significant mechanical stress, encapsulation with CFRP is essential to provide robustness while maintaining the sensitivity of the FBG sensors. In addition, the sensors are adaptable to different formats to facilitate and speed up their installation. Thus, this thesis demonstrates the effectiveness of implementing optical sensors in electrical machinery and offers techniques for preventive maintenance to ensure extended operational life.

## 6.2 SUGGESTIONS FOR FUTURE WORKS

The techniques developed and the results obtained in this study suggest avenues for further research. New tests for diagnosing different defects, such as eccentricity, broken rotor bar, and phase imbalance, can be performed using the sensor coupled to the TIM stator. Individual analysis of FBG sensors and examination of the pattern of the rotating magnetic field are also suggested, where different failure situations can be analyzed. Other encapsulation materials can be tested, such as fiberglass, to integrate the optical fiber for mechanical protection while maintaining the sensor characteristics. The sensor can also be built and implemented in to monitor the performance of machines of different sizes.

For bearing sensors, new materials can be tested in a package such as a stator sensor. The results can be processed using new conversion techniques, filters, or artificial intelligence to identify measured frequency components in isolation. Through neural networks, the signals measured by FBG sensors can be processed to classify and recognize faults, as shown in (YONG *et al.*, 2020).

In the case of distributed temperature sensors, an improvement in the signal reconstruction algorithm yielding satisfactory results for up to 15 cm can be suggested. Other techniques can be used to reduce the spatial resolution, thereby increasing the number of sensors. For the hydroelectric generator bar with a higher measurement number, the installation configuration can be radial; therefore, there would be a more accurate measurement of the temperature. Owing to the galvanic isolation of the optical fiber, it can be implemented in the lower region of the insulation; thus, the temperature would be relative to the copper bar. In the thermal mapping of TIM, a dedicated algorithm or software can be developed to monitor the temperature instantly with overheating alerts in the case of defects. The supervision of electrical machines is fundamental in identifying faults, especially in the case of internal quantities that are difficult to access.

## REFERÊNCIAS

- AHMADI, M.; POSHTAN, J.; POSHTAN, M. Static eccentricity fault detection in induction motors using wavelet packet decomposition and gyration radius. In: **2013 1st International Conference on Communications, Signal Processing, and their Applications (ICCSPA)**. [S.l.: s.n.], 2013. p. 1–5.
- ANEEL, A. N. D. E. E. **Aneel estimula troca de motores elétricos para promover eficiência energética**. 2015. Portal da ANEEL. Disponível em: <http://www.aneel.gov.br>.
- ANEEL, A. N. D. E. E. **Banco de Informações de Geração**. 2020. Portal da ANEEL. Disponível em: <https://www2.aneel.gov.br/aplicacoes/capacidadebrasil/capacidadebrasil.cfm>.
- AZGOMI, H. F.; POSHTAN, J. Induction motor stator fault detection via fuzzy logic. In: **2013 21st Iranian Conference on Electrical Engineering (ICEE)**. [S.l.: s.n.], 2013. p. 1–5.
- BAZAN, G. H. *et al.* Stator short-circuit diagnosis in induction motors using mutual information and intelligent systems. **IEEE Transactions on Industrial Electronics**, v. 66, n. 4, p. 3237–3246, 2019.
- BAZZO, J. P. *et al.* Thermal imaging of hydroelectric generator stator using a dts system. **IEEE Sensors Journal**, v. 15, n. 11, p. 6689–6696, 2015.
- BAZZO J. P.; PIPA, D. R. M. C. S. E. V. S. J. C. C. Improving spatial resolution of raman dts using total variation deconvolution. **IEEE Sensors Journal**, v. 16, n. 11, p. 4425–4430, 2016.
- BESSOUS, N. *et al.* New vision about the overlap frequencies in the mcsa-fft technique to diagnose the eccentricity fault in the induction motors. In: **2017 5th International Conference on Electrical Engineering - Boumerdes (ICEE-B)**. [S.l.: s.n.], 2017. p. 1–6.
- BOLOGNINI, G. H. Raman-based fibre sensors: Trends and applications. **Optical Fiber Technology**, v. 19, p. 687–688, 2013.
- CEBAN, A.; PUSCA, R.; ROMARY, R. Study of rotor faults in induction motors using external magnetic field analysis. **IEEE Transactions on Industrial Electronics**, v. 59, n. 5, p. 2082–2093, 2012.
- CHANG, C.; HONG, J.; CHANG, W. Preventive maintenance of motors and automatic classification of defects using artificial intelligence. In: **14th International Conference on Mechatronic and Embedded Systems and Applications (MESA)**. [S.l.]: IEEE/ASME, 2018. p. 1–6.
- DALVAND, F. *et al.* Time-domain bearing condition monitoring in induction motors using instantaneous frequency of motor voltage. In: **2014 Smart Grid Conference (SGC)**. [S.l.: s.n.], 2014. p. 1–7.
- DEHINA, W. *et al.* Diagnosis and comparison between stator current analysis and vibration analysis of static eccentricity faults in the induction motor. In: **2019 4th International Conference on Power Electronics and their Applications (ICPEA)**. [S.l.: s.n.], 2019. p. 1–4.
- DEVI, N. R.; SARMA, D. V. S. S. S.; RAO, P. V. R. Diagnosis and classification of stator winding insulation faults on a three-phase induction motor using wavelet and mnn. **IEEE Transactions on Dielectrics and Electrical Insulation**, v. 23, n. 5, p. 2543–2555, 2016.

EFTEKHARI, M. *et al.* Online detection of induction motor's stator winding short-circuit faults. **IEEE Systems Journal**, v. 8, n. 4, p. 1272–1282, 2014.

EICKHOFF, W.; ULRICH, R. Optical frequency domain reflectometry in single-mode fiber. **Applied Physics Letters**, v. 39, n. 9, p. 693–695, 1981. Disponível em: <https://doi.org/10.1063/1.92872>.

EPE. **Resenha Mensal apresenta crescimento de 3,5% em relação ao mês de novembro de 2018**. 2019. Empresa de Pesquisa Energética. Disponível em: <http://www.epe.gov.br/pt/imprensa/noticias/resenha-mensal-apresenta-crescimento-de-3-5-em-relacao-ao-mes-de-novembro-de-2018>,.

EPE. **Consumo Mensal de Energia Elétrica por Classe (regiões e subsistemas)**. 2020. Empresa de Pesquisa Energética. Disponível em: <http://www.epe.gov.br/pt/publicacoes-dados-abertos/publicacoes/Consumo-mensal-de-energia-eletrica-por-classe-regioes-e-subsistemas>,.

FROSINI, L.; BASSI, E. Stator current and motor efficiency as indicators for different types of bearing faults in induction motors. **IEEE Transactions on Industrial Electronics**, v. 57, n. 1, p. 244–251, 2010.

GALVAO, J. R. *et al.* Smart carbon fiber transtibial prosthesis based on embedded fiber bragg gratings. **IEEE Sensors Journal**, v. 18, n. 4, p. 1520–1527, 2018.

GRUBIC, S. *et al.* A survey on testing and monitoring methods for stator insulation systems of low-voltage induction machines focusing on turn insulation problems. **IEEE Transactions on Industrial Electronics**, v. 55, n. 12, p. 4127–4136, 2008.

HAN Q.AND DING, Z. X. X. W. T. C. F. Stator current model for detecting rolling bearing faults in induction motors using magnetic equivalent circuits. **ELSEVIER, Mechanical Systems and Signal Processing**, v. 131, p. 554–575, 2019.

HU, C. *et al.* Application research of distributed optical fiber temperature sensor in power system. In: **2011 Asia Communications and Photonics Conference and Exhibition (ACP)**. [S.l.: s.n.], 2011. p. 1–6.

HUDON, C. *et al.* Determination of stator temperature profile using distributed sensing. In: **2013 IEEE Electrical Insulation Conference (EIC)**. [S.l.: s.n.], 2013. p. 191–195.

IEC, S. **Rotating Electrical Machines, Part 1: Rating and Performance**. 12. ed. [S.l.]: IEC-60034-1, 2010.

IEEE. Recommended practice for the design of reliable industrial and commercial power systems. **IEEE Std P493/D4**, 2006.

IMMOVILLI, F. *et al.* Bearing fault model for induction motor with externally induced vibration. **IEEE Transactions on Industrial Electronics**, v. 60, n. 8, p. 3408–3418, 2013.

IMMOVILLI, F. *et al.* Detection of generalized-roughness bearing fault by spectral-kurtosis energy of vibration or current signals. **IEEE Transactions on Industrial Electronics**, v. 56, n. 11, p. 4710–4717, 2009.

JANDA, M.; MAKKI, Z.; KONICEK, P. Calculation of the vibration induction motor using the finite element method. In: **Proceedings of the 16th International Conference on Mechatronics - Mechatronika 2014**. [S.l.: s.n.], 2014. p. 526–529.

- JOKIC, S.; CINCAR, N.; NOVAKOVIC, B. The analysis of vibration measurement and current signature in motor drive faults detection. In: **2018 17th International Symposium INFOTEH-JAHORINA (INFOTEH)**. [S.l.: s.n.], 2018. p. 1–6.
- KANOVIĆ, *et al.* Induction motor broken rotor bar detection using vibration analysis — a case study. In: **2013 9th IEEE International Symposium on Diagnostics for Electric Machines, Power Electronics and Drives (SDEMPED)**. [S.l.: s.n.], 2013. p. 64–68.
- KERSEY, A. D. Optical fiber sensors for permanent downwell monitoring applications in the oil and gas industry. **JIEICE Trans. Electron**, E83-C, n. 3, p. 400–404, 2000.
- KIM, D. *et al.* Estimation of acoustic noise and vibration in an induction machine considering rotor eccentricity. **IEEE Transactions on Magnetics**, v. 50, n. 2, p. 857–860, 2014.
- KOKKO, V. I. J. Ageing due to thermal cycling by power regulation cycles in lifetime estimation of hydroelectric generator stator windings. In: **2012 XXth International Conference on Electrical Machines**. [S.l.: s.n.], 2012. p. 1559–1564.
- Kumar, T. C. A.; Singh, G.; Naikan, V. N. A. Sensitivity of rotor slot harmonics due to inter-turn fault in induction motors through vibration analysis. In: **2018 International Conference on Power, Instrumentation, Control and Computing (PICC)**. [S.l.: s.n.], 2018. p. 1–3.
- LEE, J. *et al.* Prognostics and health management design for rotary machinery systems—reviews, methodology and applications. **Mechanical Systems and Signal Processing**, v. 42, n. 1, p. 314 – 334, 2014. ISSN 0888-3270.
- LEE, S. B. *et al.* Identification of false rotor fault indications produced by online mcsa for medium-voltage induction machines. **IEEE Transactions on Industry Applications**, v. 52, n. 1, p. 729–739, 2016.
- LINESSIO, R. P. *et al.* Induction motors vibration monitoring using a biaxial optical fiber accelerometer. **IEEE Sensors Journal**, v. 16, n. 22, p. 8075–8082, 2016.
- LIU, L. *et al.* Temperature-independent fbg pressure sensor with high sensitivity. **Optical Fiber Technology**, v. 13, n. 1, p. 78–80, 2007.
- LU, S. *et al.* In situ motor fault diagnosis using enhanced convolutional neural network in an embedded system. **IEEE Sensors Journal**, v. 20, n. 15, p. 8287–8296, 2020.
- MIRZAEVA, G.; SAAD, K. I. Advanced diagnosis of stator turn-to-turn faults and static eccentricity in induction motors based on internal flux measurement. **IEEE Transactions on Industry Applications**, v. 54, n. 4, p. 3961–3970, 2018.
- MOHAMMED, A.; DJUROVIĆ, S. Stator winding internal thermal monitoring and analysis using in situ fbg sensing technology. **IEEE Transactions on Energy Conversion**, v. 33, n. 3, p. 1508–1518, 2018.
- MOHAMMED, A.; MELECIO, J. I.; DJUROVIĆ, S. Open-circuit fault detection in stranded pmsm windings using embedded fbg thermal sensors. **IEEE Sensors Journal**, v. 19, n. 9, p. 3358–3367, 2019.
- NEMEC, M. *et al.* Detection of broken bars in induction motor through the analysis of supply voltage modulation. **IEEE Transactions on Industrial Electronics**, v. 57, n. 8, p. 2879–2888, 2010.
- NSK, B. D. **MDiagnóstico Rápido de Ocorrências em Rolamentos**. 2019. NSK. Disponível em: <http://www.nsk.com.br/upload/file/B08.pdf>.

ORHAN, S.; AKTÜRK, N.; ÇELİK, V. Vibration monitoring for defect diagnosis of rolling element bearings as a predictive maintenance tool: Comprehensive case studies. **E International 39 - ELSEVIER.**, p. 293–298, 2006.

PALACIOS, R. H. C. *et al.* Time domain diagnosis of multiple faults in three phase induction motors using intelligent approaches. In: **2017 IEEE 11th International Symposium on Diagnostics for Electrical Machines, Power Electronics and Drives (SDEMPED)**. [S.l.: s.n.], 2017. p. 85–89.

PAWLUS, W.; KHANG, H. V.; HANSEN, M. R. Temperature rise estimation of induction motor drives based on loadability curves to facilitate design of electric powertrains. **IEEE Transactions on Industrial Informatics**, v. 13, n. 3, p. 985–994, 2017.

PRIETO, M. D. *et al.* Bearing fault detection by a novel condition-monitoring scheme based on statistical-time features and neural networks. **IEEE Transactions on Industrial Electronics**, v. 60, n. 8, p. 3398–3407, 2013.

RANSOM, D. L.; HAMILTON, R. Extending motor life with updated thermal model overload protection. In: **2011 IEEE Industry Applications Society Annual Meeting**. [S.l.: s.n.], 2011. p. 1–8.

RAO, S. **Mechanical Vibrations**. 4. ed. [S.l.]: Pearson, 2008. ISBN 978.85.7605.200.5.

RATHNAYAKA, S. B.; SEE, K. Y. Early detection of induction motor's defects using an inductively coupled impedance extraction method. In: **2017 IEEE International Electric Machines and Drives Conference (IEMDC)**. [S.l.: s.n.], 2017. p. 1–6.

RESENDIZ-OCHOA, E. *et al.* Induction motor failure analysis: An automatic methodology based on infrared imaging. **IEEE Access**, v. 6, p. 76993–77003, 2018.

RILEY, C. M. *et al.* Stator current harmonics and their causal vibrations: a preliminary investigation of sensorless vibration monitoring applications. **IEEE Transactions on Industry Applications**, v. 35, n. 1, p. 94–99, 1999.

SARKAR, S. *et al.* Machine learning methods for discriminating strain and temperature effects on fbg-based sensors. **IEEE Photonics Technology Letters**, v. 33, n. 16, p. 876–879, 2021.

SAXENA, M. K. *et al.* Raman optical fiber distributed temperature sensor using wavelet transform based simplified signal processing of raman backscattered signals. **Optics & Laser Technology**, v. 65, p. 14–24, 2015.

SEERA, M. *et al.* Condition monitoring of induction motors: A review and an application of an ensemble of hybrid intelligent models. **Expert Systems with Applications**, v. 41, n. 10, p. 4891–4903, 2014. ISSN 0957-4174.

SOLEIMANI, Y.; CRUZ, S. M. A.; HAGHJOO, F. Broken rotor bar detection in induction motors based on air-gap rotational magnetic field measurement. **IEEE Transactions on Instrumentation and Measurement**, v. 68, n. 8, p. 2916–2925, 2019.

SOUSA, K. d. M. *et al.* Determination of temperature dynamics and mechanical and stator losses relationships in a three-phase induction motor using fiber bragg grating sensors. **IEEE Sensors Journal**, v. 12, n. 10, p. 3054–3061, 2012.

SOUSA, K. M. *et al.* Dynamic eccentricity induced in induction motor detected by optical fiber bragg grating strain sensors. **IEEE Sensors Journal**, v. 16, n. 12, p. 4786–4792, 2016.

- THEUNE, N. M. *et al.* Investigation of stator coil and lead temperatures on high voltage inside large power generators via use of fiber bragg gratings. In: **SENSORS, 2002 IEEE**. [S.l.: s.n.], 2002. v. 2, p. 1603–1607 vol.2.
- TREML, A. E. *et al.* Broken rotor bar fault detection in asynchronous machines using vibration analysis. In: **2019 IEEE Power Energy Society General Meeting (PESGM)**. [S.l.: s.n.], 2019. p. 1–5.
- TSYPKIN, M. Induction motor condition monitoring: Vibration analysis technique — diagnosis of electromagnetic anomalies. In: **2017 IEEE AUTOTESTCON**. [S.l.: s.n.], 2017. p. 1–7.
- TWERDOCHLIB, M.; EMERY, F. T.; BRANDT, G. B. Improved temperature sensors for large generators: Final report. 4 1989. Disponível em: <https://www.osti.gov/biblio/6127601>.
- WANG, C. *et al.* Reliable leak detection in pipelines using integrated ddts temperature and das acoustic fiber-optic sensor. In: **2018 International Carnahan Conference on Security Technology (ICCST)**. [S.l.: s.n.], 2018. p. 1–5.
- WEG. 2019. Guia de especificações - motores elétricos. Disponível em: <https://static.weg.net/medias/downloadcenter/h32/hc5/WEG-motores-eletricos-guia-de-especificacao-50032749-brochure-portuguese-web.pdf>.
- XU, C.; QIU, C.; WU, X. Eccentricity faults diagnosis based on motor stray magnetic field signature analysis. In: **2017 Chinese Automation Congress (CAC)**. [S.l.: s.n.], 2017. p. 5577–5582.
- YAN, R. *et al.* Guest editorial special issue on smart sensing and artificial intelligence-enabled data analytics for health monitoring of engineering systems. **IEEE Sensors Journal**, v. 20, n. 15, p. 8203–8203, 2020.
- YONG, C. *et al.* Detection method using fbg sensing signal to diagnose rolling bearing fault. **Chinese Journal of Lasers**, v. 47, n. 11, p. 1104004, 11 2020. Disponível em: <https://www.researching.cn/articles/OJ569881750e2bb499>.
- ZHANG, H. Online thermal monitoring models for induction machines. **IEEE Transactions on Energy Conversion**, v. 30, n. 4, p. 1279–1287, 2015.
- ZHANG, P. *et al.* A survey of condition monitoring and protection methods for medium-voltage induction motors. **IEEE Transactions on Industry Applications**, v. 47, n. 1, p. 34–46, 2011.
- ZHANG, S. *et al.* Model-based analysis and quantification of bearing faults in induction machines. **IEEE Transactions on Industry Applications**, v. 56, n. 3, p. 2158–2170, 2020.
- ZHU, P. *et al.* Distributed modular temperature-strain sensor based on optical fiber embedded in laminated composites. **Composites Part B: Engineering**, v. 168, p. 267 – 273, 2019. ISSN 1359-8368. Disponível em: <http://www.sciencedirect.com/science/article/pii/S1359836818330440>.

**ANEXO A – Authorization of Journals for the Availability of Articles**



## Optical Fiber Sensor Encapsulated in Carbon Fiber Reinforced Polymer for Fault Detection in Rotating Electrical Machines

Author: Jessé de Pelegrin

Publication: IEEE Sensors Journal

Publisher: IEEE

Date: 1 Oct.1, 2020

Copyright © 2020, IEEE

### Thesis / Dissertation Reuse

The IEEE does not require individuals working on a thesis to obtain a formal reuse license, however, you may print out this statement to be used as a permission grant:

*Requirements to be followed when using any portion (e.g., figure, graph, table, or textual material) of an IEEE copyrighted paper in a thesis:*

- 1) In the case of textual material (e.g., using short quotes or referring to the work within these papers) users must give full credit to the original source (author, paper, publication) followed by the IEEE copyright line © 2011 IEEE.
- 2) In the case of illustrations or tabular material, we require that the copyright line © [Year of original publication] IEEE appear prominently with each reprinted figure and/or table.
- 3) If a substantial portion of the original paper is to be used, and if you are not the senior author, also obtain the senior author's approval.

*Requirements to be followed when using an entire IEEE copyrighted paper in a thesis:*

- 1) The following IEEE copyright/ credit notice should be placed prominently in the references: © [year of original publication] IEEE. Reprinted, with permission, from [author names, paper title, IEEE publication title, and month/year of publication]
- 2) Only the accepted version of an IEEE copyrighted paper can be used when posting the paper or your thesis online.
- 3) In placing the thesis on the author's university website, please display the following message in a prominent place on the website: In reference to IEEE copyrighted material which is used with permission in this thesis, the IEEE does not endorse any of [university/educational entity's name goes here]'s products or services. Internal or personal use of this material is permitted. If interested in reprinting/republishing IEEE copyrighted material for advertising or promotional purposes or for creating new collective works for resale or redistribution, please go to [http://www.ieee.org/publications\\_standards/publications/rights/rights\\_link.html](http://www.ieee.org/publications_standards/publications/rights/rights_link.html) to learn how to obtain a License from RightsLink.

If applicable, University Microfilms and/or ProQuest Library, or the Archives of Canada may supply single copies of the dissertation.

BACK

CLOSE WINDOW



## Smart Carbon-Fiber Reinforced Polymer Optical Fiber Bragg Grating for Monitoring Fault Detection in Bearing

Author: Jessé De Pelegrin

Publication: IEEE Sensors Journal

Publisher: IEEE

Date: Dec 31, 1969

Copyright © 1969, IEEE

### Thesis / Dissertation Reuse

The IEEE does not require individuals working on a thesis to obtain a formal reuse license, however, you may print out this statement to be used as a permission grant:

*Requirements to be followed when using any portion (e.g., figure, graph, table, or textual material) of an IEEE copyrighted paper in a thesis:*

- 1) In the case of textual material (e.g., using short quotes or referring to the work within these papers) users must give full credit to the original source (author, paper, publication) followed by the IEEE copyright line © 2011 IEEE.
- 2) In the case of illustrations or tabular material, we require that the copyright line © [Year of original publication] IEEE appear prominently with each reprinted figure and/or table.
- 3) If a substantial portion of the original paper is to be used, and if you are not the senior author, also obtain the senior author's approval.

*Requirements to be followed when using an entire IEEE copyrighted paper in a thesis:*

- 1) The following IEEE copyright/ credit notice should be placed prominently in the references: © [year of original publication] IEEE. Reprinted, with permission, from [author names, paper title, IEEE publication title, and month/year of publication]
- 2) Only the accepted version of an IEEE copyrighted paper can be used when posting the paper or your thesis online.
- 3) In placing the thesis on the author's university website, please display the following message in a prominent place on the website: In reference to IEEE copyrighted material which is used with permission in this thesis, the IEEE does not endorse any of [university/educational entity's name goes here]'s products or services. Internal or personal use of this material is permitted. If interested in reprinting/republishing IEEE copyrighted material for advertising or promotional purposes or for creating new collective works for resale or redistribution, please go to [http://www.ieee.org/publications\\_standards/publications/rights/rights\\_link.html](http://www.ieee.org/publications_standards/publications/rights/rights_link.html) to learn how to obtain a License from RightsLink.

If applicable, University Microfilms and/or ProQuest Library, or the Archives of Canada may supply single copies of the dissertation.

BACK

CLOSE WINDOW

## JOHN WILEY AND SONS LICENSE TERMS AND CONDITIONS

Mar 12, 2022

---

---

This Agreement between Prof. Jessé de Pelegrin ("You") and John Wiley and Sons ("John Wiley and Sons") consists of your license details and the terms and conditions provided by John Wiley and Sons and Copyright Clearance Center.

License Number 5263900785770

License date Mar 07, 2022

Licensed Content Publisher John Wiley and Sons

Licensed Content Publication IET Optoelectronics

Licensed Content Title Raman distributed temperature sensing for end winding of high-power generator

Licensed Content Author Jean Carlos Cardozo da Silva, Erlon Vagner da Silva, Daniel Rodrigues Pipa, et al

Licensed Content Date Dec 1, 2020

Licensed Content Volume 14

Licensed Content Issue 6

Licensed Content Pages 7

Type of use      Dissertation/Thesis

Requestor type    Author of this Wiley article

Format            Electronic

Portion            Full article

Will you be  
translating?      No

Title                ANÁLISE E DESENVOLVIMENTO DE TÉCNICAS DE  
INSTRUMENTAÇÃO ÓTICA APLICADA EM MÁQUINAS  
ELÉTRICAS

Institution  
name                UTFPR

Expected  
presentation  
date                May 2022

Order reference  
number            1

Prof. Jessé de Pelegrin  
Rua Francisco Guilherme Dorl, 81

Requestor  
Location            Joaçaba, Santa Catarina 89600000  
Brazil  
Attn: Prof. Jessé de Pelegrin

Publisher Tax  
ID                    EU826007151

Total                0.00 USD

Terms and Conditions

### TERMS AND CONDITIONS

This copyrighted material is owned by or exclusively licensed to John Wiley & Sons, Inc. or one of its group companies (each a "Wiley Company") or handled on behalf of a society with which a Wiley Company has exclusive publishing rights in relation to a particular work

(collectively "WILEY"). By clicking "accept" in connection with completing this licensing transaction, you agree that the following terms and conditions apply to this transaction (along with the billing and payment terms and conditions established by the Copyright Clearance Center Inc., ("CCC's Billing and Payment terms and conditions"), at the time that you opened your RightsLink account (these are available at any time at <http://myaccount.copyright.com>).

## Terms and Conditions

- The materials you have requested permission to reproduce or reuse (the "Wiley Materials") are protected by copyright.
- You are hereby granted a personal, non-exclusive, non-sub licensable (on a stand-alone basis), non-transferable, worldwide, limited license to reproduce the Wiley Materials for the purpose specified in the licensing process. This license, **and any CONTENT (PDF or image file) purchased as part of your order**, is for a one-time use only and limited to any maximum distribution number specified in the license. The first instance of republication or reuse granted by this license must be completed within two years of the date of the grant of this license (although copies prepared before the end date may be distributed thereafter). The Wiley Materials shall not be used in any other manner or for any other purpose, beyond what is granted in the license. Permission is granted subject to an appropriate acknowledgement given to the author, title of the material/book/journal and the publisher. You shall also duplicate the copyright notice that appears in the Wiley publication in your use of the Wiley Material. Permission is also granted on the understanding that nowhere in the text is a previously published source acknowledged for all or part of this Wiley Material. Any third party content is expressly excluded from this permission.
- With respect to the Wiley Materials, all rights are reserved. Except as expressly granted by the terms of the license, no part of the Wiley Materials may be copied, modified, adapted (except for minor reformatting required by the new Publication), translated, reproduced, transferred or distributed, in any form or by any means, and no derivative works may be made based on the Wiley Materials without the prior permission of the respective copyright owner. **For STM Signatory Publishers clearing permission under the terms of the [STM Permissions Guidelines](#) only, the terms of the license are extended to include subsequent editions and for editions in other languages, provided such editions are for the work as a whole in situ and does not involve the separate exploitation of the permitted figures or extracts**, You may not alter, remove or suppress in any manner any copyright, trademark or other notices displayed by the Wiley Materials. You may not license, rent, sell, loan, lease, pledge, offer as security, transfer or assign the Wiley Materials on a stand-alone basis, or any of the rights granted to you hereunder to any other person.
- The Wiley Materials and all of the intellectual property rights therein shall at all times remain the exclusive property of John Wiley & Sons Inc, the Wiley Companies, or their respective licensors, and your interest therein is only that of having possession of and the right to reproduce the Wiley Materials pursuant to Section 2 herein during the continuance of this Agreement. You agree that you own no right, title or interest in or to the Wiley Materials or any of the intellectual property rights therein. You shall have no rights hereunder other than the license as provided for above in Section 2. No right, license or interest to any trademark, trade name, service mark or other branding ("Marks") of WILEY or its licensors is granted hereunder, and you agree that you shall not assert any such right, license or interest with respect thereto
- NEITHER WILEY NOR ITS LICENSORS MAKES ANY WARRANTY OR REPRESENTATION OF ANY KIND TO YOU OR ANY THIRD PARTY, EXPRESS, IMPLIED OR STATUTORY, WITH RESPECT TO THE MATERIALS

OR THE ACCURACY OF ANY INFORMATION CONTAINED IN THE MATERIALS, INCLUDING, WITHOUT LIMITATION, ANY IMPLIED WARRANTY OF MERCHANTABILITY, ACCURACY, SATISFACTORY QUALITY, FITNESS FOR A PARTICULAR PURPOSE, USABILITY, INTEGRATION OR NON-INFRINGEMENT AND ALL SUCH WARRANTIES ARE HEREBY EXCLUDED BY WILEY AND ITS LICENSORS AND WAIVED BY YOU.

- WILEY shall have the right to terminate this Agreement immediately upon breach of this Agreement by you.
- You shall indemnify, defend and hold harmless WILEY, its Licensors and their respective directors, officers, agents and employees, from and against any actual or threatened claims, demands, causes of action or proceedings arising from any breach of this Agreement by you.
- IN NO EVENT SHALL WILEY OR ITS LICENSORS BE LIABLE TO YOU OR ANY OTHER PARTY OR ANY OTHER PERSON OR ENTITY FOR ANY SPECIAL, CONSEQUENTIAL, INCIDENTAL, INDIRECT, EXEMPLARY OR PUNITIVE DAMAGES, HOWEVER CAUSED, ARISING OUT OF OR IN CONNECTION WITH THE DOWNLOADING, PROVISIONING, VIEWING OR USE OF THE MATERIALS REGARDLESS OF THE FORM OF ACTION, WHETHER FOR BREACH OF CONTRACT, BREACH OF WARRANTY, TORT, NEGLIGENCE, INFRINGEMENT OR OTHERWISE (INCLUDING, WITHOUT LIMITATION, DAMAGES BASED ON LOSS OF PROFITS, DATA, FILES, USE, BUSINESS OPPORTUNITY OR CLAIMS OF THIRD PARTIES), AND WHETHER OR NOT THE PARTY HAS BEEN ADVISED OF THE POSSIBILITY OF SUCH DAMAGES. THIS LIMITATION SHALL APPLY NOTWITHSTANDING ANY FAILURE OF ESSENTIAL PURPOSE OF ANY LIMITED REMEDY PROVIDED HEREIN.
- Should any provision of this Agreement be held by a court of competent jurisdiction to be illegal, invalid, or unenforceable, that provision shall be deemed amended to achieve as nearly as possible the same economic effect as the original provision, and the legality, validity and enforceability of the remaining provisions of this Agreement shall not be affected or impaired thereby.
- The failure of either party to enforce any term or condition of this Agreement shall not constitute a waiver of either party's right to enforce each and every term and condition of this Agreement. No breach under this agreement shall be deemed waived or excused by either party unless such waiver or consent is in writing signed by the party granting such waiver or consent. The waiver by or consent of a party to a breach of any provision of this Agreement shall not operate or be construed as a waiver of or consent to any other or subsequent breach by such other party.
- This Agreement may not be assigned (including by operation of law or otherwise) by you without WILEY's prior written consent.
- Any fee required for this permission shall be non-refundable after thirty (30) days from receipt by the CCC.
- These terms and conditions together with CCC's Billing and Payment terms and conditions (which are incorporated herein) form the entire agreement between you and WILEY concerning this licensing transaction and (in the absence of fraud) supersedes all prior agreements and representations of the parties, oral or written. This Agreement may not be amended except in writing signed by both parties. This Agreement shall be binding upon and inure to the benefit of the parties' successors, legal representatives,

and authorized assigns.

- In the event of any conflict between your obligations established by these terms and conditions and those established by CCC's Billing and Payment terms and conditions, these terms and conditions shall prevail.
- WILEY expressly reserves all rights not specifically granted in the combination of (i) the license details provided by you and accepted in the course of this licensing transaction, (ii) these terms and conditions and (iii) CCC's Billing and Payment terms and conditions.
- This Agreement will be void if the Type of Use, Format, Circulation, or Requestor Type was misrepresented during the licensing process.
- This Agreement shall be governed by and construed in accordance with the laws of the State of New York, USA, without regards to such state's conflict of law rules. Any legal action, suit or proceeding arising out of or relating to these Terms and Conditions or the breach thereof shall be instituted in a court of competent jurisdiction in New York County in the State of New York in the United States of America and each party hereby consents and submits to the personal jurisdiction of such court, waives any objection to venue in such court and consents to service of process by registered or certified mail, return receipt requested, at the last known address of such party.

## WILEY OPEN ACCESS TERMS AND CONDITIONS

Wiley Publishes Open Access Articles in fully Open Access Journals and in Subscription journals offering Online Open. Although most of the fully Open Access journals publish open access articles under the terms of the Creative Commons Attribution (CC BY) License only, the subscription journals and a few of the Open Access Journals offer a choice of Creative Commons Licenses. The license type is clearly identified on the article.

### The Creative Commons Attribution License

The [Creative Commons Attribution License \(CC-BY\)](#) allows users to copy, distribute and transmit an article, adapt the article and make commercial use of the article. The CC-BY license permits commercial and non-

### Creative Commons Attribution Non-Commercial License

The [Creative Commons Attribution Non-Commercial \(CC-BY-NC\) License](#) permits use, distribution and reproduction in any medium, provided the original work is properly cited and is not used for commercial purposes.(see below)

### Creative Commons Attribution-Non-Commercial-NoDerivs License

The [Creative Commons Attribution Non-Commercial-NoDerivs License](#) (CC-BY-NC-ND) permits use, distribution and reproduction in any medium, provided the original work is properly cited, is not used for commercial purposes and no modifications or adaptations are made. (see below)

### Use by commercial "for-profit" organizations

Use of Wiley Open Access articles for commercial, promotional, or marketing purposes requires further explicit permission from Wiley and will be subject to a fee.

Further details can be found on Wiley Online Library  
<http://olabout.wiley.com/WileyCDA/Section/id-410895.html>

**Other Terms and Conditions:**

**v1.10 Last updated September 2015**

**Questions? [customercare@copyright.com](mailto:customercare@copyright.com) or +1-855-239-3415 (toll free in the US) or +1-978-646-2777.**





## Faults Diagnosis in Induction Motors Through Thermal Mapping Produced by the RDTS System

Author: Jessé de Pelegrin

Publication: IEEE Sensors Journal

Publisher: IEEE

Date: 15 Sept.15, 2021

Copyright © 2021, IEEE

### Thesis / Dissertation Reuse

The IEEE does not require individuals working on a thesis to obtain a formal reuse license, however, you may print out this statement to be used as a permission grant:

*Requirements to be followed when using any portion (e.g., figure, graph, table, or textual material) of an IEEE copyrighted paper in a thesis:*

- 1) In the case of textual material (e.g., using short quotes or referring to the work within these papers) users must give full credit to the original source (author, paper, publication) followed by the IEEE copyright line © 2011 IEEE.
- 2) In the case of illustrations or tabular material, we require that the copyright line © [Year of original publication] IEEE appear prominently with each reprinted figure and/or table.
- 3) If a substantial portion of the original paper is to be used, and if you are not the senior author, also obtain the senior author's approval.

*Requirements to be followed when using an entire IEEE copyrighted paper in a thesis:*

- 1) The following IEEE copyright/ credit notice should be placed prominently in the references: © [year of original publication] IEEE. Reprinted, with permission, from [author names, paper title, IEEE publication title, and month/year of publication]
- 2) Only the accepted version of an IEEE copyrighted paper can be used when posting the paper or your thesis online.
- 3) In placing the thesis on the author's university website, please display the following message in a prominent place on the website: In reference to IEEE copyrighted material which is used with permission in this thesis, the IEEE does not endorse any of [university/educational entity's name goes here]'s products or services. Internal or personal use of this material is permitted. If interested in reprinting/republishing IEEE copyrighted material for advertising or promotional purposes or for creating new collective works for resale or redistribution, please go to [http://www.ieee.org/publications\\_standards/publications/rights/rights\\_link.html](http://www.ieee.org/publications_standards/publications/rights/rights_link.html) to learn how to obtain a License from RightsLink.

If applicable, University Microfilms and/or ProQuest Library, or the Archives of Canada may supply single copies of the dissertation.

BACK

CLOSE WINDOW